

SPECTRAL ANALYSIS OF SELECTED CEPHEIDS
AND THE GALACTIC DISTRIBUTION OF
METALLICITY

SUNETRA GIRIDHAR

Thesis submitted to the
Ravishankar University
for the degree of
Doctor of Philosophy

INDIAN INSTITUTE OF ASTROPHYSICS
October 1982

*This thesis is dedicated
to the memory of*

M.K.Vainu Bappu

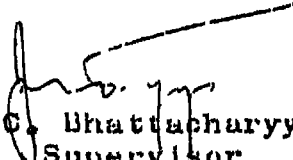
*who inspired me throughout this work,
but did not live to see its completion*

October 7, 1982

CERTIFICATE

This is to certify that Miss Sunetra Giridhar has completed her thesis for the award of the Ph.D degree of Kavishankar University, Raipur under my supervision.

I further certify that the thesis embodies the results of her own investigation and that she has worked under my supervision for the period stipulated by the Ph.D Ordinance of the University. In my opinion the thesis fulfills all the requirements of the aforesaid Ordinance.


(J.C. Bhattacharyya)
Supervisor

ACKNOWLEDGEMENTS

I wish to express my deep sense of gratitude to late Professor M.K. Vainu Bappu for suggesting the topic of this thesis and for constant encouragement and guidance throughout the project. The work would not have materialized if not for his generous allotment of observing time on 102-cm reflector at Kavalur and computing time in TDC 316 at the Indian Institute of Astrophysics. Various facilities at the Institute, in the aspects of observation, data reduction and the final presentation, which have all gone into this thesis, were all created by Professor Vainu Bappu.

I am thankful to Professor J.C. Bhattacharyya for becoming my Supervisor after the sudden demise of Professor Bappu on August 19, 1982. Professor Bhattacharyya has critically read all the Chapters of the thesis and made valuable suggestions that helped in the completion of the project.

I wish to thank Dr. N. Kameshwara Rao for giving me the spectrum synthesis code of C. Sneden and for many helpful discussions.

I am indebted to Dr. T.P. Prabhu for the keen interest taken by him in the project and for many valuable suggestions.

I am thankful to Mr. P. Venkatakrishnan and Mr. A.V. Ananth for a number of important suggestions during the

development and testing of the spectrum synthesis programme on TDC-316. Thanks are also due to the staff of the Computer Section, Mr. M.N. Muralidhar Rao, Mr. S.S. Chandramauli, Mr. A.V. Kutti and Miss E. Miranda, for their co-operation without which the computations could not have been completed.

The spectrograph used in the present investigation was designed by late Prof. M.K.V. Bappu and fabricated by Mr. Alfred Charles. The microdensitometer used in the reduction of photographic spectra was automated by Mr. C. Viswanath.

I thank Mr. A. Mohammed Batcha for his excellent typing of the entire thesis.

I also acknowledge the help of Miss Sandra D. Rajiva in the final presentation of the thesis.

Messrs. S. Muthukrishnan, P.U. Kamath and J. Hari Inbaraj prepared all the diagrams with great care. The copies were made by Mr. A.P. Monnappa and Mr. A. Elangovan. Mr. and Mrs. R. Krishnamurthy bound all the copies of the thesis. I am indebted to each of these individuals.

Bangalore-34
October 7, 1982

Sunetra Giridhar
(Sunetra Giridhar)

List of Publications

1. Violet absorption edges of C IV lines in Wolf-Rayet spectra possible superposition with diffuse interstellar bands at 5780\AA and 5797\AA - Sunetra Giridhar and M.K.V. Bappu - Kodaikanal Obs. Bull. Ser. A (1978) 2, 161.
2. The He II 5411\AA velocity curve of the Wolf-Rayet eclipsing system HD 214419 - Sunetra Giridhar - Kodaikanal Obs. Bull. Ser. A (1978) 2, 164.

CONTENTS

		<u>Page</u>
Summary	...	1
Chapter 1	... INTRODUCTION	1
	1.1 Importance of Abundance Determination in Astrophysics	1
	1.2 Chemical Evolution of Galaxies	3
	1.3 Models of Chemical Evolution	6
	1.4 The Radial Abundance Gradient	10
	1.5 Local Chemical Inhomogeneities	17
	1.6 Nucleosynthesis in Stellar Interiors	19
	1.7 Role of s-process Elements in the Chemical Evolution of Galaxies	22
	1.8 Cepheids as probes for the Chemical Constitution of the Galactic Disk	24
Chapter 2	... DETERMINATION OF CHEMICAL COMPOSITION OF STELLAR ATMOSPHERES	26
	2.1 Introduction	26
	2.2 The Curve of Growth	27
	2.3 The Differential Curve-of-Growth Method	36
	2.4 Fine Analysis	40
	2.5 Method of Spectrum Synthesis	41
	2.6 Computation of the Theoretical Spectrum	43

CONTENTS

		<u>Page</u>
Chapter 3	... OBSERVATIONS AND DATA REDUCTIONS ..	55
	3.1 Selection of Programme Stars ..	55
	3.2 Details of Observational Data ..	58
	3.3 Reductions of the Photographic Spectra ..	60
	3.4 Digitization and Reduction of the Raw Data ..	67
	3.5 The Instrumental Profile ..	73
Chapter 4	... METHOD OF ANALYSIS ..	77
	4.1 Description of the Computer Programme ..	77
	4.2 Justification of simplifying assumptions ..	97
	4.3 Determination of Atmospheric Parameters ..	102
	4.4 Assembling the line data ..	111
Chapter 5	... ABUNDANCE ANALYSIS OF INDIVIDUAL CEPHEIDS ..	118
	5.1 Introduction ...	118
	5.2 T Monocerotis - A Detailed Example..	120
	5.3 Other Stars Observed at Higher Resolution ..	132
	5.4 Stars observed at Lower Dispersion ..	138
	5.5 Error Analysis ..	146

CONTENTS

	<u>Page</u>
Chapter 6 ... RESULTS AND CONCLUSIONS ..	158
6.1 Compilation and Intercomparison of Spectroscopic Abundances ..	158
6.2 The Radial Abundance Gradient in Fe ..	167
6.3 Local Chemical Inhomogeneities in [Fe] ..	171
6.4 Variation of [s/Fe] across the disc ..	178
6.5 Summary of Conclusions ..	185
Chapter 7 ... DISCUSSION AND FUTURE PROSPECTS ..	187
Appendix	194
References	209

LIST OF TABLES

	<u>Page</u>
<u>Table 1.1:</u> Summary of different estimates of Fe abundance gradients in the Galaxy ..	15
<u>Table 1.2:</u> Summary of different estimates of O and N abundance gradients in the Galaxy ..	16
<u>Table 3.1:</u> Basic data on the Programme Stars ..	57
<u>Table 3.2:</u> Journal of Observations ..	61
<u>Table 5.1:</u> List of the iron lines computed over a grid of model atmosphere to determine atmospheric parameters ..	124
<u>Table 5.2:</u> Comparison of observed and computed Fe lines for δ 1161 of T Mon ..	128
<u>Table 5.3:</u> Derived model atmosphere parameters for the Cepheids ..	133
<u>Table 5.4:</u> Fe lines used in improving the parameters of T Mon based on low-dispersion spectra ..	142
<u>Table 5.5:</u> Cepheid abundances with respect to solar values	153
<u>Table 5.6:</u> Comparison of abundances derived in this study with those of Luck and Lambert (1981) ..	155
<u>Table 5.7:</u> The sensitivity of computed line strength to different atmospheric parameters ..	156

LIST OF TABLES

	<u>Page</u>
<u>Table 6.1:</u> Basic data for Cepheids with known spectroscopic abundances	.. 159
<u>Table 6.2:</u> Compilation of spectroscopic abundances of Cepheids	.. 160
<u>Table 6.3:</u> Abundances derived in the present investigation	.. 165
<u>Table 6.4:</u> Ages, birthsites and abundance residuals for Cepheids	.. 174
<u>Table 6.5:</u> Abundances of s-process elements in Cepheids	180
<u>Table A.1:</u> Line data : 4329-4335Å	.. 195
<u>Table A.2:</u> Line data : 4348-4365Å	.. 196
<u>Table A.3:</u> Line data : 4398-4402Å	.. 197
<u>Table A.4:</u> Line data : 4406-4428Å	.. 198
<u>Table A.5:</u> Line data : 4472-4476Å	.. 200
<u>Table A.6:</u> Line data : 4483-4489Å	.. 201
<u>Table A.7:</u> Line data : 4506-4518Å	.. 202
<u>Table A.8:</u> Line data : 4551-4573Å	.. 203
<u>Table A.9:</u> Line data : 4574-4584Å	.. 205
<u>Table A.10:</u> Line data : 4584-4632Å	.. 206

LIST OF FIGURES

	<u>Page</u> <u>No.</u>
<u>Figure 2.1:</u> (a) A typical curve of growth and (b) the change in the appearance of a line in different regions of the curve of growth (Gray 1976).	32
<u>Figure 2.2:</u> Continuum flux contribution functions at various wavelengths for a solar model (Gray 1976).	47
<u>Figure 2.3:</u> Continuum flux contribution functions longward (3660\AA) and shortward (3640\AA) of Balmer discontinuity for a solar model (Gray 1976).	48
<u>Figure 2.4:</u> Continuum flux contribution functions at $\lambda = 7000\text{\AA}$ for various temperatures, for a solar model (Gray 1976)	50
<u>Figure 3.1:</u> Distribution of the programme Cepheids in galactic plane with the spiral arms traced by young open clusters and H II regions (based on Becker and Penkart 1970).	56
<u>Figure 3.2:</u> (a) Density steps in the calibration plate and (b) the characteristic curve determined from them.	64
<u>Figure 3.3:</u> The relationship between the equivalent widths and the central depths of absorption lines of Fe.	72

LIST OF FIGURES

	<u>Page</u> <u>No.</u>
<u>Figure 4.1:</u> Block diagram of the synthesis programme.	78
<u>Figure 4.2:</u> Contribution functions for Fe I 4375.944 ($E1 = 0.0$ eV; broken line) and Fe I 4625.052 ($E1 = 3.2$ eV; solid line).	98
<u>Figure 4.3:</u> Comparison of the theoretically computed spectrum (dots) based on the solar model atmosphere of Holweger and Müller (1974), with the observed solar spectrum (continuous line) of Minnaert, Mulders and Houtgast (1940).	113
<u>Figure 5.1:</u> Atmospheric parameters of T Mon as a function of phase of the light curve, estimated by different investigators.	126
<u>Figure 5.2:</u> Observed (continuous line) and computed (broken line) spectra of T Mon; 4550-4590Å.	129
<u>Figure 5.3:</u> Observed (continuous line) and computed (broken line) spectra of T Mon; 4600-4635Å.	130
<u>Figure 5.4:</u> Observed (continuous line) and computed (broken line) spectra of ζ Gem; $\phi = 0.238$.	135

LIST OF FIGURES

	<u>Page No.</u>
<u>Figure 5.5:</u> Observed (continuous line) and computed (broken line) spectra of ζ Gem; $\phi = 0.427$.	136
<u>Figure 5.6:</u> Observed (continuous line) and computed (broken line) spectra of X Sgr; $\phi = 0.258$, 4328-4364Å.	139
<u>Figure 5.7:</u> Observed (continuous line) and computed (broken line) spectra of X Sgr; $\phi = 0.394$, 4410-4476Å.	140
<u>Figure 5.8:</u> Observed (continuous line) and computed (broken line) spectra of X Sgr; $\phi = 0.394$, 4552-4590Å.	141
<u>Figure 5.9:</u> Observed (continuous line) and computed (broken line) spectra of T Mon at lower resolution; 4328-4426Å.	144
<u>Figure 5.10:</u> Observed (continuous line) and computed (broken line) spectra of T Mon at lower resolution; 4550-4590Å.	145
<u>Figure 5.11:</u> Observed (continuous line) and computed (broken line) spectra of SV Mon; $\phi = 0.286$, 4554-4592Å.	147
<u>Figure 5.12:</u> Observed (continuous line) and computed (broken line) spectra of SV Mon; $\phi = 0.334$, 4328-4424Å.	148

LIST OF FIGURES

	<u>Page</u> <u>No.</u>
<u>Figure 5.13:</u> Observed (continuous line) and computed (broken line) spectra of SV Mon; $\phi = 0.334$, 4552-4586 \AA .	149
<u>Figure 5.14:</u> Observed (continuous line) and computed (broken line) spectra of WZ Sgr; $\phi = 0.219$, 4328-4364 \AA .	150
<u>Figure 5.15:</u> Observed (continuous line) and computed (broken line) spectra of WZ Sgr; $\phi = 0.219$, 4406-4516 \AA .	151
<u>Figure 5.16:</u> Observed (continuous line) and computed (broken line) spectra of WZ Sgr; $\phi = 0.941$, 4552-4592 \AA .	152
<u>Figure 6.1:</u> Observed abundance ratios $[\lambda/\text{Fe}]$ as a function of atomic number.	166
<u>Figure 6.2:</u> The galactic distribution of Cepheids. Spiral arms are traced from Humphreys (1978). Sun's position is shown by \odot symbol.	168
<u>Figure 6.3:</u> The radial abundance gradient in Fe. Sun's galactocentric position is shown by an arrow.	169
<u>Figure 6.4:</u> Birthsites of Cepheids with respect to the spiral arms sketched by Humphreys (1978). The numbers identify the stars through Table 6.4.	177

LIST OF FIGURES

	<u>Page</u> <u>No.</u>
<u>Figure 6.5:</u> A plot of $[S/Fe]$ as a function of galactocentric distance.	182
<u>Figure 6.6:</u> A plot of $[S/Fe]$ against $[Fe/H]$.	183

SUMMARY

The importance of determination of elemental abundances in stellar atmospheres lies in the clue it gives on the nuclear history of stellar matter and more generally of the matter in the whole Galaxy. The chemical composition of stars of different age groups leads us to an understanding of the chemical history of the Galaxy. Primal matter out of which the Galaxy was formed is believed to be consisting of only hydrogen and helium. The enrichment of the interstellar matter has resulted from the processed gas ejected by stars at their advanced stages of evolution. Large and small-scale chemical inhomogeneities in the Galaxy have an important bearing on the problem of galactic evolution. The observed radial gradient in the disk of our Galaxy, abundance anomalies across the spiral arms and also the ratios of the abundances of elements formed in primary and secondary nucleosynthesis provide the observational tests for the models of galactic evolution.

In the present investigation, we have derived the above mentioned quantities by the spectroscopic studies of classical Cepheids. This group of stars, due to its high intrinsic luminosity, smaller age and the existence of period-luminosity and period-age relationships, is a very good candidate for the studies of galactic evolution.

The importance of determination of elemental abundances in astrophysical objects is reviewed in Chapter 1 and the methods employed in the determination of the stellar chemical composition are described in Chapter 2. Chapter 3 describes the observational data for the present study and the reduction techniques employed. The spectra used in the present investigation were obtained using the 102-cm reflector of Kavalar Observatory between 1980-81. These spectra were analysed using the automated microphotometer of the Indian Institute of Astrophysics, using the microcomputer programmes specially written for the present work. The method of computation of the theoretical spectrum is described in Chapter 4. The computation, based on the formal solution of radiative transfer, incorporated the simplifying assumptions of local thermodynamic equilibrium, hydrostatic equilibrium and plane-parallel geometry. These assumptions are reasonably good for the metallic lines of F-G stars. The list of spectral lines computed, and their gf values derived from an inverted solar analysis, are given in the Appendix.

The resultant abundance determinations for the Cepheids τ Monocerotis, ξ Geminorum, χ Sagittarii, ω Sagittarii and δ V Monocerotis are presented in Chapter 5. The agreement between the observed and the computed spectra is shown in

the figures. These results are discussed in Chapter 6. We derive an abundance gradient of

$$\frac{d[\text{Fe}/\text{H}]}{dr} = -0.056 \pm 0.008.$$

The range in galactocentric distances of the present sample exceeds the past spectroscopic attempts, rendering the present work more reliable. The good agreement between the gradient derived here and the earlier photometric estimates shows that there are no systematic errors in the photometry of the past investigators.

The star ζ Gem shows marked overabundances of all the heavy elements for its position in the galactic disk. This overabundance of ζ Gem is also reported in the investigation of Luck and Lambert (1981). Similar overabundance has also been noted in W Sgr. To understand this abrupt departure from the smooth abundance variation across the disk, birthsites of all the Cepheids with known spectroscopic abundances were examined. For a majority of the stars with known spectroscopic abundances, Wislon (1973) has determined the birthsites by the detailed calculations of galactic orbits of these stars. For the remaining stars, birthsites were determined from galactic rotation assuming an age derived from the period-age relationship. It was seen that both ζ Gem and W Sgr were born far from the inner edge of the spiral arm where a majority of the stars are born. A

$$\frac{1.8 \text{ kpc}}{4.8 \text{ kpc}} = \frac{5.6 - 4.30}{4.30} = 13\% \text{ (excess)}$$

possible explanation for their overabundance is advocated in Chapter 6. In this picture, the massive stars born near the inner edge of the spiral arm move away from it as they evolve. At the end of their life, they explode as supernovae and enrich the local interstellar medium with processed matter. The stars ϵ Gem and η Sgr are probably formed from such matter. Abundances of the element derived in the present investigation do not show any significant correlation with atomic number. Also the abundance ratio of s-process elements (Ba, La, Ce, Sm) does not show any correlation with Fe. This implies that for the disk population there is no enrichment of s-process elements relative to Fe, such as has been observed earlier for halo population. The lack of any correlation between $[s/Fe]$ and $[Fe/H]$ for disk stars can be explained by the conventional infall models of Larson. We propose that an alternative explanation that the ratio $[s/Fe]$ can also be interpreted as the ratio of the intermediate-mass stars (which contribute s-process nuclei) to high-mass stars (which contribute to Fe peak nuclei). Thus the different behaviours of halo and disk populations may indicate a difference in the mass spectrum of star formation.

These results are discussed in Chapter 7, with an emphasis on the future prospects for an improvement of the techniques of analysis as well as for framing extensive observational programmes.

CHAPTER 1

INTRODUCTION

1.1 Importance of Abundance Determination in Astrophysics

The motivation for a study of abundances in astrophysical objects comes both from a desire to make sure that one understands the physical processes leading to the absorption and emission features and from the role played by abundance studies in understanding the origin of elements and the evolution of stars, galaxies and the universe.

An inspection of the abundances derived in various investigations can be used as a test of our understanding of line-forming processes through the principles of consistency and uniformity. The consistency principle is a truism; if an understanding of the line-formation process is complete, then the different lines of the same object should lead to identical abundances. The classical examples are the permitted and the forbidden lines of various elements, especially iron, in the solar photosphere. The uniformity principle is based on the presence of well-defined cosmic abundance distribution (see Suess and Urey 1956; Cameron 1968), which forms the basis of the theories of origin of the elements. Abundances of C, N, O, Na, Mg, Si, S etc. (well-represented in Fraunhofer spectrum)

relative to H are best determined from a study of the solar spectrum. Many rare-earth elements are best studied in meteorites. Abundances of He and Ne are determined from the corona and solar cosmic rays. According to the uniformity principle, the abundance estimates get better when they look alike in different objects. In spite of the exceptions like Ap stars, it has often proved a useful principle. Solar spectroscopists tend to measure the success of their abundance determinations by the agreement of their results with the Type 1 carbonaceous chondrites. The important work of Auer and Mihalas (1973) on non-LTE effects of Ne I in B stars was partly inspired by the uniformity principle.

Abundance studies are useful tools in the study of stellar evolution. Some years ago very few objects like Wolf-Rayet stars, helium stars, carbon, S and Ba II stars, Ap and Am stars were recognized to have anomalous or unusual abundances. Now almost all classes of stars away from main sequence are recognized as having modified the composition of their surface layers in respect of carbon and its isotopes, nitrogen and sometimes the s-process elements and the isotopes of oxygen. Anomalies in red giants are important because they provide evidence concerning hydrodynamical effects in stellar evolution. In metal-deficient giants in globular clusters, the effects are more drastic. Sweigart and Mengel (1979) explain it in terms of strong mixing effects in their

interiors and so in globular clusters we have a veritable jungle of abundance anomalies usually involving carbon depletion and nitrogen enhancement.

Studies of chemical composition of the interstellar medium (ISM) and the stars of different population groups are very useful in testing the models of the chemical evolution of the Galaxy. The big-bang cosmology predicts that at the time of galaxy formation the universe consisted only of H, He and possibly Li. Heavier elements were synthesized in stars by thermonuclear reactions and the enrichment of the ISM is due to the material ejected by the fast-evolving stars. Studies of the abundances in ISM and stars at different parts in the galactic disc would provide valuable clues to the evolution of the Galaxy.

In the present investigations, we would be interested in determining the chemical abundances of long-period Cepheids in order to study the large-scale inhomogeneities and trends in the abundance distribution in the Galaxy as a probe into its chemical evolution.

1.2 Chemical Evolution of Galaxies

The chemical inhomogeneity of the interstellar medium at a given time is an important factor to be explained by the models of galactic chemical evolution. The observations

which are relevant to the problem of the enrichment of the ISM in heavy elements are the following:

1) The stellar metallicities in the solar neighbourhood show an age dependence, in the sense that older stars are metal poor and younger stars are metal rich (Mayor 1976). This is inferred from the metal deficiency of the globular clusters and the ultra-high-velocity stars of the galactic halo population which are certainly old (Eggen, Lynden-Bell and Sandage 1962).

2) Long-lived stars of one solar mass or less in the solar neighbourhood have a narrow range of heavy metal abundance. Simple models of galactic evolution predict more metal-poor stars than observed. This discrepancy is called the G-dwarf problem (Schmidt 1963).

3) There is a large-scale radial abundance gradient in the Galaxy, as deduced from the metallicity and kinematics of nearby stars (Mayor 1976; James 1977) and from the oxygen abundances in H II regions (Peimbert 1979 and references therein).

4) Similar large-scale abundance gradients are found in other large galaxies, both elliptical and spiral. Faber (1977) reported gradients in a large number of normal E and SO galaxies using CN absorption features at 4160\AA , MgH + Mg I 'b' band at 5178\AA and Na I 'D' at 5893\AA . The observations

of H II regions in seven Sc galaxies by Searle (1971) also indicated the presence of an abundance gradient across the disc of these galaxies. Most large galaxies share the property of having greater metallicity (heavy-element abundance) in their central regions than in the outer parts. These gradients in the Galaxy as well as in external galaxies imply that inhomogeneities over a large length scale are created and survive during galactic evolution.

5) There is an abundance difference between the giant and dwarf elliptical galaxies in the sense that the metallicity in the central regions increases steadily with the mass or luminosity of the parent galaxy (e.g. Faber 1973, 1977). This effect and the large-scale gradient in elliptical galaxies probably results from the systematic flow of enriched gas from newly-formed stars towards the centre during the formative stages (Larson 1974).

The basic postulates of models for the chemical evolution of galaxies are that the galaxies are formed by the collapse of protogalactic clouds of gas accompanied by star formation. The protogalactic gas cloud is initially lacking in the heavy elements from carbon upwards, since the nucleosynthesis during the big-bang is expected to result only in hydrogen, deuterium, helium and possibly lithium in detectable quantities. The interstellar gas, then, is believed to be gradually

enriched in heavy elements by the matter coming out of the stars that have completed their own evolution and eject the products of nucleosynthesis in the course of their violent or slow deaths. In elliptical galaxies and the bulge of spirals, stellar relaxation times are longer than the age of the universe. This implies that the spheroidal shape of these components could not have resulted from the relaxation of stars. Hence, it has been proposed that these components assumed their shape at the time of their formation itself. This is possible through 'violent relaxation' proposed by Lynden-Bell (1967), which takes place if the star formation occurred on a timescale shorter than the collapse of the system as a whole. This implies that the star formation was largely completed a long time ago so that little gas is left. On the other hand, in the disk-like systems the star formation has evidently been delayed for some reason so that substantial amounts of gas are still there and we can see the star formation that is going on at the present time.

1.3 Models of Chemical Evolution

The important ingredient for the construction of models of galactic chemical evolution is the local stellar birthrate. The stellar birthrate is defined as the number of stars $b(m, t)$ in the mass interval $(m, m + dm)$ born per pc^2 in the time interval $(t, t + dt)$. To the first approximation, the

mass-dependence and the time-dependence of the stellar birthrate can be separated.

$$b(m, t) \, dm \, dt = \phi(m) \psi(t) \, dm \, dt$$

where $\psi(t)$ is the total star formation rate in mass per pc^2 per unit time and $\phi(m)$ is the initial mass function which is the distribution of stellar masses at birth.

The simple models of galactic chemical evolution are based on the following assumptions:

1) The evolution takes place in a cylindrical shell coaxial with the galaxy and passing through the Sun, in isolation with the rest of the galaxy. The models which make this assumption are known as the closed models.

2) The gas is initially unenriched and is gradually depleted by star formation.

3) The rate of star formation ψ varies as a power of the surface density μ of the gas (the surface density being the projected volume density of the gas on the galactic plane).

$$\psi = \psi_0 \mu^n.$$

4) The interstellar medium is well mixed at all times and in particular, new stars formed at time t have the average heavy element abundance of gas, $Z(t)$.

5) Initial mass function $\phi(m)$ has a constant form.

The two important parameters of the models of galactic evolution are firstly the fraction of mass in each generation that is returned to ISM which we shall call as β and secondly the yield of heavy elements which we will call p , defined as the total mass fraction of primary synthesis products ejected in each generation relative to the fraction that remains locked up in long-lived stars or collapsed remnants. In instantaneous recycling approximation where one assumes the evolutionary processes to take place instantaneously compared to the timescale of galactic evolution, these two quantities are constants characteristic of IMF adopted. From the above considerations, the heavy metal abundance Z , in the gas or in newly formed stars, at a given time is given by

$$Z = p \ln (1 + s/g)$$

where s is the mass locked up in stars or compact remnants and g is the mass of gas that is left. Searle and Sargent pointed out that this equation predicts a large scale radial abundance gradient in the galactic disc such as already established observationally by Searle (1971).

The simple model of galactic evolution runs into difficulties because of its incapability to explain the narrow range of metallicity of G dwarfs.

As we look across the galaxy at a particular moment of time, more of the gas has been changed into stars in the inner region than in the outer region. Some authors have considered the rates of star formation varying with a power law of the average gas density, with an exponent greater than one, which can arise from a variety of reasons like the free-fall timescale, the rate of collisions of clouds and so forth. Such law, when applied to the past history of the solar neighbourhood using the Simple Model, comes into conflict with an attempt to reconcile the relative number of large-mass and low-mass stars seen today with a constant and smooth IMF; there are too few long-lived dwarf stars, compared with the number of short-lived O and B stars, to permit the average past rate of star formation to have exceeded the present rate by as much as would be required by a power law in the gas density with an exponent of even one, let alone more than one. To solve this problem one can propose that the IMF could have varied or it could be discontinuous, with low-mass and high-mass stars being born in quite separate sets of events (Eggen 1976). More simply, the mass of the gas could have had a phase in the past when it was increasing owing to infall (Larson 1974; Lynden-Bell 1975; Larson 1976)

so that one can have a power law in the gas density for the rate of star formation, combined with a non-monotonic dependence on time. This form of departure from Simple Model provides a natural explanation for the narrow range of abundance in G dwarfs; further, it can also account for the indication that the past rate of star formation has been fairly uniform. Thus Larson's (1976) model with decaying Infall, and the closely related analytical model of Lynden-Bell are the most reasonable models for the evolution of disk-like galaxies.

1.4 The Radial Abundance Gradient

1.4.1 Abundance Gradient in Lighter Elements

Observations of H II Regions:

The presence of an abundance gradient of O/H, N/H and N/S in external galaxies has been reported by various observers from the observations of the ISM (Searle 1971; Peimbert 1968; Benvenuti, D'Odorico and Peimbert 1973; Shields 1974; Comte 1975). For our galaxy, Peimbert et al (1978) derived an abundance gradient for O/N, N/H, N⁺/S⁺ and He/H from the photoelectric observations of five H II regions covering a galactocentric range from 8.4 to 18.9 kpc. Hawley (1977) observed thirteen H II regions and found smaller gradients in O/H and N/H than those found by Peimbert et al and no gradients in the He/H, S/H and Ne/H abundance ratio.

Barker (1974), D'Odorico, Peimbert and Sabbadin (1976), Aller (1976) and Torres-Peimbert and Peimbert (1977) have studied the abundance gradient in the galaxy from the observations of Planetary Nebulae (PN). The abundance gradient can be studied only through type II PN which are of population I and which have apparently not been affected by considerable helium enrichment due to their own stellar evolution.

Periods of Cepheids:

It is known that in the Galaxy as well as in M31 and the Magellanic Clouds, short period Cepheids are concentrated towards the outer regions and long-period Cepheids towards the inner regions (Shapley and McKibben 1940; van den Berg 1958; Baade and Swope 1965; Fernie 1968). A possible explanation is that this effect is due to a radial gradient in the chemical composition of these galaxies.

It is possible to obtain a crude estimate of the O/H abundance gradient in the Galaxy by assuming that the O/H abundance is directly proportional to the Cepheid period (at a given mass of the Cepheid). Such a relationship has been identified through a comparison of the observations of the H II regions and Cepheids in the Small Magellanic Cloud (SMC) and the solar neighbourhood. The assumption that the Cepheid periods are related to the metal abundances is

supported by the results of Gascoigne (1969) and Madore (1974) who found that the SMC Cepheids are 0.1 mag bluer in B-V than the Cepheids in the galaxy. Bell and Parsons (1972) have explained this difference as due to reduced line-blanketing in SMC Cepheids or in other words, the reduction in metal content in SMC Cepheids by a factor of four relative to the galactic Cepheids. Fernie (1968) found for the galaxy a relation between the galactocentric distance R and the Cepheid period given by

$$\Delta \log P / \Delta R = -0.05 \text{ d kpc}^{-1}$$

and an average value of $\log P(d) = 0.97$ for the Cepheids of solar neighbourhood. Arp and Kraft (1961) found an average value of $\log P(d) = 0.5$ for the SMC Cepheids. Peimbert and Torres-Peimbert (1976) have found a difference of 0.76 in the $\log (O/H)$ between the solar vicinity and the SMC H II regions. One obtains from these results $\Delta \log (O/H) / \Delta \log P(d) = 1.6$ and thus a radial gradient in the galaxy of $d \log (O/H) / dR = -0.08 \text{ kpc}^{-1}$.

1.4.2 Abundance Gradient in Heavier Elements:

Grenon (1972), from the Geneva photometry of G and K dwarfs, found $d \log (Fe/H)/dR = -0.07 \text{ kpc}^{-1}$. Mayor (1976), from an analysis of the kinematic and photometric properties of about 600 F-type main-sequence stars and 600 G and K

giant stars, has derived two values of the metallicity gradient, one for all the objects with eccentricity of their galactic orbit in the range 0.05 - 0.40 and another for the subset of statistically younger objects with eccentricity 0.05 - 0.15. From the observations of Hansen and Kjaergaard (1971), Mayor has derived gradients in the sodium abundance corresponding to the two eccentricity groups described above. Sodium and iron gradients are steeper for the younger subset than for the complete sample. This result is in agreement with the absence of a gradient for halo stars derived by Grenon (1972), but is apparently in contradiction with the radial metallicity gradient derived from globular clusters in the solar neighbourhood which amounts to $d \log (Fe/H)/dR = -0.1$ (Kinman 1959; Mayor 1976). Janes and McClure (1972), from the DDO photometry of 799 K giant stars, presented the evidence for a radial gradient in CN strength. The CN strength is correlated with Fe/H. Janes (1977) covered a still larger sample of G and K giant stars and measured the CN strengths from DDO photometry; he also incorporated the UVB photometry of 41 open clusters to estimate the variation of metallicity across the galactic disk.

Williams (1966), from the narrowband photometry of 52 Cepheids with periods longer than 13 days, found that the Cepheids in the Sagittarius arm appear to be somewhat metal-rich as compared to those within 1.5 kpc of the Sun;

the Cepheids in the Cygnus arm, on the other hand, appear to be somewhat metal-deficient. Harris (1981), using the Washington system colours which are designed specifically to determine stellar abundances in the temperature range of Cepheids (Canterna 1976; Harris and Canterna 1979), determined photometric abundances for 102 Cepheids with a wide range of positions in the disk of the galaxy. He found a gradient in the metal abundance $d(A/H)/dr = -0.07 \text{ kpc}^{-1}$ for the galactic disk, approximately linear over 10 kpc.

Apart from the photometric attempts to determine the abundance gradient in the galactic disk, accurate spectroscopic abundance determinations have also been tried in the past. The analysis of Luck (1977a,b, 1978, 1979), Luck and Lambert (1981), and of Luck and Bond (1980), based on high dispersion spectra of F and G supergiants, suggests somewhat greater gradient than other studies. Though their relatively small range of 3 kpc in distance increases their uncertainty in the gradient, such an analysis should ultimately yield more accurate results as the sample is enlarged to larger distances. Besides, such detailed analyses are indispensable for the calibration of a photometric reddening-free abundance index. Various estimates of the abundance gradients in the galactic disk are summarized in Tables 1.1 and 1.2.

Table 1.1

Summary of different estimates of Fe abundance gradients
in the Galaxy

Objects	Method	-d Fe/H / dR	Source
Old disk stars	1	0.04 ± 0.03	1
gK and old open clusters	1	0.05 ± 0.01	2
Young disk stars (dF and dG)	1	0.10 ± 0.02	1
Young clusters *	1	0.098 ± 0.015 0.095 ± 0.034	3 4
Cepheids *	1	0.07 ± 0.01	5
Supergiants and Cepheids	2	0.13 ± 0.03	6
Cepheids	2	0.06 ± 0.01	7

* $-d \log (Z/X) / dR$

Method: 1. Photometry 2. Spectroscopy

Source: 1. Mayor (1976) 2. Janes (1979)
 3. Panagia and Tosi (1980) 4. Panagia and Tosi (1981)
 5. Harris (1981) 6. Luck (1982)
 7. Present study

Table 1.2

Summary of different estimates of O and N abundance gradients in the Galaxy

Objects	Method	$-d \log(O/H)/dR$	$-d \log(N/H)/dR$	Source
Cepheids	1	0.08		1
O stars (local gradient in Sagittarius arm)	2	0.13 ± 0.06		2
H II regions	3	0.06 ± 0.02	0.08 ± 0.02	3
		0.13 ± 0.04	0.23 ± 0.06	4
		0.05 ± 0.03	0.10 ± 0.03	5
		0.09 ± 0.02		6
H II regions (Sagittarius arm) (Persius arm)	3	0.24	0.16	3
		0.18	0.15	3
Planetary nebulae	3	0.06 ± 0.02	0.18 ± 0.04	7
		0.10 ± 0.03	0.27 ± 0.08	8
H II regions	4	$0.05 - 0.08$		9

Method :	1. Period calibration	2. Photometry	3. Spectroscopy
	4. Radio electron temperature		
Source :	1. Peimbert (1979)	2. Panagia and Tosi (1981)	
	3. Talent and Dufour (1979)	4. Peimbert, Torres-Peimbert and Rayo (1978)	
	5. Hawley (1978)	6. Peimbert and Torres-Peimbert (1979)	
	7. Torres-Peimbert and Peimbert (1977)	8. Peimbert and Serrano (1980)	
	9. Mezger et al (1980)		

The O/H abundance gradient obtained from H II regions is steeper than that given by PN. This difference, if real, could be due to at least three causes; (a) a different O/H distribution in the interstellar medium at the time of formation of the parent stars of PN; (b) a different O/H in the shell from that of the original cloud from which the parent stars of PN are formed; (c) the effect of non-circularity of the PN orbits around the centre of the galaxy.

The Fe/H and Na/H gradients derived from the intermediate age stars are similar to the O/H gradients derived from PN which supports the possibility (a). On the other hand, there is some observational evidence that suggests that the rate of enrichment of Fe has been different from that of O, S and A and consequently that the Fe/H and O/H are not directly comparable (Peimbert 1973; Barker 1974; Chevalier 1976a; Chevalier and Kirshner 1978). Furthermore, based on the observational evidence, Chevalier has suggested that the Fe enrichment is due to SN of type I while that of O, S and Ar is due to SN of type II.

1.5 Local Chemical Inhomogeneities

One of the important mechanisms that can produce local inhomogeneities is the sequential star formation in associations, the first generation of supernovae enriching the material out of which further stars immediately form.

There is considerable evidence that supernova explosions may induce further star formation. Sancisi (1974) and Knapp and Kerr (1974) found shells of cold H I, dust and molecules around supernova remnants; Berkhuijsen (1974) and Herbst and Assoua (1978) found young stellar associations on the edge of supernova remnants. It has been suggested that the formation of our own solar system was induced by a supernova. Even if the star formation is not actually triggered by supernova explosion, the synthesized material from a supernova could still be incorporated, provided the formation happens soon afterwards (e.g. instigated by photoionized H II region formations; Elmegreen and Lada 1977) before the inhomogeneity is destroyed by mixing. If the products of several supernovae are mixed into the mass of a typical observed shell ($3 \times 10^3 M_{\odot}$), then the excess over the surrounding metallicity, $dZ = 3 \times 10^{-3}$ would be possible, resulting in $\sigma \sim 0.1$ for the present mean disk abundances. Ögelman and Maran (1976) suggest a repetitive cycle of star formation—supernova may operate within OB associations, but the extent of homogeneity will depend on how well and quickly the supernova mixes into the interstellar medium before new star formation takes place. The expanding remnants will probably break up into knots (Chevalier 1975, 1976b; Gull 1974) which may be metal rich. It is not clear whether induced star formation occurs in these knots before they mix into outer material, or by the

supernova shocking of previously existing cool clouds of normal abundance.

1.6. Nucleosynthesis in Stellar Interiors

The theory of the synthesis of elements in stellar interiors is developed by Cameron (1955) and by Burbidge, Burbidge, Fowler and Hoyle (1957, B²FH). Starting with the hypothesis that all elements have been built from primordial hydrogen and helium, B²FH postulated as much as eight different nuclear processes to account for the observed features of the cosmic abundance distribution:

- 1) hydrogen burning to produce helium;
- 2) helium burning to produce C, O, Ne and perhaps Mg;
- 3) α -processes in which Mg^{24} , Si^{28} , S^{32} , Ar^{36} and Ca^{40} are produced by successive addition of helium nuclei to O^{16} and Ne^{20} , the α -particles being freed by decomposition of heavy nuclei;
- 4) the equilibrium s-process which was suggested to account for the iron peak elements;
- 5) r-process in which neutrons are captured at long timescales ranging from 10 yr to 10^5 yr for each neutron capture. This mode of synthesis is responsible for the production of the majority of isotopes in the range $23 \leq A \leq 46$ and for a considerable

portion of isotopes in the range $63 \leq A \leq 209$;

- 6) r-process in which neutrons are captured on a fast timescale $\sim 0.01s$ to $10s$;
- 7) the p-process in which proton-rich isotopes are formed;
- 8) x-process which is invoked for the production of the temperature-vulnerable light elements.

These nuclear processes operate in different stages of star's evolution. It is known that when the stars first form out of a gas of hydrogen and helium, the hydrogen burns in the core to produce helium and the star is then called a main-sequence star. When the hydrogen burning in the core is exhausted it begins to contract gravitationally until the temperature and density are large enough for helium to burn in the core. During this core-contraction stage, the outer envelope expands and the star becomes a red giant. When helium burns in the core, it creates carbon and oxygen via the triple-alpha reaction. At higher internal temperatures, a succession of x-processes may set in to form O^{16} , Ne^{20} and Mg^{24} . After depletion in the core, helium may continue to burn in a shell surrounding the depleted core. This shell is surrounded by a hydrogen-burning shell. At temperatures of $\sim 10^9 K$, reactions may take place among the C^{12} , O^{16} and Ne^{20} nuclei. Helium particles can be made

available through a (γ, α) reaction. Mg^{24} can capture alpha particles to form Si^{28} , S^{32} , A^{36} and Ca^{40} . The chain eventually terminates in the iron group of nuclei that have larger stability. During this time an equilibrium concentration is being reached between these even-even nuclei. This process is called the equilibrium process. If the star is a second generation star, i.e. it contains heavier elements, neutrons are produced via exergonic reaction $\text{Ne}^{21} + \text{He}^4 = \text{Mg}^{24} + n$ or $\text{C}^{13} + \text{He}^4 = \text{O}^{16} + n$. Heavier elements are formed via the process of slow and fast neutron captures.

It is useful to classify the elements according to the number of stellar generations required for their nucleosynthesis. Primary elements are those that can be formed directly from H and He inside the star (C^{12} , O^{16} , Ne^{20} , Fe^{56} etc.). Secondary elements are necessarily formed from the primary seeds which must have existed in the interstellar matter when the star was formed. Examples of such secondary elements are C^{13} , N^{14} and the s-process elements.

Enrichment of the ISM is mostly due to the material ejected by stars in their last stage of evolution. Most massive stars eject so-called primary nucleosynthesis products which can be built up directly from hydrogen and helium in the course of stellar evolution. The elements C, O, Ne and most of the nuclear species upto the iron group are formed

this way. Stars of intermediate mass (between one and few solar masses) eject their excess of material above the white-dwarf residue as gas that may have undergone some processing but without enriching it in oxygen or metals. Stars of about 1 solar mass or less simply form and remain there without significant contribution to the ISM as do the white dwarfs and other compact remnants such as neutron stars left behind by more massive stars after their death.

1.7 Role of s-process Elements in the Chemical Evolution of Galaxies

The s-process nuclei are an interesting probe of galactic evolution because they are produced via a secondary process. It is not possible to produce s-process nuclei in a star unless that star already contains some heavy seed nuclei. The bulk of the heavy element fraction Z is due to primary processes. The heavy primary nuclei which are the products of explosive nucleosynthesis are probably produced by explosions of massive stars $M \gtrsim 7 M_{\odot}$. The source of s-process nuclei is normally taken to be in the interiors of red giant stars (B^2FH). However, the details of how the s-process actually might work in such an astronomical site is only beginning to be understood. Ulrich (1973) investigated what happens during the double-shell-source phase of the evolution of certain stars. He finds that a reasonable

s-process environment occurs between the two shells whenever a flash mixes down hydrogen-burning material into helium-burning region. Ulrich (1974) has estimated that the s-process synthesis in such intershell sources can explain the abundance anomalies observed in FG Sagittae. In Ulrich's model, when the hydrogen is mixed down in the flash, it is captured by C^{12} ; the N^{13} thus formed rapidly decays into C^{13} ; at the high temperature inner boundary of the convective cell, the reaction $C^{13} (\alpha, n) O^{16}$ produces neutrons. These neutrons are captured by the iron-peak nuclei that serve as seeds for the s-process. The s-process nuclei built up in the intershell region gradually leak out into the outer envelope where they can be radiated away into the interstellar medium via the red giant's stellar wind. It may also be possible that the intershell region itself gets ejected during the later stages of stellar evolution.

As we have already seen, the iron peak and s-process elements are formed due to two fundamentally different nucleosynthesis processes, former resulting from explosive nucleosynthesis within supernovae and the latter due to slow neutron capture by heavy elements during advanced non-catastrophic evolution. These processes occur in different mass ranges of the star and depend in different ways on the star's initial composition. The abundance ratio of the s-process and iron peak elements may, therefore,

set important constraints on the theories of stellar and galactic evolution.

1.8 Cepheids as probes for the Chemical Constitution of the Galactic Disk

As a group, the classical Cepheids (referred to hereafter as Cepheids for the sake of brevity) have five properties which makes them perhaps the most suitable class of stars for studying the abundance variations in the galaxy:

1) Cepheids are intrinsically luminous objects. Their high intrinsic luminosity enables one to observe them at considerable range of distances.

2) They comprise of a homogeneous population, their masses, ages and luminosities are closely related to their periods, and the total range in age is much less than the age of the galactic disk.

3) Period-luminosity-colour relationship of Sandage and Tammann (1969) helps one to determine their distances with a sufficient degree of accuracy. The intrinsic luminosity of nonvariable supergiants is inferred on the basis of the luminosity class and the spectral type. The accuracy of these estimates is rather low and is only slightly improved by an application of model atmospheres.

4) Cepheids have a temperature range in which the spectra show enough number of metallic lines. Yet their temperatures are not too hot as to make the non-LTE effects very serious, while not too low for the convection to become important.

5) All the Cepheids with periods larger than 10 days are quite young and hence their atmospheric abundances reflect those of the interstellar medium out of which they are born.

Because of these advantages, we choose to study the chemical abundances of selected Cepheids in the present investigation.

CHAPTER 2

DETERMINATION OF CHEMICAL COMPOSITION OF STELLAR ATMOSPHERES

2.1. Introduction

The first star to be studied spectroscopically was obviously the nearest one - the sun. Early attempts to determine the solar chemical composition were based on eye estimates of line intensities. Russell, Adams and Moore (1928) pointed out that Rowland's eye estimates of the intensities of Fraunhofer lines could provide a wealth of information when they are calibrated for the number of absorbers. Before the development of a theoretical relation between the energy absorbed by a line and the number of atoms acting to produce it, they demonstrated the importance of an empirical calibration of the arbitrary scale of Rowland intensities. Their calibration was aimed to determine directly the relative number of atoms effective in producing lines of various intensities. The calibration was effected with the aid of multiplets in atomic spectra, the relative strength of whose lines could be predicted theoretically. A striking result of the work of Russell, Adams and Moore was the demonstration of the enormous differences in the number of atoms acting to produce lines of various Rowland intensities. They showed that millions of times as many atoms

were active in producing the violet FeI line at 3720\AA (Rowland intensity of 40) as for a line just visible on the spectrogram of the sun (Rowland intensity - 3). The important applications of Rowland's calibration to stellar spectra (α Ori, α Sco, α Boo, γ Cyg) were made almost immediately by Adams and Russell (1928) and to the solar spectrum by Russell (1929). With the hypothesis of thermodynamic equilibrium - which enabled them to use the ionisation and dissociation equation - and a further assumption that atoms at different levels are equally effective in producing a line, they derived a relation that connected the relative number of atoms acting to produce a given line in different stars with the relative total number of atoms of a given element, the excitation potential, the electron pressures, the ionization potentials and the temperatures. The vast difference in the amounts of metallic vapours above the photospheres of different types of stars was thus demonstrated.

2.2. The Curve of Growth

Although eye estimates of line intensities and the straightforward theories of ionization and excitation went a long way towards the interpretation of stellar spectra, further progress was required on the theory of line formation and quantitative measures of line intensity. Unsöld (1955)

approached the problem through the measurement and interpretation of line profiles, whereas Voigt, Minnaert and Slob studied the equivalent width of lines by means of a relationship now known as the curve of growth. The curve of growth is a relationship between the equivalent width of a line and number of atoms acting to produce it, or more precisely the quantity Nf where N is the number of absorbers and f is the oscillator strength. Equivalent width is a measure of the intensity of the line. It is generally expressed as the total amount of energy subtracted from the adjacent continuum. We express the intensity at any point in the line in terms of the continuous spectrum, i.e.

$r_\nu = F_{\text{line}}/F_{\text{continuum}}$, then the effective width of the line in frequency units is

$$W_\nu = \int_0^\infty (1 - r_\nu) d\nu. \quad \dots (2.1)$$

Since $\lambda = c/\nu$ and $d\lambda = \frac{c}{\nu^2} d\nu$, the equivalent width in Ångstrom unit is

$$W_\lambda = \frac{c}{\nu^2} W_\nu.$$

Early calculations of curve of growth (Voigt 1912; Minnaert and Mulders 1931; Minnaert and Slob 1931) were made with very simple models. Often the whole line-forming

region was characterised by a single temperature and gas pressure. Curve of growth calculations of Menzel (1936) and Unsöld (1955) were based on Schuster-Schwarzschild (S-S) model wherein the entire continuous absorption is assumed to originate in a photosphere overlaid by a reversing layer which produces all the absorption lines without any continuous absorption. The atmosphere, with its temperature and pressure gradients, may be replaced by an isothermal stratum of uniform density. The temperature and pressure correspond very closely to their values at an optical depth $\tau = 0.5$ in the atmosphere. In Schuster-Schwarzschild model, an approximation formula for r_{ν} as given below can be used.

$$r_{\nu} = \frac{F_l}{F_c} \frac{1}{1 + \tau_{\nu}}$$

Where F_l is the flux in the line, F_c is the flux in nearby continuum and $\tau_{\nu} = N \alpha_{\nu}$ is the optical depth in the line, α_{ν} being the atomic coefficient of line absorption at the frequency ν and N the number of atoms causing the line absorption. Line absorption coefficient plays a fundamental role in determining the shape of a spectral line. Several different physical effects enter the structuring of the final absorption coefficient. Each of these effects has associated with it a function describing the variation in strength of the line absorption with wavelength across the line, i.e. each one of these processes has its own absorption coefficient. Some of the processes are (1) natural

broadening, (2) pressure broadening and (3) thermal broadening. The natural broadening and all the significant broadening processes have the same wavelength dependence in their individual absorption coefficient. The basic form of these absorption coefficients is that of the dispersion profile. The thermal broadening reflects the Maxwellian velocity distribution of the absorbing atoms and ions via the Doppler effect. While combining these absorption coefficients, all these distributions must be convolved together to obtain the combined result. Convolution of the dispersion profiles results in a new dispersion profile with $\beta = \sum_j \beta_j$; where β_j are the half widths of individual profiles. The convolution of the dispersion and Gaussian profiles is the Voigt function. The normalized Voigt function can be expressed as

$$U(a, v) = \frac{a}{\pi^{3/2}} \int_0^{\infty} \frac{e^{-y^2}}{(v-y)^2 + a^2} dy,$$

where a and v are the damping parameter and Doppler velocity, respectively. We will consider these quantities in greater detail in the next chapter, where the calculation of absorption coefficient is described.

Menzel has suggested writing the equation for α_ν in the form

$$\alpha_\nu = \frac{\pi e^2}{mc} f \left[\frac{c}{c_0 \nu \sqrt{\pi}} \exp \left\{ -\frac{c}{c_0} \left(\frac{\nu - \nu_0}{\nu_0} \right) \right\}^2 + \frac{\Gamma}{4\pi^2} \frac{1}{(\nu - \nu_0)^2} \right] \quad \dots (2.2)$$

where Γ is the damping constant. With the understanding that the first term will be employed in the Doppler core of the line and the second in the absorption wings; here, c_0 is the most probable velocity.

The meaning of the curve of growth can now be illustrated. Suppose that in the atmosphere of a star we introduce an increasingly greater concentration of an element say, iron. When the number of atoms is small $N\alpha_0 \ll 1$, the line appears as only a tiny dip in the continuum, curve A of the Figure (2.1b). As the number increases, the line broadens slightly and becomes deeper. In the S-S model of a pure scattering atmosphere, the central intensity approaches zero as N is increased. For the lines formed by pure absorption, the minimum residual flux is fixed by the temperature distribution. Then, for an appreciable range of $N\alpha_0$, where α_0 is the atomic absorption coefficient at the line centre ($\nu = \nu_0$), the equivalent width changes slowly with increasing N . As N continues to increase, however, absorption in the damping domain becomes important

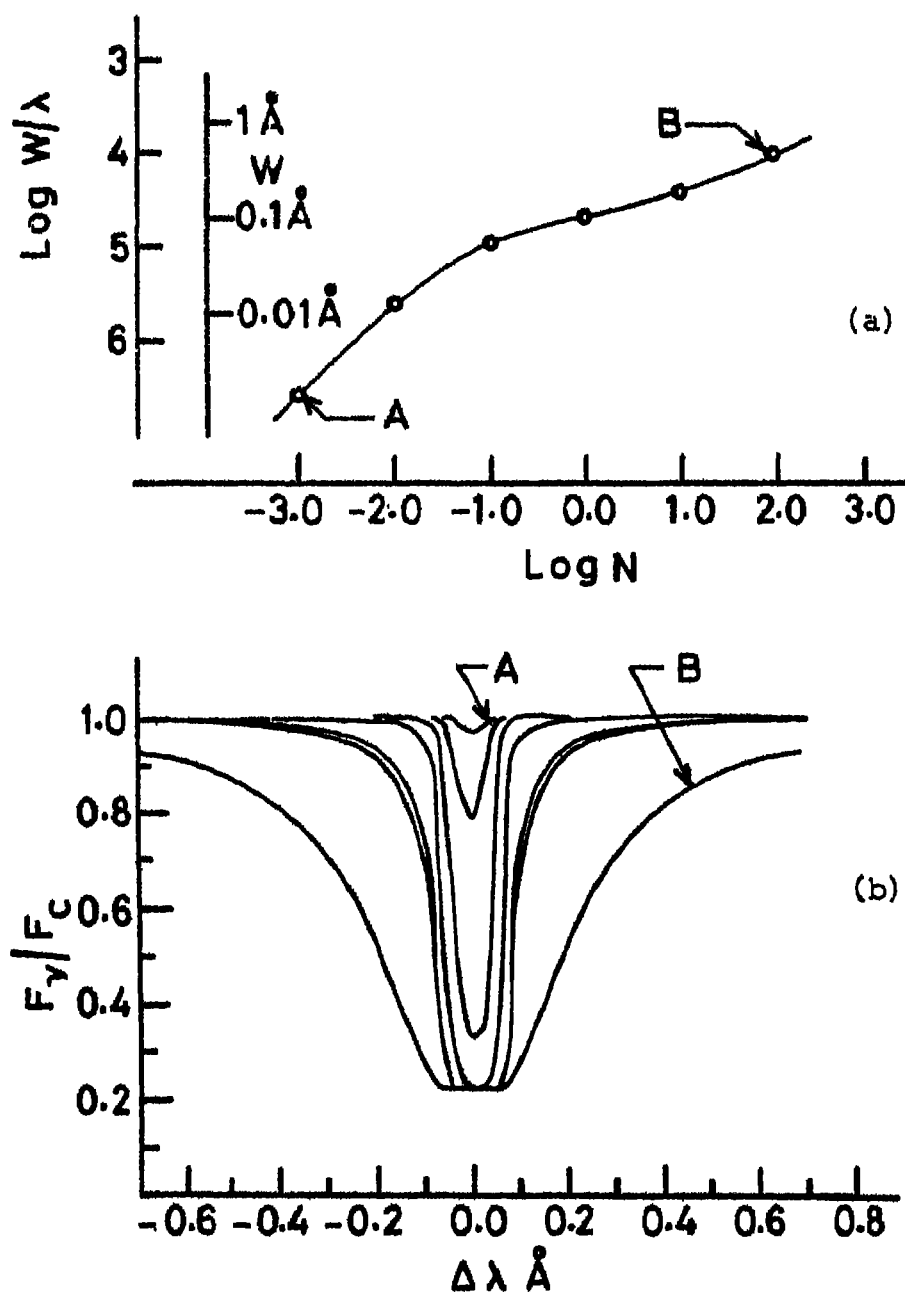


Figure 2.1 (a) A typical curve of growth and (b) the change in the appearance of a line in different regions of the curve of growth (Gray 1976).

and the line develops the characteristic wings. Figure (2.1a) shows the characteristic relation between the equivalent width of a line, W , and the number of atoms acting to produce it:

$$W_{\nu} = \int_0^{\infty} (1 - r_{\nu}) d\nu = \int_0^{\infty} \frac{N\alpha_{\nu}}{1 + N\alpha_{\nu}} d\nu. \quad \dots (2.3)$$

The change in the appearance of the line is shown in Figure (2.1b).

Menzel introduced a fictitious optical depth at the centre of the line

$$x_0 = N\alpha_0 = N \frac{\pi e^2}{mc} f \frac{1}{\sqrt{\pi}} \frac{c}{c_0 \nu_0} \quad \dots (2.4)$$

and considered the three domains of x_0 :

1) Equations (2.2) - (2.4) yield

$$\frac{W_{\lambda}}{\lambda} = \sqrt{\pi} \frac{c_0}{c} x_0 \left(1 - \frac{x_0}{\sqrt{2}} + \frac{x_0^2}{\sqrt{3}} \right) \quad \text{for } x_0 < 1$$

and

$$\frac{W_{\lambda}}{\lambda} = \sqrt{\pi} \frac{c_0}{c} x_0 \quad \text{for } x_0 \ll 1$$

2) For the intermediate values of x_0 , when $x_0 \gg 1$ but not so great that the effect of damping becomes

important, W_λ / λ grows more slowly with x_0 in accordance with the expression given by Menzel:

$$\frac{W_\lambda}{\lambda} = 2 \frac{c_0}{c} (\ln x_0)^{\frac{1}{2}} \left[1 - \frac{\pi^2}{24} \frac{1}{(\ln x_0)^2} + \dots \right].$$

3) Finally when x_0 is very large the second term in the equation of atomic absorption coefficient becomes important and

$$\frac{W_\lambda}{\lambda} = \frac{\sqrt{\pi}}{2} \left(\frac{c_0}{c} \right)^{\frac{1}{2}} \left(x_0 \frac{\Gamma}{\nu_0} \right)^{\frac{1}{2}}$$

Using the above functional behaviours in the three domains, one may compute a family of curves for different values of Γ/ν_0 . When the number of absorbing atoms is small, the equivalent width is proportional to Nf . This region is known as the straight-line or Doppler portion of the curve of growth. As the number of active atoms increases, the line saturates and W grows more slowly than Nf until a flat region is reached where the increase is slow. Indeed, this portion is known as the flat portion of the curve of growth. Here, the number of absorbers is sufficient for the Doppler core of the line to be complete, but absorption at wings has not yet set in. When the number of acting atoms Nf has become very large, the damping or square-root portion of

curve of growth begins, where the equivalent width is proportional to $\sqrt{Nf\tau}$.

Menzel's and Unsöld's formulations both regard the spectral lines as formed in a layer of absorbing atoms overlying a sharply defined photosphere. But most spectral lines, however, originate principally in the same layer as does the continuous spectrum and for these the Milne-Eddington (M-E) approximation of a constant ratio of line-to-continuous absorption coefficient is more satisfactory. Instead of χ_0 , which involves the number of atoms above the photosphere, in M-E model, one utilizes the ratio of the line absorption coefficient per gram of the stellar material at the centre of the line (l_0) to the coefficient of continuous absorption (κ). Curves of growth based on this hypothesis have been computed by Strömgren (1940), Goldberg and Pierce (1948), Wrubel (1949) and others. Wrubel computed the curve of growth based on Chandrasekhar's exact solution of the transfer equation for lines formed according to the ME model. His curves of growth have been used in many abundance determinations.

There are appreciable differences between the curves of growth computed on the M-E and S-S models in the damping portions; the damping constants derived from the S-S model are smaller by a factor of two.

The widespread use of electronic computers since nineteen sixties made it possible to replace these single-layer models with depth-dependent models. Once such detailed model is calculated for a particular star (say, Sun), it may be scaled in optical depth to suit another star. This technique is described by Cayrel and Jugaku (1963) and applied by Gray (1967).

Because of the prolonged use of very simple models to calculate the curve of growth, some astronomers imply a single layer model whenever they refer to the curve of growth. In reality, the curve of growth is a concept which applies under extremely general conditions. Depending upon the physical condition and the particular transition giving rise to an absorption line, the appropriate curve of growth will have its own shape, and one of the basic problems is the determination of this shape. It is only when equivalent widths themselves are not clearly defined, as in the case of severe blending, that the curve of growth is not useful.

2.3. The Differential Curve-of-Growth Method

For an application of absolute curve of growth, one must know the mechanism of line formation, atmospheric structure and a set of f -values (the atomic oscillator strengths), and more or less proceed with the first principles. The difficulty with this fundamental approach is that the

f values of all the transitions are necessary, a requirement very much difficult to fulfill in reality. Further, the calculations of the other parameters like the absorption coefficients and damping constants, need to be carried out for all the lines considered. A simpler differential method has become fairly popular which circumvents these difficulties. In this method, one compares the spectrum of a programme star with a standard star for which the chemical composition \bar{T} , \bar{P}_0 and \bar{P}_g are presumably known. The selected standard star must be similar to the programme star in spectral type and luminosity class or in other words the atmospheric parameters of the two stars should not differ considerably. To illustrate the method, let us consider a star whose temperature does not differ greatly from that of the Sun. If M-E model is employed, one uses as abscissa

$$\log \eta_0 = \log N_{r,s} + \log \alpha_0 - \log K_\nu \quad \dots (2.5)$$

where $N_{r,s}$ is the number of atoms per gram of the stellar material capable of absorbing the line in question. $N_{r,s}$ can be expressed in terms of Boltzmann's equation

$$\log N_{r,s} = \log N_r + \log g_{r,s} - \log u(T) - \theta \chi_r, \quad \dots (2.6)$$

$$\alpha_0 = \frac{\pi e^2}{mc} f \frac{1}{\Delta \nu_0} \quad \text{and} \quad v^2 = \left(\frac{2kT}{M} + \xi^2 \right)^{\frac{1}{2}}$$

Using the superscripts * and @ to denote the quantities for the star and the Sun respectively, we obtain for each

spectral line

$$\log \frac{\eta_0^*}{\eta_0^\circ} = \log \frac{N_r^*}{N_r^\circ} - \chi_{r,s} (\theta^* - \theta^\circ) - \log \frac{V^* u^*(\tau)}{V^\circ u^\circ(\tau)} - \log \frac{\kappa_\lambda^*(P_e^*, \tau)}{\kappa_\lambda^\circ(P_e^\circ, \tau)} \quad \dots (2.7)$$

where $\theta = 5040/T$. Notice that not only the numerical constants, but also the gf values cancel out. Now η_0^* and η_0° may be read for each line in the Sun and the star from the curve of growth with $\text{Log } \frac{W_c}{\lambda V}$ as ordinate, the curve being assumed to be the same for the Sun and the star. To simplify the notation let us write any quantity ζ as

$$\log \frac{\zeta^*}{\zeta^\circ} = [\zeta].$$

Equation (2.7) now reduces to

$$[\eta] = [N_r] - \chi_{r,s} (\theta^* - \theta^\circ) - [Vu(\tau)] - [\kappa_\lambda]. \quad \dots (2.8)$$

For each element, we group the line according to the excitation potential and for each of these groups we determine the shift necessary to fit the empirical curve to the theoretical curve both for the Sun and the star. The difference in log provides for each of these groups the value of $[\eta]$. If T^* and T° does not differ greatly, then $[\kappa_\lambda]$ will be virtually independent of λ and will depend

mostly on the ratio P_e^*/P_e^\odot . If one plots $\log(N_r - \theta\chi)$ against χ , the slope of the line gives θ^* . Knowing the temperature of the Sun and the star, we can evaluate the term $\nu(T)$. P_e^*/P_e^\odot can then be determined from Saha's and Boltzmann's equations. Knowing all these quantities, we can interpret $[\eta]$ in terms of $[N_r]$ and in turn, $[N_r]$ in terms of the actual abundance ratio.

In the past, it was practice to assume that most of the MK standard stars have the same chemical composition. This provided a grid-work of stars with varying temperature and pressure which could be used to determine differential abundances over a wide range of physical conditions. But, there are growing indications that the abundances of all the elements are not constant for stars of different spectral types. Thus, the abundance of the standard stars need to be determined from the first principles. Further, the differential method can be used only to estimate small differences in abundances. Many stars like a high-velocity stars or Ap and Am stars that have chemical composition so much different from the standard MK types, cannot be compared with these standard stars. Besides, the need for accurate f values is not really eliminated. The standard curve of growth for the reference star is to be constructed using the known f values. Though f values cancel out in differential analysis, the relative f values must be known for some set of lines

observed in the reference star and they must range sufficiently in strength to define the curve of growth for the reference star.

2.4. Fine Analysis

In the single-layer curve-of-growth procedure, it is supposed that all essential properties of the spectrum can be represented by a single value of temperature and pressure. But, it is scarcely to be expected that the lines of low and high excitation are formed in the same atmospheric layers. In the refined treatments of stellar atmospheres, the variation of temperature, pressure etc. with depth are taken into consideration. For the Sun, $T(\tau_\lambda)$ (where λ is some specific wavelength, say, $\lambda = 5000\text{\AA}$) has been obtained using the energy distribution at the centre of the Sun's disc and the limb darkening data. Once the temperature distribution is adopted, P_g and P_e can be calculated as a function of optical depth from the condition of hydrostatic equilibrium. Various workers have constructed model solar atmospheres based on empirical and/or theoretical considerations (Holweger and Müller 1974 ; Gingerich et al 1971; Vernazza, Avrett and Loeser 1976). For other stars, theoretical models have generally been used. These theoretical models are calculated using following assumptions: (1) Plane parallel geometry, (2) Hydrostatic equilibrium, and (3) the sum of the radiative and convective fluxes is depth and time-

independent. For F-G supergiants Parsons (1969) has computed model atmospheres, Models of O B A F G stars by Kurucz (1979) and of cooler stars by Gustafsson et al (1975) covering a large range in gravities, are currently in use.

The determination of composition of a stellar atmosphere using detailed models proceeds by successive approximations. First, a curve-of-growth analysis supplies an approximate composition and temperature. Next, a grid of model atmospheres is calculated and using them the theoretical line intensities of selected model-sensitive lines are computed. For example, for a star whose temperature is about 22,000K one might employ lines of Si II, Si III and Si IV which appear simultaneously in the spectrum. Also, the model should predict correctly the hydrogen line profiles, the discontinuity at the Balmer limit, and the energy distribution in the continuous spectrum. Once a suitable model has been identified or interpolated, a calculation of the theoretical equivalent widths is carried out and abundances are derived from a comparison of the observed and predicted equivalent widths.

2.5 Method of Spectrum Synthesis

The most complete studies are done on high-quality data by computing simultaneously all the lines over a

portion of the spectrum. To apply this method of spectrum synthesis, most (if not all) of the observed lines should be identified and must have known gf values. Then, using a suitable model atmosphere and atomic parameters of all lines falling in the region of interest, the spectrum is computed. The individual abundances (or perhaps the temperature and pressure) are adjusted until a good fit is obtained. Even when the lines are blended together, one simply computes the blend and the comparison is made with the data. The method of spectrum synthesis is more reliable, in principle, because it takes into account all the known absorption features and tries to reproduce the observed spectrum as precisely as possible without attempting to compare the observed equivalent widths of individual lines with the computed ones. The latter process requires a precise location of the continuum and the extrapolation of the profile of each line, because in reality none of the spectral lines shows the complete profile, the wings being generally blended with the neighbouring lines. In the curve-of-growth method the lines falling on the linear portion of the curve of growth are used. In order to measure the equivalent width of these weak lines, one requires a very high resolution, since the blending due to neighbouring lines is often disastrous at lower dispersions even in the relatively clean spectral regions. Moreover, the possibility of defining the continuum decreases drastically with

decreasing resolution. Further, the crowding of the spectral lines is so severe in late-type stars that the synthetic spectrum becomes indispensable even when the study is based on a high dispersion. The synthetic spectra also make it possible to determine accurate abundances from the low-dispersion spectra and even from the colours without a cumbersome empirical calibration based on stars studied with higher spectral resolution which may not always be available. The method of spectrum synthesis incorporates the use of detailed model atmospheres and it is necessary that detailed calculations be made for all spectral features providing information about the structure of the star's atmosphere. In the method of spectrum synthesis, the calculations are not confined to weak lines alone. Important luminosity indicators are generally based on strong and frequently blended features. In order to reproduce them, it is necessary to calculate a wide region of the spectrum point by point. LTE spectrum synthesis is described by Ross and Aller (1968) who applied it for a determination of Cr I abundance in the solar atmosphere.

2.6 Computation of the Theoretical Spectrum

The flow of radiation through the stellar atmosphere is described by the equation of radiative transfer. The equation of radiative transfer in a plane-parallel atmosphere

(the thickness of photosphere $\Delta x \ll$ radius R of the star) is given by

$$\cos \theta \frac{dI_\nu}{d\tau_\nu} = -I_\nu + S_\nu \quad \dots (2.9)$$

Here, θ is the angle between the direction of the beam and normal to the radiating surface. S_ν is source function which is the ratio of emission coefficient to absorption coefficient, I_ν is the specific intensity and τ_ν the optical depth.

The integrated form for emergent intensity is given by

$$I_\nu(\theta) = \int_0^\infty S_\nu e^{-(t_\nu - \tau_\nu) \sec \theta} \sec \theta dt_\nu \quad \dots (2.10)$$

The specific intensity is relevant for solar work where intensity measurement can be made as a function of θ . For most of the stars, however, we must deal with flux. The emergent flux is given by

$$F_\nu(0) = 2\pi \int_0^\infty S_\nu(t_\nu) E_2(t_\nu) dt_\nu \quad \dots (2.11)$$

Where $E_2(t_\nu)$ is the exponential integral of the form

$$E_n(x) = \int_0^\infty \frac{e^{-xw}}{w^n} dw \quad \dots (2.12)$$

We can infer from equation (2.12) that the surface flux is composed of the sum of the source function at each depth multiplied by an extinction factor $E_2(t_\nu)$ appropriate to that depth; the sum is taken over all depths contributing a significant amount of radiation at the surface. If we denote continuum absorption coefficient by K_λ and continuum source function by S_λ the emergent flux in continuum will be given by

$$F_\lambda(0) = 2 \int_0^\infty S_\nu(\tau_\lambda) E_2(\tau_\lambda) d\tau_\lambda \quad \dots (2.13)$$

2.6.1 The Continuum flux contribution function

If K_r is the continuous absorption coefficient at a reference wavelength r (say 5000\AA), the geometrical depth can be defined as

$$dl = \frac{d\tau_r}{K_r \rho} \quad \dots (2.14)$$

The optical depth τ_λ and hence the continuous absorption coefficient K_λ at any arbitrary wavelength can be expressed in terms of τ_r and K_r by

$$dl = \frac{d\tau_r}{K_r \rho} = \frac{d\tau_\lambda}{K_\lambda \rho} \quad \dots (2.15)$$

Hence,

$$\tau_{\lambda} = \int_0^{\tau_r} \frac{\kappa_{\lambda}(t_r)}{\kappa_r(t_r)} dt_r$$

or

$$\tau_{\lambda} = \int_{-\infty}^{\log \tau_r} \frac{\kappa_{\lambda}(\tau_{\lambda})}{\kappa_r(\tau_r)} \tau_r \frac{d \log \tau_r}{\log e} \quad \dots (2.16)$$

Using equation (2.16), the expression for emergent continuum flux can be written as

$$F_{\lambda}(0) = 2 \int S_{\lambda}(\tau_r) E_2(\tau_{\lambda}) \frac{\kappa_{\lambda} \tau_r}{\kappa_r} \frac{d \log \tau_r}{\log e} \quad \dots (2.17)$$

The amount of light contributed to the surface flux as a function of depth in the atmosphere is specified by the integrand of equation (2.17). This integrand is known as flux-contribution function. It shows at what depth the surface flux originates and where, for example, $T(\tau_r)$ must be defined in order to compute the surface flux. Figure (2.2) shows the flux-contribution function for different wavelengths in the spectrum of a solar model. It is clear from the figure that the radiation at 8000\AA is formed higher in the atmosphere than the radiation at 5000\AA . This reflects in part the smaller absorption at 5000\AA . A good illustration of the concept of the depth of formation arises in a discussion of the behaviour of the model flux above and below the Balmer discontinuity. As shown in Figure (2.3),

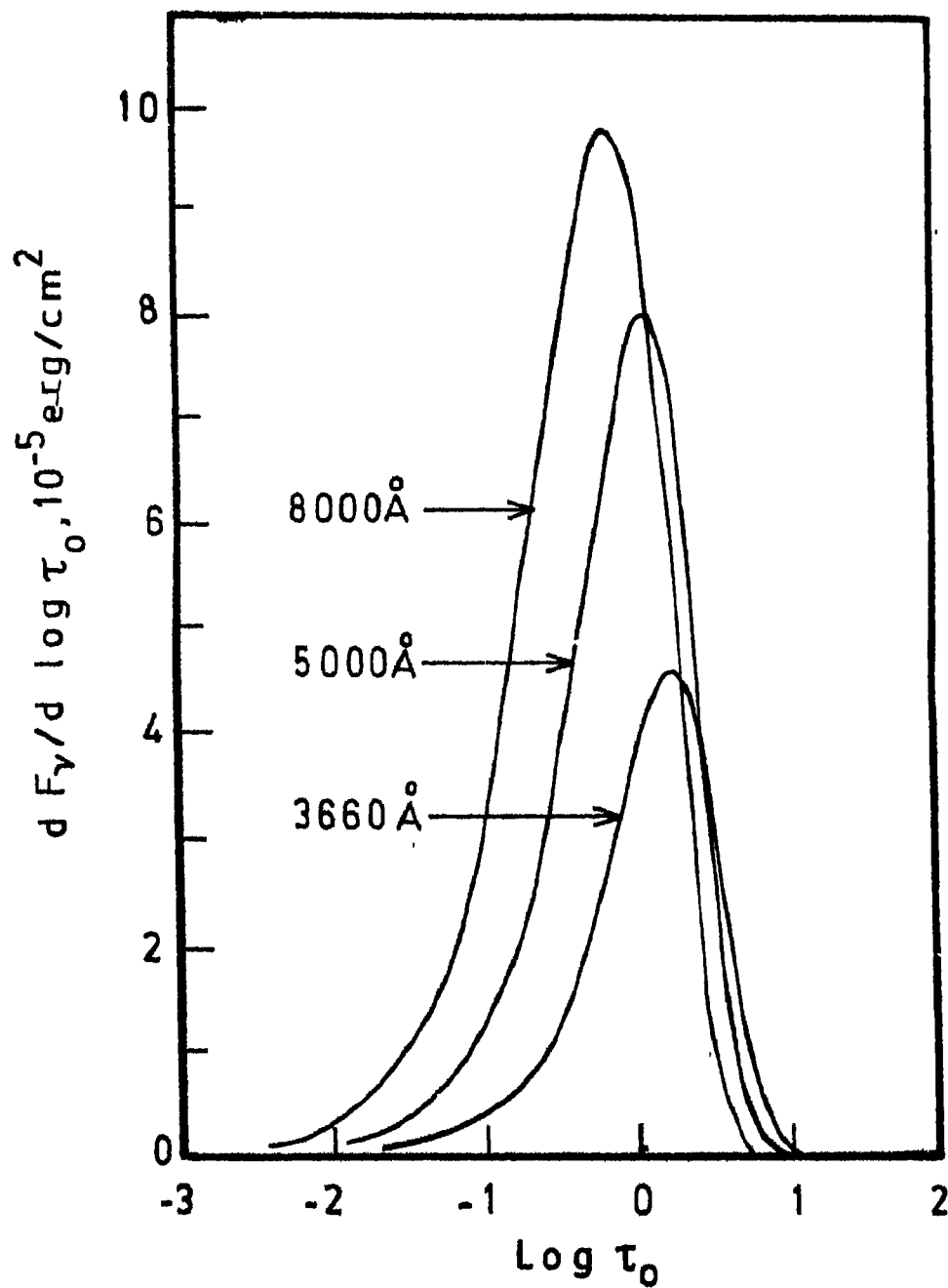


Figure 2.2 Continuum flux contribution functions at various wavelengths for a solar model (Gray 1976).

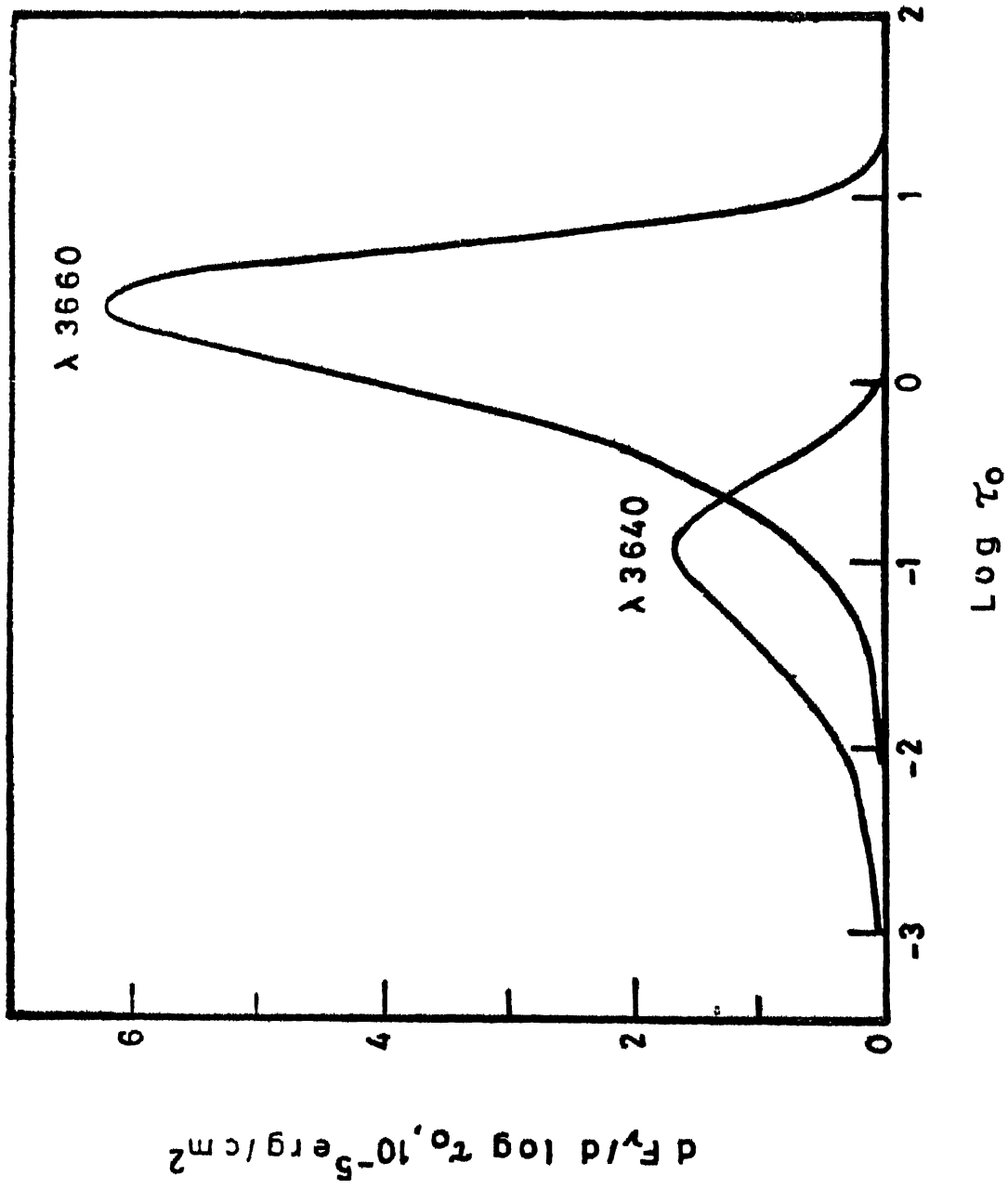


Figure 2.3 Continuum flux contribution functions longward (3660 Å) and shortward (3640 Å) of Balmer discontinuity for a solar model (Gray 1976).

the flux at 3650\AA arises in significantly deeper layers than the flux at 3640\AA . The depth of formation is dependent upon the temperature of the model. Changes such as shown in Figure (2.4) are typical.

2.6.2 The line spectrum

A line in the stellar spectrum is characterised by its profile which is the observed distribution of energy as a function of frequency (or wavelength). Excepting the Sun, we observe for all other stars only the flux integrated over the entire disc of the star. We measure the line flux F_1 with respect to the continuum flux F_c and describe the profile in terms of its absorption depth

$$D_\nu = 1 - R_\nu = 1 - \frac{F_l}{F_c} \quad \dots (2.18)$$

where R_ν is the residual flux.

2.6.3 The line transfer equation

The transfer equation (2.9) holds for line as well continuum radiation, provided the variables are suitably defined. If κ_l denotes the line absorption coefficient and j_1 the line emission coefficient and if κ_c and j_c are the corresponding parameters for continuum, by defining

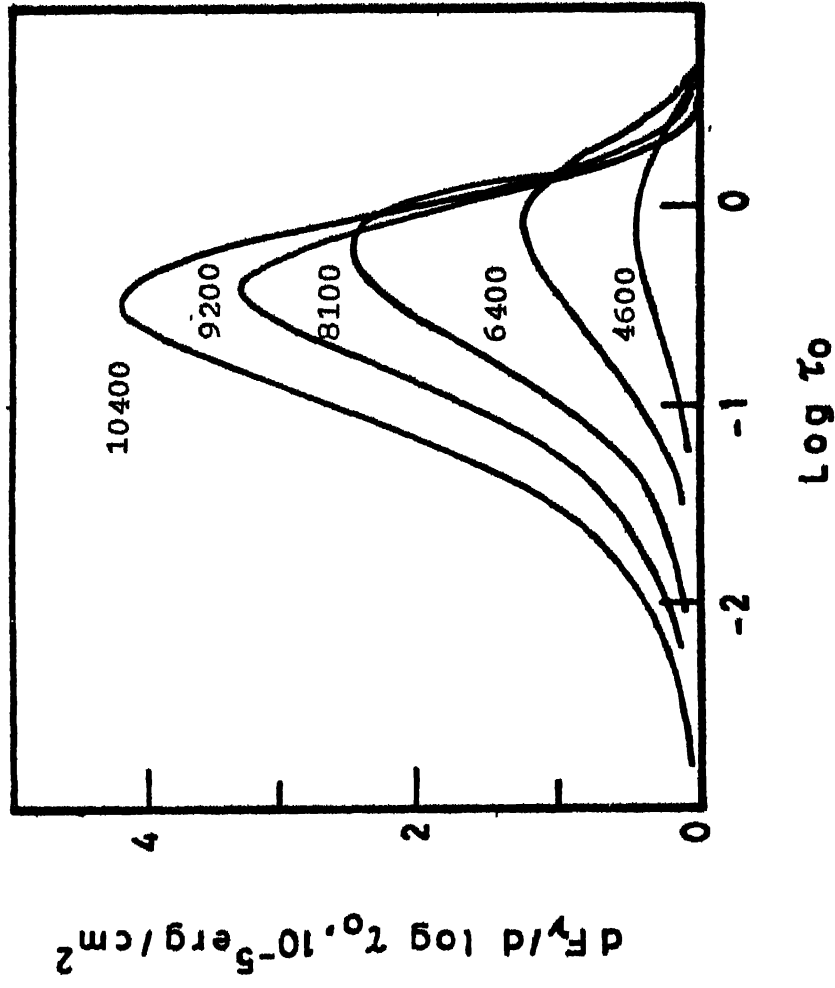


Figure 2.4 Continuum flux contribution functions at $\lambda = 7000 \text{ \AA}$ for various temperatures, for a solar model (Gray 1976).

$$d\tau_v = (\kappa_l + \kappa_c) \rho dx. \quad \dots (2.19)$$

and source function

$$S_v = \frac{j_l + j_c}{\kappa_l + \kappa_c}$$

we can write

$$\frac{dI_v}{d\tau_v} = -I_v + S_v.$$

The integral form of the transfer equation still holds.

The surface flux would be given by

$$F_v(0) = 2\pi \int_0^{\infty} S_v(\tau_v) E_2(\tau_v) d\tau_v. \quad \dots (2.20)$$

The equivalent width of a line can be expressed as

$$W = \int_{-\infty}^{\infty} D(\Delta\lambda) d\Delta\lambda, \quad \dots (2.21)$$

where $\Delta\lambda$ is the wavelength displacement from the line centre

and $D(\Delta\lambda)$ is the line depth at a displacement $\Delta\lambda$. $D(\Delta\lambda)$

is related to residual flux by

$$D(\Delta\lambda) = 1 - R(\Delta\lambda) \quad \dots (2.22)$$

where

$$R(\Delta\lambda) = \frac{2}{F_c(0)} \int_0^{\infty} S_v(\tau_l + \tau_c) E_2(\tau_l + \tau_c) d(\tau_l + \tau_c). \quad \dots (2.23)$$

Here, the continuum flux is defined by

$$F_c(0) = 2 \int_0^{\infty} S_c(\tau_c) E_2(\tau_c) d\tau_c. \quad \dots (2.24)$$

$S_y(\tau_c)$ and $S_y(\tau_l + \tau_c)$ are the source functions of the continuum and the line-plus-continuum respectively. Hence,

$$D(\Delta\lambda) = \frac{2}{F_c(0)} \left\{ \int_0^{\infty} S_c(\tau_c) E_2(\tau_c) d\tau_c - \int_0^{\infty} S_y(\tau_l + \tau_c) E_2(\tau_l + \tau_c) d(\tau_l + \tau_c) \right\}. \quad \dots (2.25)$$

If the stellar atmosphere is assumed to be in local thermodynamical equilibrium, then the source functions are merely Planck's function $B(\tau)$. If the temperature distribution in the stellar atmosphere is known as a function of τ_r (a reference optical depth scale), then, using

$$\tau_c = \int_0^{\tau_r} \frac{\kappa_c}{\kappa_r} d\tau_r$$

and

$$d(\tau_c + \tau_r) = \left\{ 1 + \frac{\kappa_l}{\kappa_c} \right\} d\tau_c,$$

we obtain

$$D(\Delta\lambda) = \frac{2}{F_c(0)} \int B_\lambda(\tau_c) \left\{ E_2(\tau_c) - \left[1 + \frac{\kappa_l}{\kappa_c} \right] E_2(\tau_l + \tau_c) \right\} d\tau_c. \quad \dots (2.26)$$

In the situations where the portion of the model spectrum being computed includes several lines, it is only necessary to add the absorption coefficients of all the contributing lines. Then κ_λ in equation (2.26) is replaced by the sum of line absorption coefficients with each κ_λ evaluated at proper $\Delta\lambda$, the wavelength difference from the centre of the line to the position of interest. Now, by defining $x = \log(\tau_r)$ and $dx = \frac{d\tau_r}{\tau_r}$, the depth equation can be written as

$$D(\Delta\lambda) = \frac{2}{0.4343 F_c(0)} \int_{-\infty}^{\infty} \frac{\tau_r \kappa_c}{\kappa_r} B_\lambda(T) \times \left\{ E_2(\tau_c) - \left[1 + \frac{\kappa_l}{\kappa_c} \right] E_2(\tau_l + \tau_c) \right\} dx \quad \dots (2.27)$$

where

$$F_c(0) = \frac{2}{0.4343} \int_{-\infty}^{\infty} \frac{\kappa_c(\tau_r)}{\kappa_r} B_\lambda(T) E_2(\tau_c) dx. \quad \dots (2.28)$$

Integrand of equation (2.27) is called the contribution function to the line depth (C_D). We can thus write

$$D(\Delta\lambda) = \int_{-\infty}^{\infty} C_D(\Delta\lambda, x) dx. \quad \dots (2.29)$$

Slight variations exist in the literature in the definition of the contribution functions. For example,

contribution function for residual flux $C_R (\Delta\lambda, x)$ and contribution function to equivalent width $C_W (\Delta\lambda, x)$ are used by different workers. The concept of the contribution function was first introduced by Ten Bruggencate, Lust-Kulka and Voigt (1955) and has been used by numerous investigators (e.g. Goldberg and Pierce 1959; Edmonds, Michard and Servajean 1965). These contribution functions provide an indication of the contribution to the aspect of spectral line formation coming from different layers of the stars. Equation (2.28) is perfectly general; it applies to strong as well as weak lines and provides in a simple way for the depth dependence of parameters.

Contribution function of the form used in equation (2.27) will be negative at small optical depths since $(\kappa_c + \kappa_l)/\kappa_c$ is always greater than one. When τ_c is of the order of unity, the self absorption term $E_2 (\tau_l + \tau_c)$ goes rapidly to zero decreasing the importance of the negative term and the contribution function becomes positive. The integral of the contribution function from 0 to say τ^* gives the line depth that would be observed if the atmosphere from τ^* to ∞ were missing. Negative part of the contribution function tells us that without the deeper layer we would be observing emission lines - which is not surprising. It is only when these layers are observed with a hotter continuum behind, that one gets absorption lines.

CHAPTER 3

OBSERVATIONS AND DATA REDUCTIONS

3.1 Selection of Programme Stars:

Galactic distribution of all Cepheids brighter than $m_v = 9.0$ was studied to select the stars suitable for abundance gradient determination. Figure(3.1) shows the distribution of programme stars in the galactic plane. Young open clusters and H II regions are also shown in the same figure to bring out the spiral arms. We selected the stars which lie approximately along a straight line from $l = 20^\circ$ to $l = 200^\circ$. The stars SV Mon and T Mon are chosen towards the galactic anticentre while X Sgr and WZ Sgr are chosen towards galactic centre. ζ Gem was taken as representative of the local arm population. The sample of stars encompasses a range of 4.2 kpc around the sun - 2.5 kpc towards galactic anticentre and 1.7 kpc towards galactic centre.

Table 3.1 contains the basic data for the programme stars. The coordinates, magnitudes, mean spectral types and luminosity classes are taken from the General Catalogue of Variable stars of Kukarkin et al (1969). The distances listed in the table are calculated using P-L-C relationship of Sandage and Tammann (1968) and using the colour excesses

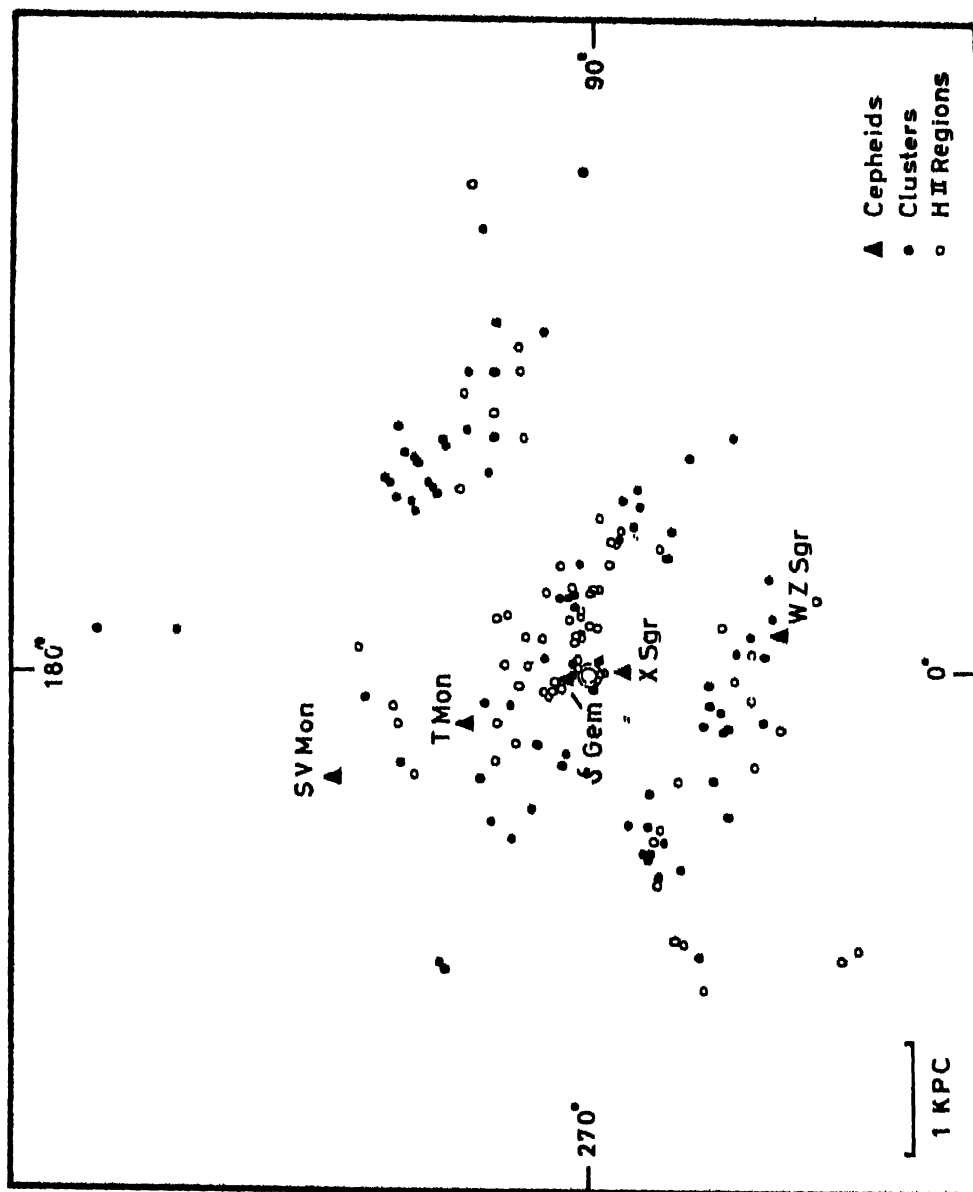


Figure 3.1 Distribution of the programme Cepheids in galactic plane with the spiral arms traced by young open clusters and H II regions (based on Becker and Fenkart 1970).

Table 3.1

Basic data on the Programme Stars

Star	RA(1900) DEC(1900)	l deg b deg	Spectral type	Max Min	V	P days	Epoch JD	r gc kpc
X Sgr	17 41 16 -27 47.6	1.2 0.2	F5-G1	4.24	4.84	7.01225	36968.85	8.13
ζ Gem	06 58 11 20 43.1	195.7 11.9	F7-G3 Ib	3.66	4.16	10.1535	10639.80	8.87
T Mon	06 19 49 -07 08.4	203.6 -02.6	F7-K1 Iab	5.59	6.60	27.0205	36137.09	10.14
SV Mon	06 16 04 06 30.9	203.7 -02.68	F8-K5	7.8	8.9	15.2316	36437.07	10.87
WZ Sgr	18 11 06 -19 06.6	12.11 -01.39	G3-K6	8.4	10.1	21.8497	35506.63	6.74

published by Nikolov and Ivanov (1974). The periods and epochs of the minima were taken from Schaltenbrand and Tamman (1971).

Long-period Cepheids of the disk population are known to be relatively young objects. Kippenhahn and Smith (1969), from the evolutionary tracks for massive stars, derived a relationship between the age and the period of Cepheids. According to their calculations, all Cepheids with periods greater than 15 d should be as young or younger than 2×10^7 yr and for the Cepheids of 11.2 d period, the average age estimate was $\sim 3 \times 10^7$ yr. While selecting the programme stars, we preferred Cepheids with periods longer than ~ 10 d and excepting X Sgr ($P = 7.0125$ d) all of them satisfy this condition.

3.2 Details of Observational Data

All the spectrograms used in the present investigation were obtained with the 102-cm reflector telescope of Kavalur Observatory. The spectrograph used at the Cassegrain focus is designed by late Professor M.K.V. Bappu and fabricated at the Indian Institute of Astrophysics. The collimator mirror of the spectrograph has a focal length of 70cm. The reflection grating with 1800 grooves mm^{-1} blazed at 5000\AA in the first order, when used with a camera of 50cm in focal length gives a dispersion of $11.3\text{\AA} \text{mm}^{-1}$. Bright stars like

X Sgr, T Mon and ζ Gem were observed at this dispersion. The same system with a camera of 25cm focal length gives a dispersion of 22.6\AA mm^{-1} .

A Varo 8605 single-stage image-intensifier tube is placed at the focus of the camera and the spectra were recorded either on IIA-D or on 103a-D plates in contact with the fibre-optic output window of the image tube. The grating was used at positive angles (i.e. blaze direction towards the collimator). Such an arrangement reduces the light loss at the grating considerably (Hollars and Reitsema 1974).

Durations of the exposures were limited by the image-tube background noise which reaches a density of 0.05 above chemical fog in 150 minutes in the winter (ambient temperature $\sim 18^{\circ}\text{C}$) and in 90 minutes in spring (ambient temperature $\sim 25^{\circ}\text{C}$).

The slit width of the spectrograph was adjusted for each camera in such a way that the projected slit width on the plate was $20\ \mu\text{m}$. The star was trailed along the length of the slit to get a well-widened spectrum. The widening varied from 0.3mm to 0.5mm depending upon the brightness of the star. One can record a 0.4mm wide spectrum of a star of 6.5 mag in 90 minutes with the 50cm camera. With the 25cm camera we can reach a magnitude of 8.0 with the same

widening. Table 3.2 lists the details of the observational data. The last two columns contain the duration of the exposure as a fraction of the pulsation period and the mean phase at the middle of exposure. Since all of our programme stars have sufficiently long periods and the exposure times of less than 150 minutes, it is reasonable to assume that there was no phase change in the star during the exposure.

For each spectrogram, a calibration plate was simultaneously exposed in an auxiliary calibration spectrograph. The calibration set up consists of a Hilger quartz spectrograph, a rotating sector and a Tungsten filament source. The calibration and stellar spectrograms are developed together for four minutes in Kodak DA-19b developer at 20°C.

3.3 Reductions of the Photographic Spectra

An image is stored in the photographic plate in the form of blackened silver grains in varying degree of blackening. To determine the intensity of the radiation that blackened the photographic grains, one needs to know the response of the photographic material to the incident light. The response of a photographic emulsion is described through what is called the characteristic curve of the emulsion. A good calibration should be able to show the plate response for a considerable range of light intensities.

Table 3.2

Journal of Observations

Plate No	Star	Dispersion \AA mm^{-1}	Spectral Region \AA	Epoch of Observation	Duration of Exposure ϕ	Phase ϕ
δ 1089	X Sgr	11.3	4300-4500	1980 Sep 26.604	0.0010	0.258
δ 1105	X Sgr	11.3	4400-4600	1980 Sep 27.595	0.0010	0.394
δ 1147	ζ Gem	11.3	4450-4650	1980 Oct 26.937	0.00015	0.238
δ 1180	ζ Gem	11.3	4450-4650	1980 Nov 7.915	0.00015	0.427
δ 1361	SV Mon	22.6	4300-4600	1981 Jan 31.737	0.0055	0.286
δ 1418	SV Mon	22.6	4300-4600	1981 Feb 16.625	0.0055	0.334
δ 1563	WZ Sgr	22.6	4200-4500	1981 Mar 24.958	0.0045	0.219
δ 1683	WZ Sgr	22.6	4400-4700	1981 Oct 9.708	0.0045	0.941
δ 1161	T Mon	11.3	4500-4700	1980 Nov 2.929	0.0012	0.219
δ 1182	T Mon	22.6	4300-4600	1980 Nov 30.845	0.0006	0.254

The degree of blackening is usually expressed by optical density of the photographic silver deposit. Suppose I_0 is the light intensity falling on a photographic image and only a fraction I_t is transmitted through it; then, I_t/I_0 is the transmittance T of the plate. For a clear plate which is not exposed to any light before developing, $I_t = I_0$, or we can say the transmittance $T = 1$. If the plate is darkened so much that $I_t = 0$, then $T = 0$.

Earlier, observers used percentage deflection (either $T \times 100$ or $(1-T) \times 100$) as a measure of optical density and plotted it against the exposure E ($I \times t$ where t is the duration of exposure and I the intensity of light); but such a curve would show saturation within a very small range of densities. Hurter and Driffield plotted optical density $D = \log 1/T$ against the logarithm of exposure. With this new parameter, the saturation was reached at much higher densities. This curve was adopted by a number of observers and the term characteristic curve became almost synonymous with the one proposed by Hurter and Driffield (HD curve). The well-known shape of the curve is responsible for the general concept that the response of a photographic plate is inherently non-linear. Various attempts were made by different groups of observers to fit suitable functions to this non-linear curve. Baker (1925) introduced a function $D_1 = \log (10^D - 1)$ (which is now known as 'the Baker density')

that gave a linear curve even at a very low density (where the toe used to appear in the HD curve) and the saturation came at much higher densities. de Vaucouleurs (1968) called $10^D - 1$ as opacitance (ω) because of its relation to opacity ($\omega = \frac{1}{T} - 1$). He constructed characteristic curves for several emulsions using this parameter plotted on a logarithmic scale. These curves are strictly linear at low and intermediate densities which are of practical importance in Astronomical photometry.

We have used the Baker density ($\log \omega$) for our calibration curves. Figure(3.2) shows calibration curve for the plate δ 1361. One can clearly see the absence of toe in the low-density region and a slight deviation from non-linearity comes only after $D = 1.2$. Since our plates were never darker than $D = 0.6$, a straight-line least-squares fit (excluding the highest densities) was adequate.

Smoothing: The image stored in a photographic emulsion is a degraded picture of the original information. The most severe degradation affected by this form of storage is the addition of grain noise. One cannot get rid of the noise by simply increasing the signal, since the noise is an increasing function of photographic density. Hence, it is necessary to devise an effective method of noise removal from the record before the information is analysed.

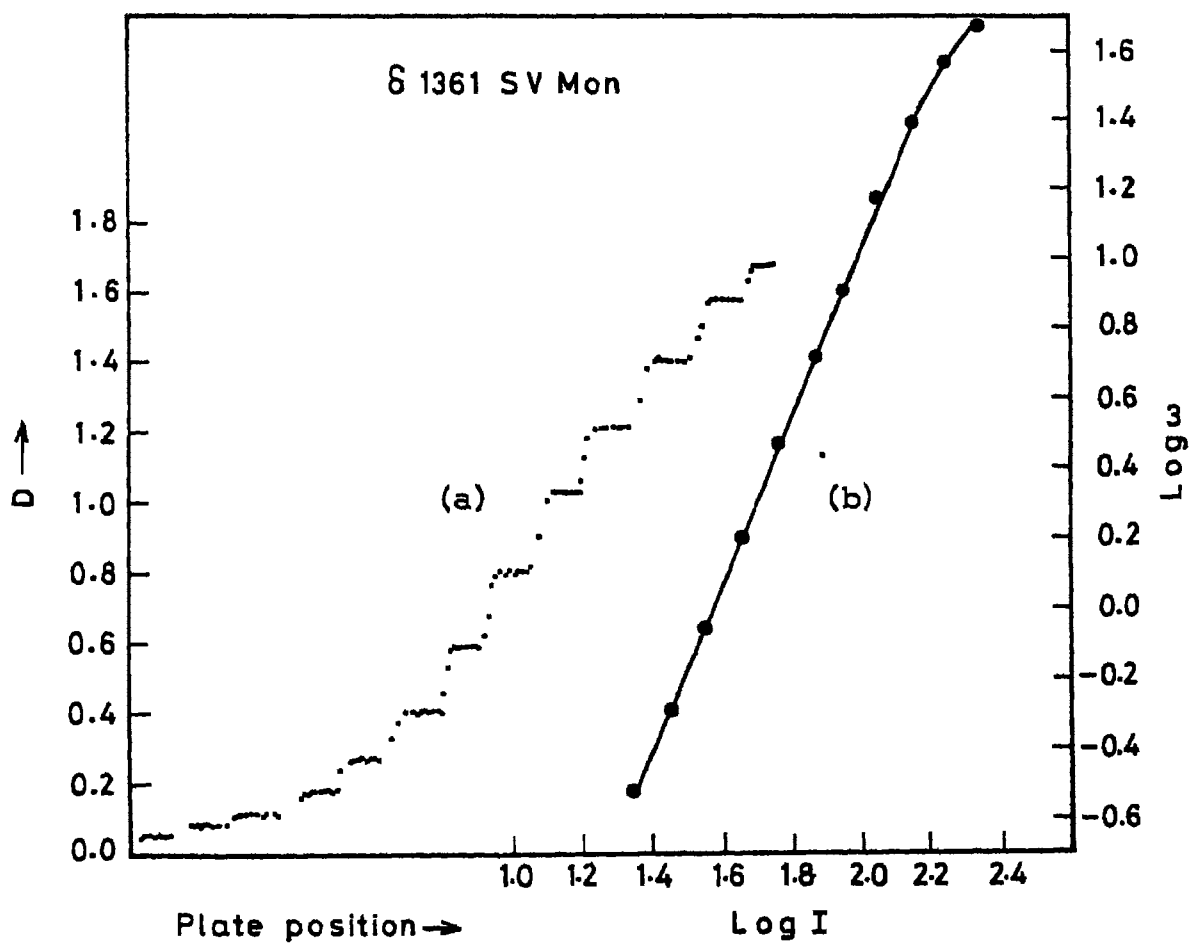


Figure 3.2 (a) Density steps in the calibration plate and (b) the characteristic curve determined from them.

Fortunately, in frequency domain the photographic noise decreases with increasing wavelength. Thus, it is possible to retrieve the information at longer wavelengths and discard the one at shorter wavelengths which is affected by noise. The best way of noise removal lies in the frequency domain where one can use the pre-knowledge of the shapes of the noise function and the signal function to separate the two.

A very much simpler technique is to cut off the frequencies higher than the ones transmitted by the apparatus function (instrumental and detector). This is the technique of low-pass filtering utilized in its simplest form by a conventional researcher by drawing a smooth curve by hand over the analog record. This method generally meets the problem of delicate balance between skill and subjectivity.

The digital low-pass filters which are more objective and fairly quick even with the simplest of modern digitizing equipment are constructed on the principle of the weighted running average. The running average with equal weights has side-lobes in the frequency domain and hence degrades the overall resolution. A triangular function is very much better. This is equivalent of a hanning window used in Fourier analysis. A further improvement is a hamming window which has weights 0.23, 0.54, 0.23 in the data domain, when 3-point averages are used. Since our apparatus function has a half-width of $40\mu\text{m}$ (see section 3.5) and the digitization

interval is $8\mu\text{m}$ the 3-point triangular profile smoothens the spectra sufficiently without degrading the resolution.

Signal-to-Noise Ratio: A quantity which represents the precision with which the incident radiant energy is determined is the signal-to-noise ratio. Consider an experiment in which identical exposures are given to a number of plates. The density of any specified image will not exactly be the same on each plate because of the factors such as granularity and non-uniformity. These density differences form a normal distribution with a well-defined mean D and standard deviation σ_D , and with a corresponding mean $\log E$ and uncertainty $\sigma_{\log E}$. The precision in $\log E$ is closely related to the signal-to-noise ratio (S/N). E/σ_E is related to density fluctuations σ_D , by the local slope of the characteristic curve γ .

$$\frac{S}{N} = \frac{E}{\sigma_E} = \frac{1}{\sigma_{\ln E}} = \frac{0.4343}{\sigma_{\log E}} = \frac{0.4343\gamma}{\sigma_D}$$

Signal-to-noise ratio is an extremely useful quantity as it allows us to estimate the fractional precision with which the exposure in any image element is determined from a single measurement. A S/N ratio of 10 means that the determination of exposure is uncertain by 10% and a S/N ratio of 1000 corresponds to 0.1% precision.

Let us now consider the effect of background exposure on the signal-to-noise ratio. By background exposure we mean the plate density which is caused by undesirable light such as the sky background or image-tube background. The undesirable intensity which is not caused by exposure to light is referred to as plate fog which contributes to the noise but not to the signal; this contribution is automatically included in the determination of σ_D .

Background exposure E_B is mixed with the stellar exposure E_S . The net S/N is related to the background and the total exposure $E_T = E_S + E_B$ by the relation:

$$\text{Net} \left(\frac{S}{N} \right) = \frac{E_T - E_B}{E_T} \cdot \left(\frac{S}{N} \right)$$

In our spectrograms, the density of image-tube background was always between 0.02 and 0.04. It affects S/N by 5 to 10%. After applying this correction, the S/N of our spectrograms is generally ~ 120 and never below 100 even for the fainter stars. After applying a 3-point smoothing, S/N improves further by a factor $\sqrt{2}$ or by 41%, since the effective number of points used in obtaining the average value is 2.

3.4 Digitization and Reduction of the Raw Data

The stellar spectrograms were traced on the Carl Zeiss microphotometer. The microphotometer is automated

utilizing a microcomputer HCL MICRO 2200 (Viswanath 1981).

The hardware of this automated microphotometer consists of a position sensor, digitizer system interface and control logic, microcomputer, microdata interface (MDI) and a floppy disk attachment (FDA).

Positional sensor is an incremental shaft encoder which gives 500 pulses per revolution with quadrature output. This is coupled to a gear inside the potentiometric recorder of the microphotometer such that it gives one pulse for every $8\ \mu\text{m}$ linear displacement of the photographic plate. This pulse is the basic clock for the system and the digitization and data transfer is done on the arrival of this pulse.

The digitizer system is an analogue-to-digital converter (A/D) of three decimal digits and digitizes the analogue voltage from the potentiometric recorder of microphotometer. MICRO 2200 is a desk-top computer with 2000 programming steps and 200 data registers. MDI is a digital input/output point through which MICRO 2200 handles the memory backup; each floppy disk has the capacity to store 30,000 programming steps and 3000 data points.

Various programmes (written in a language similar to BASIC) required at different stages of reduction are stored in different locations of the disk. A typical run of the spectrophotometric reductions is described below:

- i) Using the programme to log the deflections, the calibration plate is digitized and the deflections (measured from the dark level) are stored in the disk.
- ii) A routine calculates the average D , σ_D and $\log \omega$ for a specified number of points.
- iii) By plotting these densities against the plate position we can see various density steps as shown in Figure (3.2a). The values of σ_D help in evaluating S/N as a function of photographic density or $\log \omega$ as the height and width of the slit of the microphotometer are kept the same for the calibration plate as for the stellar spectrograms. The average $\log \omega$ of each step is determined the next. The characteristic curve is determined using a curve-fitting routine.
- iv) The stellar spectrum is also digitized using the programme to log the deflections. Another routine searches for the minimum deflections in each set of 100 points. The continuum is defined by choosing from the highest points only those that have reached the continuum.
- v) The unexposed portion of the plate just above and below the stellar spectrum is also traced and

digitized in a similar way in order to determine the image-tube background. The average value of the background is determined at every 1 mm on the plate. The image tube background is non-uniform, being lesser at the edges of the plate and increasing towards the centre.

- vi) The deflections corresponding to the stellar spectrum are smoothed by a three-point triangular smoothing function using the weights 0.25, 0.5 and 0.25. These smoothed deflections are converted to $\log \omega$ and then to $\log I$ by using the coefficients of the power-law fit obtained earlier. The image-tube background is subtracted from these intensities which are then converted to $1/I_c$ using the predetermined continuum.

The Final Spectrum Plots: Since the microphotometer readings are at arbitrary steps in wavelength, the data must be transferred to standard wavelength steps. Firstly, using the intensity values as a function of plate position, the spectral lines were identified using a routine which searches for lines deeper than a specified depth. A 4-coefficient least-squares-fit is made to these wavelengths as a function of plate position. Accuracy of such a fit was found to be about ± 3 data points which is less than the resolution. With plate position - wavelength conversion

constant known, the intensities are interpolated to regular steps in wavelength (say 0.1\AA). This enables one to compare the observed spectrum with the calculated spectrum with greater ease.

Equivalent Widths: The abundance analysis reported in this investigation is based on the general fit of the observed spectrum and the computed spectrum. Thus, the equivalent widths of the individual lines is generally not necessary. However, equivalent widths of some lines are useful in improving various atmospheric parameters and in the error analysis. Thus, the equivalent widths help in the spectroscopic estimation of atmospheric parameters.

When the individual spectral lines do not reach the continuum because of crowding, and the blending is not yet too severe to affect the central depths of the individual absorption lines, the equivalent widths can be indirectly estimated if a calibration between the central depths and the equivalent widths is first determined using unblended lines. Hence, a representative sample of the narrowest lines in the spectrum were measured for their equivalent widths using a trapezoidal integration method. A least-squares straight-line fit to these equivalent widths is made as a function of their residual intensities. Figure (3.3) shows such a function for the plate $\delta 1161$ of T Mon. The residual of other lines needed in the estimation of

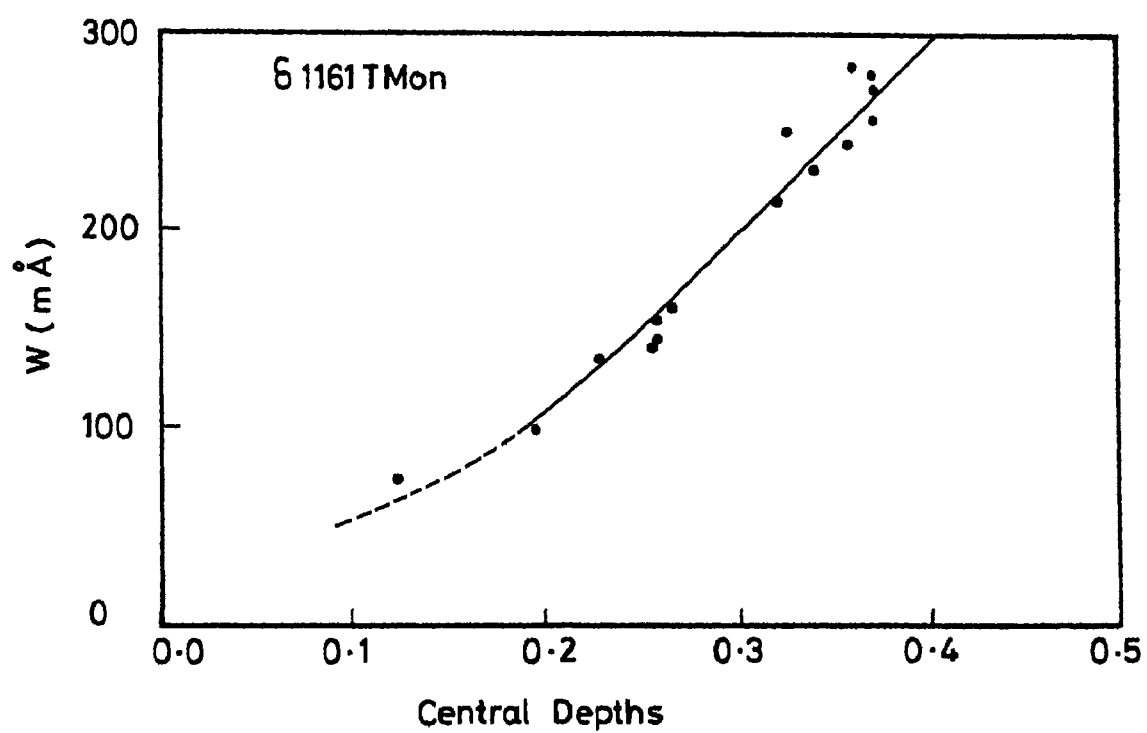


Figure 3.3 The relationship between the equivalent widths and the central depths of absorption lines of Fe.

atmospheric parameters are converted to the equivalent widths using a similar relationship. Equivalent widths estimated in such a fashion would be more accurate than the ones obtained by extrapolating the wings to the continuum.

3.5 The Instrumental Profile

Distortion of the stellar spectrum can be caused by inadequate spectral purity, detector resolution, diffraction and other aberrations. Measurement of the instrumental profile tells us how much degradation occurs and to some extent allows us to reconstruct the original image prior to blurring.

Consider a light source giving an infinitely narrow spectral line. Such a line can be denoted by $\delta(\lambda - \lambda_0)$ where λ_0 is the central wavelength. The profile of this δ -function source measured with the instrument of interest is the instrumental profile $I(\lambda)$. A general spectrum can be viewed as a synthesis of functions with their heights modulated by the flux $F(\lambda)$. Each of these δ -functions gives an $I(\lambda)$ in the output spectrum each shifted to the wavelength of the δ -function. The data actually recorded is then the sum of these shifted $I(\lambda)$'s, so that the observed spectrum is

$$D(\lambda) = \int_{-\infty}^{\infty} I(\lambda - \lambda_0) F(\lambda_0) d\lambda_0$$

or

$$D(\lambda) = I(\lambda) * F(\lambda).$$

The data is the convolution of the instrumental profile with the true flux spectrum. When a spectral line is intrinsically broader (such as due to rotation in early type stars) than the instrumental profile, it is easy to deconvolve the observed profile from the instrumental one and get the true profile. However, when the stellar line widths are comparable to the instrumental profile the iterative methods of deconvolution fail and the Fourier methods give rise to sidelobes. It is hence more convenient to convolve the theoretical spectrum with the instrumental profile and then compare it with the observed spectrum.

An iron-argon hollow-cathode lamp was used as a comparison source for the stellar spectrograms. We selected weak unblended lines of this source for determining the instrumental profile. These comparison lines were traced on the microphotometer and intensity profiles were determined. The line centre λ_0 was determined by parabolic interpolation. A linear fit between $\log I$ and $(\lambda - \lambda_0)^2$ was obtained for deriving the parameters of the Gaussian profile. Figure (3.4)

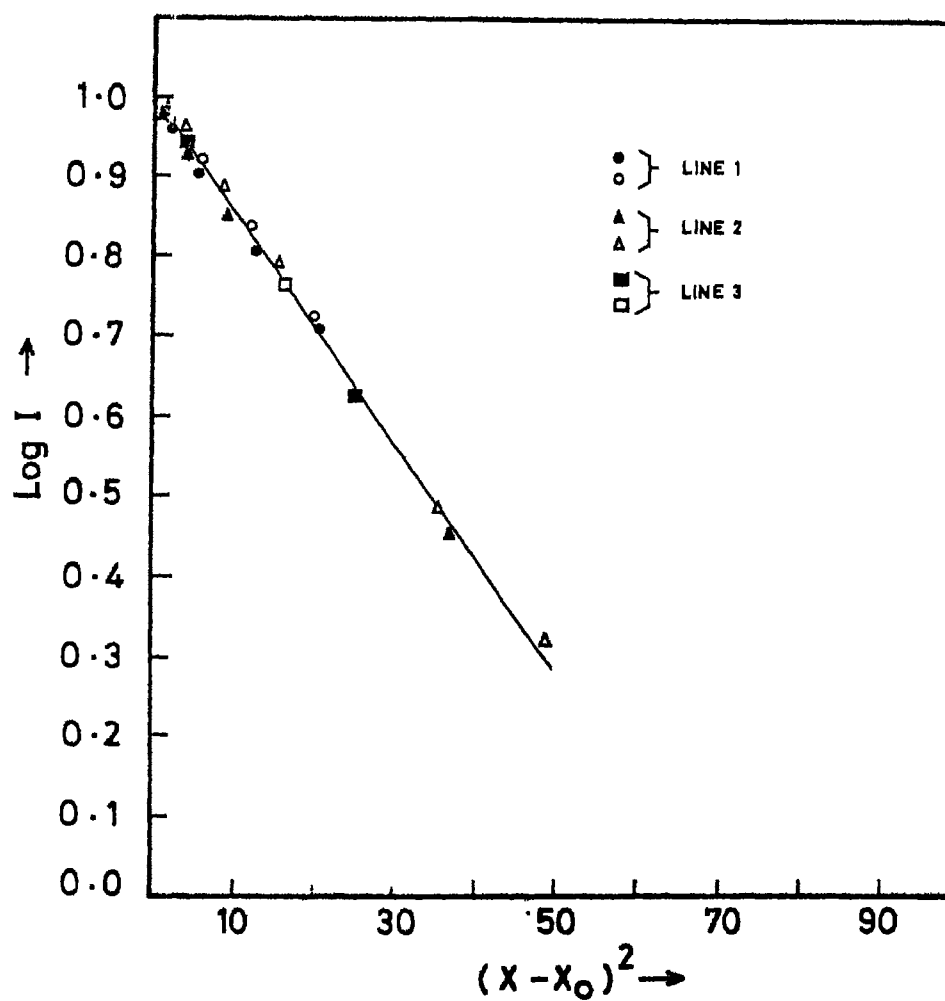


Figure 3.4 The instrumental profile determined from three comparison lines. The straight line is a gaussian fit.

shows the $\log I$ vs $(x-x_0)^2$ relationship for three such lines. The ordinates are normalised such that $\log I = 1.0$ at the line centre. Short-wavelength and long-wavelength wings of each line are shown by different symbols as explained in the figure caption. It is clear from the above figure that the instrumental profile can be represented by a Gaussian fairly well without significant asymmetry. The half-width of the apparatus profile corresponds to 0.9\AA at the dispersion 22.6\AA mm^{-1} and 0.45\AA at the dispersion of 11.3\AA mm^{-1} .

With these preliminary reductions of raw data, we are now ready to compare the observed spectrum with the theoretical spectrum, and deduce the atmospheric parameters and the chemical composition of these stars.

CHAPTER 4

METHOD OF ANALYSIS

4.1 Description of the Computer Programme

In this Chapter we will demonstrate the method of deriving the abundances of elements in stellar atmospheres using the spectrum synthesis method. In the synthesis method we attempt to duplicate the appearance of certain portions of the observed spectrum using a model atmosphere for the star and parameters of all known contributors to the line opacity in the region of interest.

Snedden's Spectrum Synthesis programme has been used after slight modification. Figure (4.1) gives the schematic block diagram of the program. Input to this programme consists of a model atmosphere and line parameters of all the relevant lines. Model atmospheres usually describe the variations of temperature, gas and electron pressure, and microturbulent velocities as a function of optical depth at a reference wavelength (say 5000\AA). The continuum opacities are calculated in subroutine OPACIT. Due to its overwhelming dominance in the stellar atmosphere, major contribution to continuous absorption comes from hydrogen in its various forms. Other smaller contributions due to helium absorption, and hydrogen and helium Rayleigh scattering are also included.

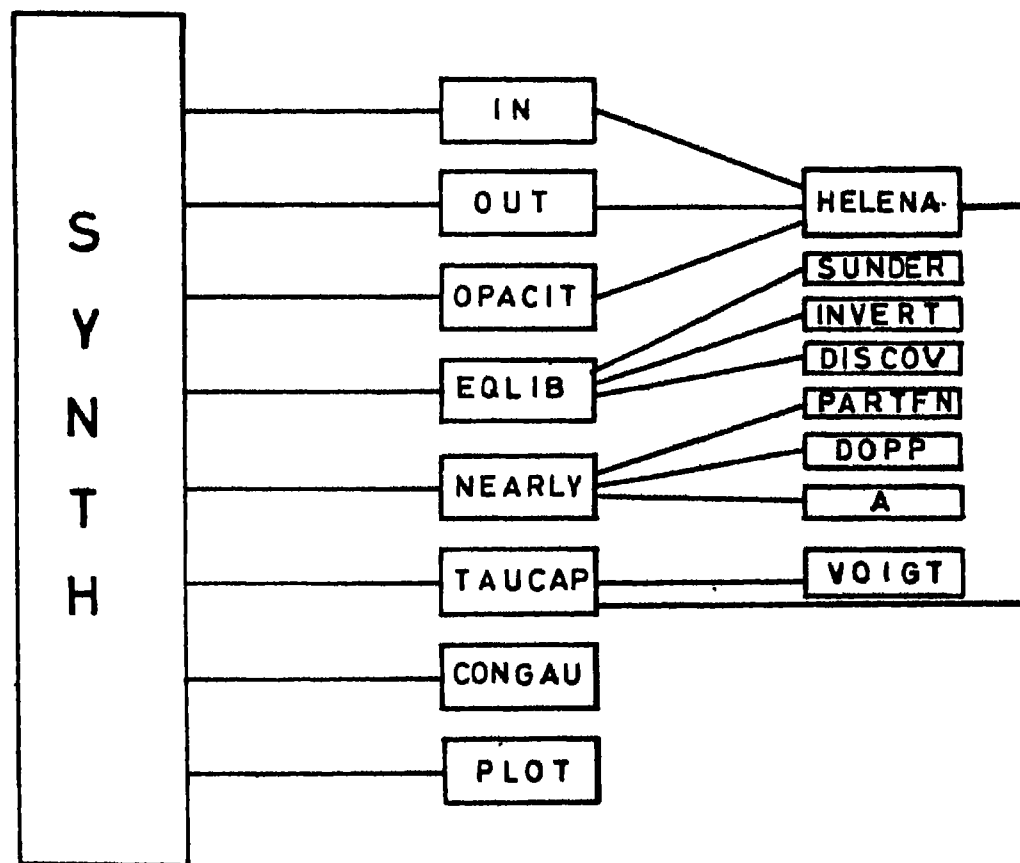


Figure 4.1 Block diagram of the synthesis programme.

These opacity formulations are such that opacity per neutral hydrogen (or neutral helium) atom is calculated. The total number density of hydrogen can be written as a sum of the number densities of all the species made from hydrogen.

$$N(\text{H})_{\text{tot}} = n(\text{H}^{\circ}) + n(\text{H}^{+}) + n(\text{H}^{-}) + n(\text{H}_2^{+}) \quad \dots (4.1)$$

and for helium, using the same analogy,

$$N(\text{He})_{\text{tot}} = n(\text{He}^{\circ}) + n(\text{He}^{+}). \quad \dots (4.2)$$

The number density of each component in equation (4.1) can be written as a function of neutral H and electron number densities by means of Saha equation. These equations relating the component number densities to the total number densities of hydrogen and helium are solved iteratively using Newton-Raphson technique and the number densities of all components are derived. We will briefly summarise various important contributors to continuum opacity in the following sections.

While describing the formulation of these absorption coefficients, frequency dependence of absorption coefficients is implicitly assumed and hence we drop the subscript λ for the sake of brevity.

Negative Hydrogen: The hydrogen atom is capable of holding a second electron in a bound state because the simple electron-proton combination is highly polarized. The ionization potential of H^{-} ion is 0.754 eV. The extra

electron needed to form H^- comes from ionized metals. In solar photosphere, H^- is proved to be the major source of continuous absorption. At temperatures higher than those in the solar photosphere H^- is deionised to such an extent that it ceases to be a strong absorber. On the other hand, for the cooler stars the supply of free electrons is much less for H^- ion to exist as a strong absorber.

H^- bound-free absorption coefficient $\kappa(H^-_{bf})$ can be expressed by

$$\kappa(H^-_{bf}) = n(H^-) a(H^-_{bf}) (1 - h\nu/kT) \quad \dots (4.3)$$

where $a(H^-_{bf})$ is the atomic absorption coefficient with the units of cm^2 per absorber. $(1 - h\nu/kT)$ is the stimulated emission factor; the absorption actually produced is lowered by the factor $(1 - h\nu/kT)$ because of the stimulated emission. The polynomial approximation to $a(H^-_{bf})$ is given by Gingerich (1964) is as follows:

$$a(H^-_{bf}) = 6.801 \times 10^{-20} + \frac{5.358 \times 10^{-3}}{\nu} + \frac{1.481 \times 10^{13}}{\nu^2} + \frac{-5.519 \times 10^{27}}{\nu^3} + \frac{4.808 \times 10^{41}}{\nu^4}$$

for $\nu \gg 2.111 \times 10^{14}$ and

$$a(H^-_{bf}) = 3.695 \times 10^{-16} + \frac{-1.251 \times 10^{-1}}{\nu} + \frac{1.052 \times 10^{13}}{\nu^2}$$

for $2.111 \times 10^{14} < \nu \leq 1.8259 \times 10^{14}$ where 1.8259×10^{14} is the ionisation-limit frequency, corresponding to the ionisation potential 0.754 eV for the negative hydrogen ion.

H^- free-free absorption coefficient $K(H^-_{ff})$ is given by

$$K(H^-_{ff}) = n(HI)n_e F_\nu(T) \quad \dots (4.4)$$

where $F_\nu(T)$ is given by

$$F_\nu(T) = \frac{1.3737 \times 10^{-25}}{\nu} + \frac{4.3748 \times 10^{-10}}{\nu^2} - \frac{2.5993 \times 10^{-7}}{\nu^2}$$

which is a fit to the dipole-length calculations by Stilley and Callaway (1970).

Neutral Hydrogen: Both the bound-free and free-free transitions contribute to continuous absorption. Bound-free absorption is more important than free-free absorption. Bound-free transition can occur from any level to continuum. The number density in each level can be calculated by Boltzmann equation

$$n_n = n(HI) \frac{g_n}{U(HI)} e^{-E_n/kT} \quad \dots (4.5)$$

where $g_n = 2n^2$ and $E_n = 13.595 \frac{Z^2}{1-(1/n^2)}$.

Bound-free absorption coefficient has the form

$$K(H_{bf}) = n_n \alpha_n [1 - e^{-h\nu/kT}] \quad \dots (4.6)$$

Polynomial approximations to α_n as given by Gingerich (1969) is as follows

$$\alpha_n = \frac{2.815 \times 10^{29} Z^2}{n^5 \nu^3} \left[A_n + B_n \frac{Z^2}{\nu} + C_n \frac{Z^4}{\nu^2} \right]$$

for $\nu \geq 3.28805 \times 10^{15} \times \frac{Z^2}{n^2}$.

The polynomial coefficients are as follows:

n	A_n	B_n	C_n
1	0.9916	2.719×10^{13}	-2.268×10^{30}
2	1.105	-2.375×10^{14}	4.077×10^{18}
3	1.101	-9.863×10^{13}	1.035×10^{28}
4	1.101	-5.765×10^{13}	4.593×10^{27}
5	1.102	-3.909×10^{13}	2.371×10^{27}
6	1.0986	-2.704×10^{13}	1.229×10^{27}
7	1	0	0

For levels above 9, the summation over levels is treated as an integral over n, and we obtain

$$\begin{aligned} K(H_{bf}) &= \frac{n(HI)}{U(HI)} \times \frac{2.815 \times 10^{29}}{3} (1 - e^{-h\nu/kT}) \frac{kT}{13.595} \\ &\times \left[e^{-13595(1 - \frac{1}{n^2})/kT} - e^{-13.595/kT} \right]. \end{aligned}$$

Hydrogen Molecule: Hydrogen molecules appear in large numbers in cool stars. H_2^+ is a significant absorber in the ultra-violet spectral region. H_2^+ absorption has been studied by

Bates (1951) and Matsushima (1964). Polynomial approximation to Bates' results for the sum of bound-free and free-free transitions is given by Kurucz (1970).

$$\kappa(H_2) = n(\text{HI}) n(\text{HII}) F_\nu(T) (1 - e^{-h\nu/kT}) \quad \dots (4.7)$$

where

$$\begin{aligned} F_\nu(T) = \exp & \left[-\frac{E_s}{kT} - 3.023 \times 10^3 + 3.7797 \times 10^2 \ln \nu \right. \\ & - 1.82496 \times 10^1 (\ln \nu)^2 + 3.9207 \times 10^{-1} (\ln \nu)^3 \\ & \left. - 3.1672 \times 10^{-3} (\ln \nu)^4 \right] \end{aligned}$$

with

$$\begin{aligned} E_s = & -7.342 \times 10^{-3} + -2.409 \times 10^{-15} \nu + 1.028 \times 10^{-30} \nu^2 \\ & - 4.230 \times 10^{-46} \nu^3 + 1.224 \times 10^{-61} \nu^4 - 1.351 \times 10^{-77} \nu^5 \end{aligned}$$

Rayleigh Scattering by HI and He I

HI Rayleigh Scattering: Using the cross-section given by Dalgarno (1962)

$$\kappa(\text{HI})_{\text{Ray}} = n(\text{HI}) \left(\frac{5.799 \times 10^{13}}{\lambda^4} + \frac{1.422 \times 10^{-6}}{\lambda^6} + \frac{2.784}{\lambda^8} \right)$$

$$\text{where } \lambda = \frac{2.997925 \times 10^{18}}{\min(\nu, 2.922 \times 10^{15})}$$

where $\min(A, B)$ means the smaller of A and B is adopted.

He I Rayleigh Scattering: The cross-section is given by Dalgarno (1962).

$$(\text{He I})_{\text{Ray}} = n(\text{He I}) \frac{5.484 \times 10^{-14}}{\lambda^4} \left[1 + \frac{2.44 \times 10^5}{\lambda^2} + \frac{5.94 \times 10^{-10}}{\lambda^2(\lambda^2 - 2.90 \times 10^{-5})} \right] \quad \dots (4.9)$$

where $\lambda = \frac{2.997925 \times 10^{18}}{\min(\nu, 5.15 \times 10^{15})}$.

Negative Helium ion: The bound-free absorption is generally found to be negligible for He^- because there is only one bound level with excitation potential of 19eV. For free-free absorption, Carbon, Gingerich and Latham (1969) gave a polynomial fit to the calculations of John (1968).

$$\kappa(\text{He}^-)_{\text{ff}} = n(\text{He I})n_e F_\nu(T) \quad \dots (4.10)$$

where $F_\nu(T) = aT + b + c/T$

with

$$a = 3.397 \times 10^{-46} - \frac{5.216 \times 10^{-31}}{\nu} + \frac{7.039 \times 10^{-15}}{\nu^2}$$

$$b = -4.116 \times 10^{-42} + \frac{1.067 \times 10^{-26}}{\nu} + \frac{8.135 \times 10^{-11}}{\nu^2}$$

$$c = 5.081 \times 10^{-37} - \frac{8.724 \times 10^{-23}}{\nu} - \frac{5.659 \times 10^{-8}}{\nu^2}.$$

When all the absorption coefficients are calculated, they are multiplied by N_{H} or N_{He} as appropriate and added to get total continuous absorption coefficient κ_λ .

Following Sneden (1974), we will denote the continuous absorption coefficient as κ_λ and line absorption coefficient by κ_ν for convenience. Numerical integration subroutine HELENA integrates κ_λ over the atmospheric levels in order to get the continuum optical depth τ_λ . In the calculation of a given line, we need continuum optical depths τ_λ at an arbitrary wavelength. By definition,

$$d\tau_\lambda = \kappa_\lambda \rho \, dl \quad \dots (4.11)$$

Where κ_λ is the continuum opacity at wavelength λ and ρ is the density of the material and dl the increment of depth in the atmosphere. We can also write $dl = \frac{d\tau_r}{\kappa_r \rho}$ where κ_r and τ_r are the continuum absorption coefficients and continuum optical depth at reference wavelength. Now,

$$\tau_\lambda = \int_0^{\tau_r} \frac{\kappa_\lambda(t_r)}{\kappa_r(t_r)} \, dt_r \quad \dots (4.12)$$

At first, the continuum absorption coefficient and optical depth is calculated at the reference wavelength and the value of τ_λ is calculated using equation (4.12).

Subroutine EQLIB solves the molecular equilibrium equation for all the relevant molecules at all the atmospheric depths, and calculates the free atomic density of all molecule-forming atoms. Input data to this subroutine contains the polynomial constants which are obtained by doing

least-squares fit to Tsuji's (1964) table of the logarithm of dissociation constants as a function of temperature. In our input data, we have the molecule identification number followed by four polynomial constants. The dissociation potential is calculated using the appropriate constants found with their identification number. Subroutine SUNDER examines each molecule and returns its component parts and subroutine DISCOV counts the number of times a particular atom appears in a molecule. Subroutine EQLIB solves simultaneously equations of the form

$$N_i = n_i + \sum_j n_{ij} N_{ij} \quad \dots (4.13)$$

and

$$N_i = n_i' + \sum_{ij} n_{ij} \cdot n_i n_j / K_{ij} \quad \dots (4.14)$$

Where N_i is the number density the element i would have had if there were no molecules, n_i is the actual number density of i ; K_{ij} is the dissociation constant of molecule ij and n_{ij} is the number of times atom i appears in molecule ij . For the solution of this set of equations, the Newton-Raphson method was employed. Briefly, given a set of equations $\tilde{f}(x)$ where $\tilde{x}_0 = (x_{1_0}, x_{2_0}, \dots, x_{m_0})$ are the initial guesses to the variable \tilde{x} and $\tilde{f} = (f_1, f_2, f_3, \dots, f_m)$, we solve the system of linear equations

$$A(\tilde{x}) \tilde{\delta} = \tilde{f}(\tilde{x})$$

for the increment $\tilde{\delta} = (\delta_1, \delta_2, \delta_3, \delta_4 \dots \delta_m)$.

Matrix A is given by

$$A_{ij}(\tilde{x}) = \frac{\partial f_i}{\partial x_j}(\tilde{x}),$$

i.e. matrix \tilde{A} is the matrix generated by differentiating each function f_i by each variable x_j and evaluating it at \tilde{x} . Then, $\tilde{\delta} = -\tilde{f}(\tilde{x}) \tilde{A}^{-1}(\tilde{x})$

and $\tilde{x}_{\text{new}} = \tilde{x}_{\text{old}} + \tilde{\delta}$.

The process is repeated till $\tilde{x}_{i,\text{new}} - \tilde{x}_{i,\text{old}} < \epsilon$, for all x_i . In our problem \tilde{x} are the number densities of different atoms or ions.

At this stage, the spectrum commands and line data are called for. We have to specify the starting and ending wavelength of the computations, the step size between two spectrum calculations and the limit on the either side of the step point for which the contribution due to neighbouring lines will be included in the spectrum calculations.

The line data consists of wavelength of the line (\AA), identification of an atom, given in the style of ATLAS (i.e. the integral part is the atomic number of the element and the number after decimal point shows the ionisation state. Thus FeI = 26.0, FeII = 26.1 etc.), atomic mass of the atom in a.m.u., χ_1, χ_2 , the first and second ionisation potential (eV) of the transition and the gf value i.e. the statistical

weight multiplied by the oscillator strength of the line i . In subroutine PARTFN the partition functions at each level of model atmosphere for various atoms are calculated using an expression

$$\begin{aligned} \log U = \text{Const } 1 + \text{Const } 2 \times T + \text{Const } 3 \times T^2 \\ + \text{Const } 4 \times T^3 \end{aligned} \quad \dots (4.15)$$

where the constants are those appropriate to that particular ion under consideration. These constants were derived from the least-squares fit of the temperature versus $\log U$, from the partition function data contained in the following sources: Drawin and Felenbok (1965) for H, He, Be, C, N, O, Na, Mg, Al, Si, Ca, Ti, Cr, Fe, Co, Ni, Zn, Sr, Zr and Ba; Bolton (1970) for Si, Mn and V; Kurucz (1970) for rare-earth elements. The temperature range of the fits are roughly from 2000 K to 20000 K and the fitting accuracy is always ≤ 1.5 per cent. These constants are stored in the subroutine as data with an identification number in ATLAS style followed by twelve coefficients, four for each ionisation state beginning with the neutral state.

Line absorption coefficient is calculated in subroutine NEARLY. We have the standard formula

$$K_{\nu} = N \frac{\pi e^2}{mc} \frac{f}{\Delta \nu_D} \left[1 - e^{-hc/\lambda kT} \right] U(a, \nu) \quad \dots (4.16)$$

In this equation, we have the physical constant $\pi e^2/mc$, the number density of the absorber N and oscillator strength of transition, f , the Doppler width $\Delta\nu_D$ in frequency units, the correction for induced emission $1 - e^{-h\nu/kT}$ and normalized Voigt-profile function $U(a, \nu)$. The Doppler width is given by

$$\Delta\nu_D = \frac{1}{\lambda} \left[\frac{2kT}{M} + \xi^2 \right]^{\frac{1}{2}} \quad \dots (4.17)$$

where ξ is microturbulent velocity and M is the mass of the absorber. Normalized Voigt function $U(a, \nu)$ can be expressed as

$$U(a, \nu) = \frac{a}{\pi^{3/2}} \int_{-\infty}^{\infty} \frac{e^{-y^2} dy}{(\nu - y)^2 + a^2} = \frac{1}{\sqrt{\pi}} H(a, \nu) \quad \dots (4.18)$$

where $H(a, \nu)$ is known as Hjerting's function. The approximation formula for $H(a, \nu)$ for various combinations of a and ν has been taken from Voigt (1965). The stated errors are less than one per cent. The variables are the damping parameters a and Doppler velocity ν . They are given by

$$a = \frac{\Gamma_n + \Gamma_s + \Gamma_w}{2\pi \lambda^{-1} \left[\frac{2kT}{M} + \xi^2 \right]^{\frac{1}{2}}} \quad \dots (4.19)$$

where Γ_n , Γ_s , Γ_w are natural, Stark, and Van der Waals broadening half-widths and Doppler velocity v is given by

$$v = \frac{\Delta\lambda}{\frac{\lambda}{c} \left[\frac{2kT}{M} + \xi^2 \right]^{\frac{1}{2}}} \quad \dots (4.20)$$

For
~~Since Van der Waals broadening is found to contribute in most situations only that was considered in the calculations.~~

The following formula from Unsöld (1955) for damping half width was used

$$\Gamma_w = 17.0 \times C_6^{0.4} \times v^{0.6} \times N(\text{HI}) \quad \dots (4.21)$$

Here, v is the mean relative velocity for an atom of mass M , given by

$$v = \left[\frac{8kT}{\pi} \left(\frac{1}{M} + \frac{1}{M_H} \right) \right]^{\frac{1}{2}} \quad \dots (4.22)$$

$$C_6 = 1.6 \times 10^{-33} \left[\left(\frac{13.5 Z_a}{\chi_i - E_{i,u}} \right)^2 - \left(\frac{13.5 Z_e}{\chi_i - E_{i,l}} \right)^2 \right] \quad \dots (4.23)$$

Z_e is the charge of the atom

$Z_e = 1$ for neutral atom, 2 for singly-ionised ion etc.

χ_i = the ionisation potential

$E_{i,l}$, $E_{i,u}$ = the excitation potentials of the lower and upper states for line i .

Calculation of all these parameters are done for each layer of the model atmosphere. For the calculation of number

density of absorber in the lower state of transition, Saha and Boltzmann's equations were used. Consider an atom i :

$$N_{i,\text{total}} = N_{i,I} + N_{i,II} + N_{i,III}$$

Now the Saha equation is

$$\frac{N_{i,j+1} n_e}{N_{i,j}} = \left(\frac{2\pi m_e kT}{h^2} \right)^{3/2} \frac{U_{i,j+1}}{U_{i,j}} e^{-\chi_{i,j}/kT} \quad \dots (4.24)$$

so that

$$\frac{N_{i,j+1}}{N_{i,j}} = \frac{4.830 \times 10^{15}}{n_e} \frac{U_{i,j+1}}{U_{i,j}} T^{3/2} e^{-1.16 \times 10^4 \chi_{i,j}/T} \quad \dots (4.25)$$

Then we may write

$$N_{i,\text{tot}} = N_{i,I} + N_{i,II} Q1 \quad \dots (4.26)$$

$$\text{where } Q1 = 1 + \frac{4.830 \times 10^5}{n_e} \frac{U_{i,III}}{U_{i,II}} T^{3/2} e^{-\frac{1.16 \times 10^4 \chi_{i,II}}{T}}$$

Then

$$N_{i,\text{tot}} = N_{i,I} \left(1 + \frac{N_{i,II}}{N_{i,I}} Q1 \right) = N_{i,I} Q2$$

where $Q2$ is the quantity in the brackett. Above equations are solved to yield $N_{i,I}$, the number of neutral atoms. Also

$$N_{i,\text{tot}} = N_{i,II} \left(\frac{N_{i,I}}{N_{i,II}} + Q1 \right)$$

so that

$$N_{i,II} = \frac{N_{i,tot}}{(Q1 + N_{i,I}/N_{i,II})} = \frac{N_{i,tot}}{(N_{i,I}/N_{i,II}) (1 + N_{i,II} Q1/N_{i,I})}$$

$$= \frac{N_{i,II}}{N_{i,I}} \frac{N_{i,tot}}{Q2} .$$

Finally, for a particular state of an atom we have from Boltzmann equation,

$$N_{i,j,r} = N_{i,j} \frac{g_{i,j,r}}{U_{i,j}} e^{-E_{i,j,r}/kT} . \quad .. (4.27)$$

Logarithmic abundances for all the elements from $Z = 1$ to $Z = 65$, scaled to hydrogen are also given as input data.

$$N_{i,j} = \text{ABUNDANCE} \times N_{H,tot} . \quad .. (4.28)$$

With these considerations the number of absorbers (XNUM) relevant for the particular line can be written as

$$XNUM = \frac{\text{ABUNDANCE} \times N_{H,tot}}{Q2 \times U(1)} e^{-\frac{1.1605 \times 10^4 E1}{T}} \quad .. (4.29)$$

for neutral atom,

$$\text{and } XNUM = \frac{\text{ABUNDANCE} \times N_{H,tot} \times \frac{N_{i,II}}{N_{i,I}}}{Q2 \times U(2)} e^{-\frac{1.1605 \times 10^4 E1}{T}} \quad .. (4.30)$$

for ionized atom. The absorption coefficient at line centre is given by

$$l_0 = \frac{\pi e^2}{mc} N_i \frac{gf}{\Delta\nu_D} (1 - e^{-hc/\lambda kT}). \quad \dots (4.31)$$

The line absorption coefficient at a distance $\Delta\lambda$ from the line centre is calculated by

$$l_\lambda = l_0 \times U(a, \nu). \quad \dots (4.32)$$

Line opacities and optical depths at wavelength, say λ , is calculated in subroutine TAUKAP. Contributions from all the lines falling in the wavelength range $\lambda - \Delta\lambda$ to $\lambda + \Delta\lambda$ are considered. The limit $\Delta\lambda$ is specified in the input line data. At each level, j line optical depth given by

$$k_\nu = \sum_j l_j(I) \times U(a_j(I), \nu) \quad \dots (4.33)$$

is calculated.

Now we are ready to calculate the emergent fluxes in the line and continuum. The emergent continuum flux as defined in Chapter 2 is given by

$$F_\lambda(0) = 2 \int_0^\infty S_\lambda(\tau_\lambda) E_2(\tau_\lambda) d\tau_\lambda.$$

The source functions in LTE calculations are merely Planck functions $B_\lambda(T)$. Planck function at a wavelength λ is calculated in subroutine SOURCE by Planck's radiation law

$$B_\nu(T) d\nu = \frac{2h\nu^3}{c^2} \frac{d\nu}{e^{h\nu/kT} - 1} \quad \dots (4.34)$$

With

$$\lambda = \frac{c}{\nu} \quad \text{and} \quad |d\nu| = \frac{c}{\lambda^2} d\lambda$$

we have

$$B_\lambda(T) d\lambda = \frac{2hc}{\lambda^5} \frac{c}{\lambda^2} \frac{d\lambda}{e^{hc/\lambda kT} - 1} \quad \dots (4.35)$$

If λ is expressed in \AA ,

$$\frac{2hc^2}{\lambda^5} = \frac{1.19089 \times 10^{35}}{\lambda^5}$$

and

$$\frac{hc}{\lambda kT} = \frac{1.43879 \times 10^8}{\lambda T}$$

Finally we get

$$B_\lambda(T) = \frac{1.19089 \times 10^{35}}{\lambda^5} \frac{1}{e^{1.43879/\lambda T} - 1} \quad \dots (4.36)$$

The exponential integrals are calculated in Function

Subroutine EXPINT. Formally,

$$E_n(x) = \int_1^\infty \frac{e^{-xt}}{t^n} dt = x^{n-1} \int_x^\infty \frac{e^{-t}}{t^n} dt \quad \dots (4.37)$$

Now

$$E_n'(x) = \frac{\partial}{\partial x} \int_1^{\infty} \frac{e^{-xt} dt}{t^n} = \int_1^{\infty} \frac{e^{-xt} dt}{t^n} = E_{n-1}(x).$$

We can derive a recurrence formula

$$E_n(x) = \frac{1}{n-1} [e^{-x} - x E_{n-1}(x)]. \quad \dots (4.38)$$

This allows one to get $E_n(x)$ from $E_1(x)$. $E_1(x)$ is calculated from the polynomial approximations of Abramowitz and Stegun (1965), where, for different ranges of x , $0 < x \leq 1$, $1 < x \leq 100$ and $x > 100$, different approximations are given. The errors are stated to be less than 2.0×10^{-7} . In our computations, first $E_1(x)$ is calculated by appropriate formula and then $E_n(x)$ is calculated using the recurrence relation (4.38). Since the spectrum range covered is small, we can use a single wavelength for the continuous opacity calculations. Central wavelength of the portion of the spectrum to be computed was adopted for a calculation of the continuum flux

$$F_{\lambda}(0) = \int_1^{N\tau_{\lambda}} \frac{\kappa_{\lambda}(I) \tau_{\lambda}(I) B_{\lambda}[T(I)] E_2(-\tau_{\lambda}(I))}{0.4343 \kappa_r(I)} dx_r(I). \quad \dots (4.39)$$

where $x_r = \log \tau_r$.

Now we are ready to compute the spectrum depths. For the starting wavelength, the calculations of line opacity and optical depths at this wavelength is done for all atmospheric levels. Contribution curve of depth as defined in Chapter 3

is calculated by

$$CD(I) = \frac{\tau_r(I) K_\lambda(I) B_\lambda[T(I)]}{0.4343 F_\lambda(0) K_r(I)} \left\{ E_2[-\tau_\lambda(I)] - \left[1 + \frac{K_v(I)}{K_\lambda(I)} \right] E_2[-\tau_\lambda(I) - \tau_v(I)] \right\}. \quad \dots (4.40)$$

Then the line depth is

$$D(N) = \int_1^{NTAU} CD(I) d X_r(I).$$

The depth calculations to next wavelength

$$WAVE = WAVE + STEP$$

are done in a similar way and the entire spectral region of interest is computed.

The computed spectrum is convolved to apparatus function in subroutine CONGAU. The instrumental profile as described in Chapter 2 can be expressed by a Gaussian profile. In this subroutine the input data is the full width at half maximum of the instrumental profile. The subroutine generates a Gaussian profile and convolves the computed spectrum with this profile. The convolved spectrum is finally compared with the observed spectrum. Subroutine PLOT plots the computed spectrum with the help of line printer. Hence it is not an accurate representation, but useful only for visual inspection.

4.2 Justification of simplifying assumptions

In the method of spectrum synthesis adopted in this work, following simplifying assumptions about the atmospheres of stars have been made:

1) Plane-parallel atmosphere: The extent of the atmosphere is much smaller than the radius of the star ($\frac{\Delta R}{R} < 0.1$), so that we can consider plane-parallel geometry instead of concentric spheres. Low-gravity stars (supergiants and giants) have extended atmospheres and validity of the assumption can be questioned. de Jager (1972), de Jager and Neven (1975), de Jager (1980) and Vardya (1982) have calculated the limiting value of gravity g_{\min} below which the plane-parallel approximation does not hold. For the temperature range of our interest 5000°K - 6000°K the g_{\min} calculated by Vardya (1982) is ~ 6 while none of our programme stars have $g < 10$. Thus the assumption of plane-parallel geometry is a reasonable one.

Further, in Figure (4.2), we show the contribution function for the equivalent width as a function of optical depth for two lines of FeI ($E_1 = 0.0$ eV, and 3.2 eV). We can see from the figure that the actual contribution to the line formation (or the depth of formation) comes from a narrow range in optical depth mainly between ($\log \tau = -0.3$ to $+0.8$). The contribution function $CD(\tau)$ was calculated

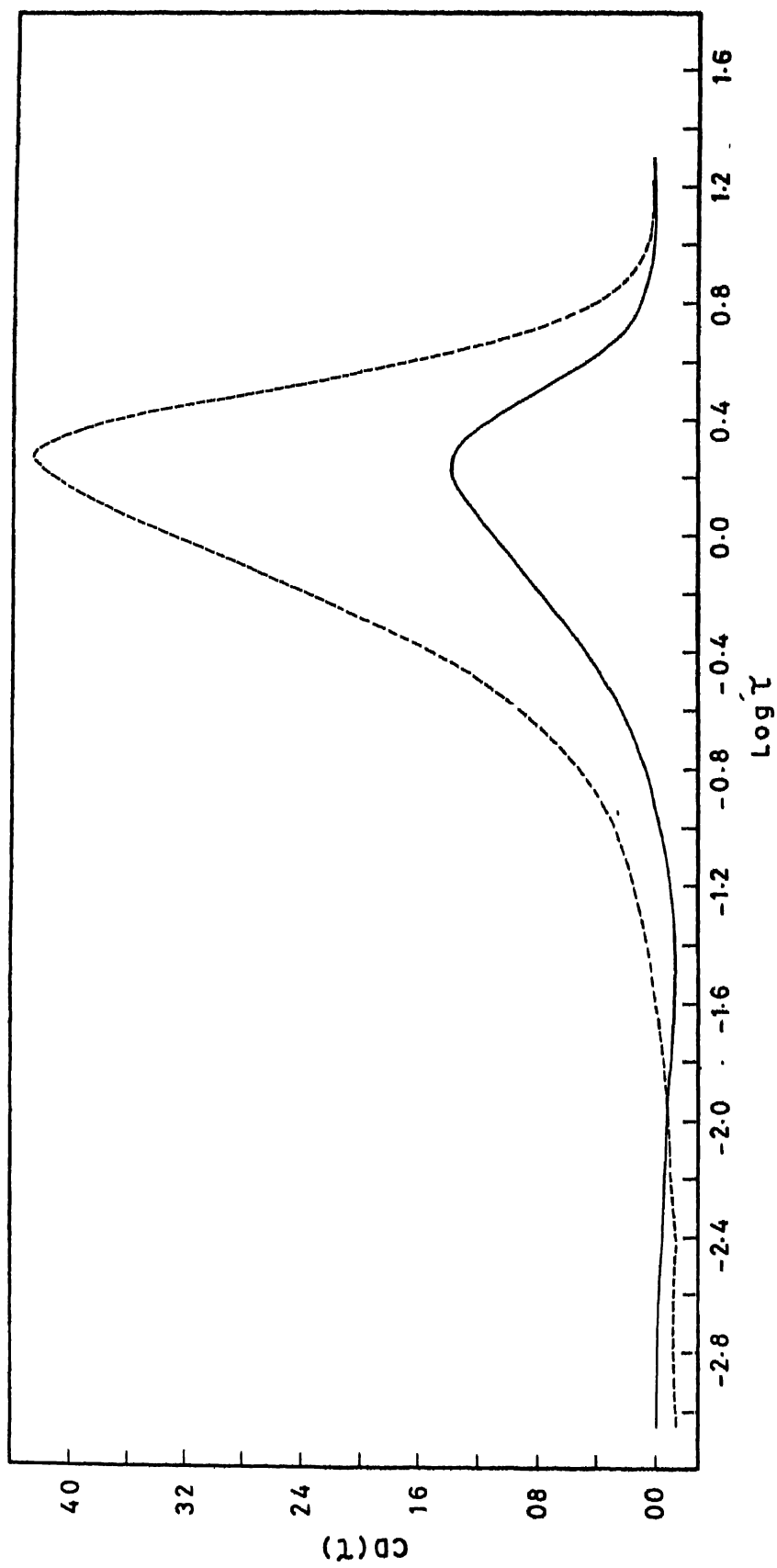


Figure 4.2 Contribution functions for Fe I 4375.944 ($E_1 = 0.0$ eV; broken line) and Fe I 4625.052 ($E_1 = 3.2$ eV; solid line).

using a model $T_{\text{eff}} = 5500\text{K}$, $\text{Log } g = 1.0$ from the grid of model atmospheres of Kurucz (1979). In these models, geometrical heights corresponding to different values of optical depths are also tabulated. Full width at half maximum of the contribution function in Figure (4.2) corresponds to 84860 km in geometrical height scale. If the radius of the star is $60 R_{\odot}$, which is typical of galactic Cepheids, the ratio of the line-forming region to radius of the star is ~ 0.0002 . Thus it is reiterated that the use of plane-parallel atmospheric layer will not introduce any serious error in our calculations.

2) The local thermodynamic equilibrium: The atmosphere of the star is assumed to be in local thermodynamic equilibrium (LTE); i.e. the relations such as Boltzmann's equation, Planck's formula and Kirchoff's law hold at a given point at the local temperature of the point. All the metallic lines are formed in the layers of optical depth $\tau = 0.1$ to 10. In these layers, the collisional processes are dominant as compared to the radiative processes. Therefore, for these photospheric or near-photospheric lines the LTE formulation is good enough.

3) The hydrostatic equilibrium: The atmosphere of the star is assumed to be in hydrostatic equilibrium; this implies that there is no large-scale acceleration comparable to the surface gravity; hence the pressure balances the gravitational

attraction. In the pulsating atmospheres of the Cepheids, the validity of such an assumption can always be questioned. For all the programme stars, the duration of the exposures were less than 1 per cent of the star's pulsation period. So, it is unlikely that there was any change in temperature and pressure of the star during the observation. Besides, Schmidt (1971) has pointed out that for Cepheids with period larger than 10 days, spectroscopically determined surface gravity values are in agreement with those derived from their masses. The masses indicated by evolutionary tracks of Hofmeister (1967) or Iben (1967) can be used together with the radii obtained by Wesselink's method. The gravity can be calculated from

$$g_{\text{eff}} = \frac{GM}{R^2} - \dot{R}$$

which holds if hydrostatic equilibrium is valid. (i.e. if R is a constant throughout the atmosphere). Schmidt (1971) compared spectroscopically derived gravities with those obtained from evolutionary masses. For Cepheids S Nor and η Aql ($P = 9.75$ d and 7.18 d, respectively), he found a disagreement between the two gravity determinations. For Cepheids of longer period (Y oph: $P = 17.12$ d), there was no significant difference between the two estimates of gravity. Rodgers and Bell (1968) have compared the density variations of several Cepheids. In the case of long-period Cepheid

1 Car, there is no apparent density variation larger than the errors in density estimations. The star 1 Car is a long-period Cepheid and has a small amplitude of light variations. It is possible that the atmosphere is always in hydrostatic equilibrium and a constancy of gravity and density is expected. However, long-period Cepheids SV Vul and K Pav have a sudden increase in the density near maximum light superimposed upon the gradual variations with a second maximum near minimum light. The sudden increase in density comes at the same phase in each case as a strong outward acceleration. Over the rest of the cycle, the variation in the density of the atmosphere is very slow. It appears from the above discussion that in long-period Cepheids of small amplitudes, the gravity does not vary much over the cycle and consequently the atmosphere is in quasi-hydrostatic equilibrium most of the time. In the case of long-period Cepheids with large amplitudes, it is possible that the gravity varies during the short interval of outward acceleration and stays nearly constant rest of the time. The atmospheres of short-period Cepheids do not appear to achieve hydrostatic equilibrium during a large part of their cycles and the relation between gravity and acceleration is not obvious for them. Keller and Mutschler (1970) calculated a hydrodynamic model of a 11.5 d Cepheid. They also calculated hydrostatic, constant-flux atmospheres with parameters

g_{eff} and T_{eff} taken from the hydrodynamic models at selected phases. The structure of these atmospheres compare well with the hydrodynamic models; the (B-V) colour predicted by the hydrostatic atmospheres and hydrodynamic models show favourable agreement. These considerations imply that for long-period Cepheids ($P > 10$ d), properly-chosen hydrostatic atmospheres can adequately predict the observable properties of Cepheids. Excepting X Sgr ($P = 7.01$ d) all our stars have periods > 10 d. The light curve of X Sgr is very smooth without any suggestion of humps. All the stars were observed in a phase range where the acceleration of the atmosphere is close to its minimum. We believe that for the phase at which the observations were made, the assumption of hydrostatic equilibrium is not unrealistic for X Sgr star also.

4.3 Determination of Atmospheric Parameters

Many model atmospheres are available in the literature and numerous programmes to calculate them. These models all depend on values of three parameters: the effective temperature (T_e), the surface gravity ($\log g$) and chemical composition. The abundance worker who is beginning a spectral synthesis is expected to have an approximate idea of what these parameters are for the type of stars considered. A gridwork of models is selected which is distributed over the range of uncertainties in the initial estimates of T_e , $\log g$

and abundance. Calculations are made for all these models and final results are taken from the particular model which gives the best fit of the theory with observations.

The ideal spectroscopic information for a reasonable estimate of the atmospheric parameters is the measurement of relative energy distribution in the continuous spectrum. What is available generally is not the energy distribution curve but the stellar colours which are essentially the energy distribution observed with broad band-pass filters. By a comparison of the magnitudes measured in different parts of the spectrum, a measurement is made of the shape of the stellar energy distribution. The difference between the magnitudes in two bands, defined as the colour between the two effective wavelengths, gives a first-degree shape, or the slope of the energy distribution.

4.3.1 Estimation of Approximate Atmospheric Parameters from Colours

It is necessary to correct the observed colours for the interstellar reddening, before using them to derive atmospheric parameters. Any uncertainty in the intrinsic colour will affect the atmospheric parameters derived using them. An error of 0.1 mag in $E(B-V)$ corresponds to about 300K in the temperature scale.

Existing photometry of Cepheids, though extensive, is very inhomogeneous and mostly has been made using broad-band photometric systems. These systems are not very well suited for accurate reddening determinations. Stars with different spectral energy distributions obscured by the same amount of interstellar dust will show different colour excesses in such broad bands. One can, in principle, correct for broad-band non-linearities, but the correction terms are not sufficiently well defined and - in the case of Cepheids - not only vary from one star to another but also depend on the phase of light variations.

Pel (1976) has published Walraven five-colour photometry for 150 Cepheids in the southern Milky Way. The quantity and quality of this data is outstanding and must represent the most extensive uniform, high accuracy body of data ever obtained on Cepheids. The properties and stability of the VBLUW system, and the calibration of VBLUW colours in terms of physical parameters by means of theoretical spectra, have been discussed by Lub and Pel (1977). It was demonstrated by these authors that the effect of reddening on VBLUW is highly linear because the VBLUW bands are sufficiently narrow. In particular, the slopes of the reddening lines are independent of the observed energy distribution which implies that the same correction term can be used for all the phases of a Cepheid. This greatly simplifies the reddening correction as

compared to broad-band systems where complicated differential corrections are needed.

Pel (1978) has derived temperatures, gravities, bolometric light curves, radius variations and equilibrium values of these quantities for 98 Cepheids with $P > 11$ d, using the model atmosphere spectra from Kurucz (1975) and the intrinsic colours of these Cepheids. The method adopted by Pel (1978) to derive the colour excesses is to shift the observed points in the two-colour diagram along the reddening lines (corresponding to the known interstellar extinction law) onto their intrinsic unreddened positions. Additional information is thus needed to define the intrinsic position. Pel has made independent determination of the required intrinsic Cepheid locus. The two-colour diagram most suitable for this purpose is (V-B) - (B-L) diagram. Cepheids, during their cycles, describe long narrow loops in the (V-B) - (B-L) plane. Apart from the irregularities that are associated with the secondary bumps of the light curves and the differences in amplitudes for the stars of different periods, the loops of most Cepheids look very similar in shape and orientation. Observations of stars of different luminosity classes reveal that for spectral types later than F0 there is practically no luminosity effect in the (V-B) - (B-L) diagrams. Theoretical colours derived by using Kurucz model atmosphere fluxes (Lub and Pel 1977)

confirm this by demonstrating that all constant-gravity lines for $T_e < 7500^\circ\text{K}$ nearly coincide. These reasonings indicate that all unreddened Cepheids occupy a well-defined locus in (V-B) - (B-L) diagram and that the observed loops must have been shifted away from this locus by different amount of reddening. By shifting the loops back onto the locus one can determine the colour excesses. To fix the unreddened position of this locus Pel (1978) used (1) the reddening of the brightest and least-reddened Cepheid β Dor, (2) the reddening of the least-reddened cluster Cepheid S Nor, (3) positions of the brightest Ib and Iab supergiants in (V-B) - (B-L) diagram, and (4) the theoretical (V-B) and (B-L).

The (V-B) - (B-U) diagram is best suited for a derivation of physical parameters due to its sensitivity to temperature as well as gravity and because it separates the two parameters well. Pel constructed a theoretical (V-B) - (B-U) diagram using Kurucz models. Following analytical expressions were fitted to the grid of theoretical colours and bolometric corrections:

$$\theta_e = 0.812 + 1.008 (V-B)^* + 8.5 \left\{ (V-B)^* - 0.012 \right\}^3$$

$$\text{with } (V-B)^* = 0.337 \frac{(V-B) - 0.216}{(B-U) - 0.157};$$

$$\text{Log } g = 1.340 - 16.1 (B-U)^* - 7.0 \left\{ (B-U)^* \right\}^2$$

$$\text{with } (B-U)^* = (B-U) - 0.504 - 1.2 \times \left\{ |\theta_e - 0.852| \right\}^{1.61} + 0.015 (\theta_e - 0.852);$$

and

$$\text{B.C.} = 0.834 (|\theta_e - 0.695|)^{3/2} + 0.035 (\log g)$$

$$- \theta_e (0.027 \log g - 0.053) - 0.156.$$

$$\theta_e = \frac{5040}{T_e}$$

In the region covered by the Cepheid loops, these relations fit the exact values of the discrete grid points to within 0.0015 in θ_e and 0.05 in $\log g$.

Pel has computed this grid using the model atmospheres due to Kurucz ($T_e = 5500 - 7000\text{K}$ and $\log g = 0.5 - 3$) and extrapolated the analytical relations down to $T_e = 5000\text{K}$ to cover the complete loops of Cepheids with $P < 11$ d. Though a majority of our programme stars have periods longer than this value, the phases on the descending branch of the light curve at which the observations were made have $T \gg 5400\text{K}$ and hence do not generally involve extrapolation. The initial estimates of T_e and $\log g$ were hence obtained using the analytical expressions quoted above.

4.3.2 Improvement of the Atmospheric Parameters using Spectrum Synthesis

The photometrically-derived atmospheric parameters provide a first guess to the star's atmosphere. This guess is improved ^{by computing} a large number of lines (for an element say Fe) covering a large range in equivalent widths, excitation

potentials and atleast two ionisation stages, for slightly differing atmospheric parameters until the computed spectrum agrees with the observed one consistently for all the lines. Different atmospheric parameters affect the strength of the lines in different ways; this fact helps us in improving each atmospheric parameter independent of the others. The parameters were improved in the following order:

(1) Microturbulence: The motions of photospheric gas elements is broadly called turbulence. If the element of moving gas is large compared to the mean free path of a light quantum the turbulent motion is called macroturbulence. Macroturbulence does not affect the equivalent widths of the lines but the line profiles are broadened. When the individual elements of the moving gas are small compared to the mean free path of a light quantum we will have microturbulence. Here, the elements of gas moving with different velocities absorb at different distances from the centre of the line. Absorption can occur over a greater range in wavelength because of the Doppler shifts introduced by the turbulence. If the line is not weak and saturation effects are present at the core of the line, broadening introduced by the microturbulence reduces the amount of saturation allowing the equivalent width of the line to increase. The effect of microturbulence on the curve-of-growth is to raise the flat portion above the one

produced by thermal motions alone. The microturbulence is taken as a free parameter in abundance analysis by the curve-of-growth technique and is determined from the shift required along the y-axis for the theoretical and observed curves of growth to agree. In our approach, we computed the equivalent widths for a large number of FeI lines covering a good range in equivalent widths, using the models with T_e and $\text{Log } g$ determined photometrically and for a range of trial values of microturbulence velocity. Since it is known from the previous studies (e.g. Schmidt 1971; Schmidt, Rosendhal and Jewsbury 1974; Luck and Lambert 1981) that the abundance of iron peak elements in Cepheids is not very much different from the solar value, we have assumed the solar iron abundance as a starting value. The microturbulence velocity for which the lines of different intensities agree with the observed ones was finally adopted.

(2) Effective temperature: The temperature controls the line strengths very strongly. The temperature sensitivity can be seen through the exponential and power dependences with T_e in the excitation and ionisation equations. As the temperature is varied, most lines go through a maximum in strength. Usually the increase in strength with temperature is due to an increase in excitation. The decrease beyond the maximum results in some cases from the increase in continuous opacity of the negative hydrogen ion which in turn arises from an

increase in electron pressure. In some other cases, the decrease results from the ionisation of the absorbing species. Normally the temperature derived from continuum colours is not very accurate. In order to improve the estimate, lines of a particular element, say iron, covering a large range in excitation potential are computed. Abundances derived from individual lines are examined to see if they show a correlation with the excitation potential; such a correlation is expected if the atmospheric temperature is incorrectly chosen. The elimination of such a correlation with excitation potential would lead to an improved choice of T_e .

(3) Surface Gravity: Changes in the pressure can change the ratio of line absorption to the continuum opacity. The pressure is related to the surface gravity through equations $P_g = C_1 \times g^{1/3}$ and $P_e = C_2 \times g^{1/3}$. Therefore, the pressure dependence can be translated into a gravity dependence. Lines formed by any ion or atom where most of the element is in the neighbouring ionisation stage are insensitive to changes in pressure (and hence in gravity); but lines corresponding to the dominant ionization stage are pressure sensitive. For example, in the case of the solar-type stars, most of the iron is singly ionized and, therefore, Fe II lines are more sensitive to pressure compared to Fe I lines. Once the temperature is accurately determined, the value of gravity can be

determined by requiring that the lines of neutral and ionised iron lead to the same value of abundance.

4.4. Assembling the line data

Among the line parameters required in our investigations the wavelengths were taken from Moore, Minnaert and Houtgast (1966) and the excitation potentials from the Revised Multiplet Table (Moore 1945). Accurate gf values for all the lines of interest are very difficult to get. Though a number of investigations exist (particularly for elements like iron, chromium etc.) there are large differences in gf values determined for the same line in different investigations and for some weak lines gf values have not been calculated at all. The most accurate gf values determined so far is by Blackwell and Shallis (Oxford group) who claim an accuracy of 0.5% in their gf values. These investigators have experimentally determined the gf values for a large number of Fe and Ti lines. Such high-precision gf values are not available for other elements; even for Fe and Ti there are very few lines in the spectral region of our interest for which high-accuracy gf values are known. Considering these problems, we have employed here, solar gf values obtained from an inverted solar analysis. Solar abundances were taken from the new table of Pagel (1977) and the solar photospheric model of Holweger and Müller (1974) was adopted with a depth independent microturbulent velocity of 1.0 km s^{-1} . The trial gf values were taken from the

compilation of Kurucz and Peytremann (1975); they have determined semi-empirical gf values of iron lines and also compiled the gf values of other elements from the literature.

We have given the equivalent widths of Moore, Minnaert and Houtgast (1966) as input to a single-line version of the spectrum synthesis programme. In this programme, gf values are altered by small amounts till the computed equivalent widths agree with the observed ones.

The use of these solar oscillator strengths makes this study essentially a differential one with respect to Sun. The use of model-atmospheric technique removes the difficulties encountered otherwise in comparing with a standard of dissimilar spectral type and luminosity. The observed solar spectrum from the Atlas of Solar Spectrum by Minnaert, Mulders and Houtgast (1940) is compared with the theoretically computed spectrum in Figure (4.3). One can see from the figure that the agreement is very good.

The s -process elements are usually represented by very few, weak and often blended lines. Very few abundance determinations of these elements are available in the literature and some of these determinations are based on a single line; accuracy of such investigations is always very low. Keeping these factors in mind, a number of small portions of the spectrum (each portion covering 5\AA to 15\AA

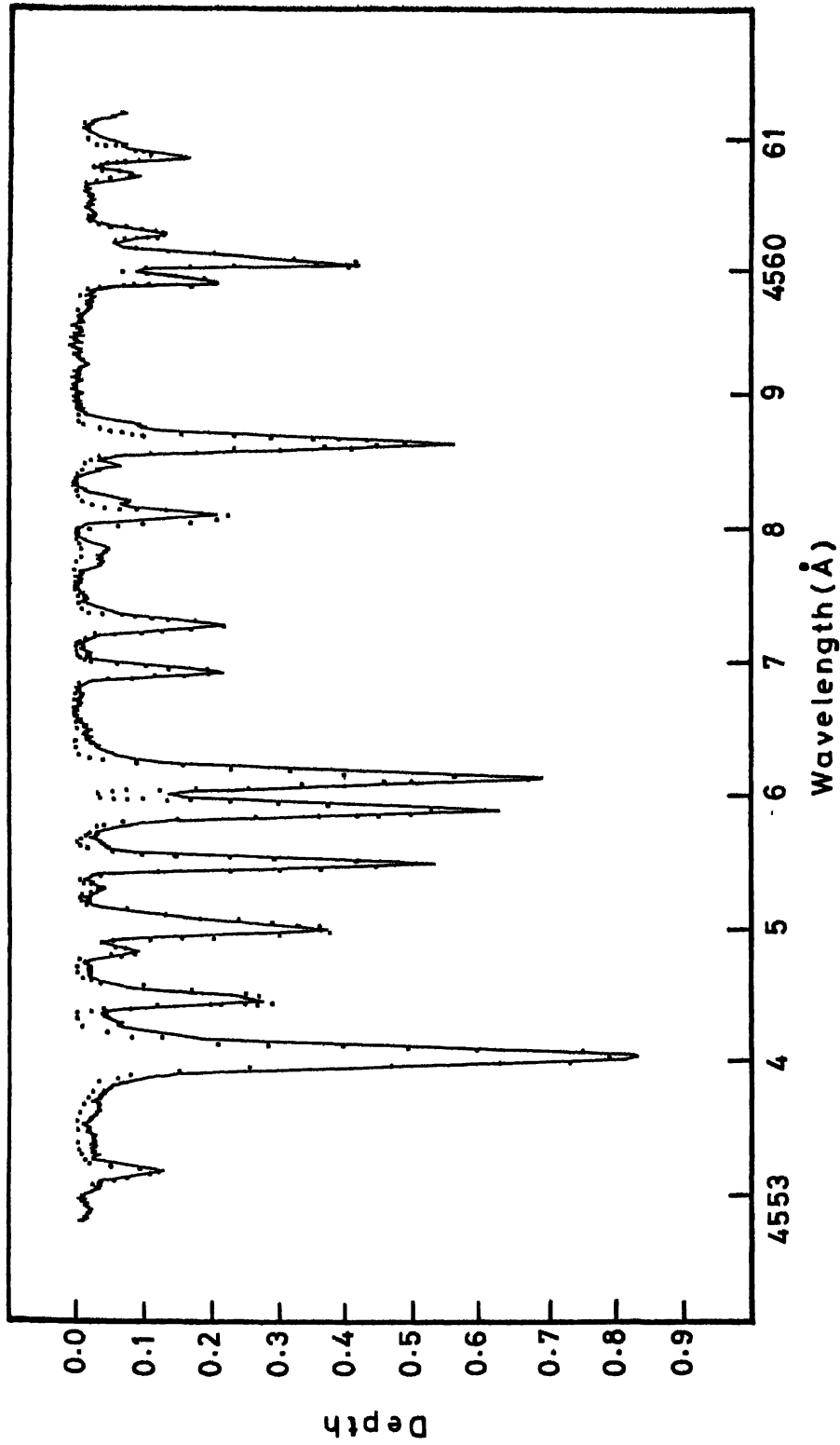


Figure 4.3 Comparison of the theoretically computed spectrum (dots) based on the solar model atmosphere of Holweger and Muller (1974), with the observed solar spectrum (continuous line) of Minnaert, Mulders and Houtgast (1940).

region) were selected having as many lines of Ba, La, Ce, Sm and other s-process elements as possible. In Appendix, we give the list of the constituent lines for the various spectral regions computed. The first column gives the wavelength of the line adopted from Moore, Minnaert and Houtgast (1966). The second column gives the atomic identification of the element together with the ionisation state of the element in the style of ATLAS (Kurucz 1970). The integral part of this number is the atomic number, and the first decimal the ionization state. The third column gives the atomic mass in amu. Fourth and fifth columns give the first and second ionisation potentials of the atom respectively. Sixth and seventh columns give the excitation potentials of the lower and upper level respectively. The eighth column gives the adopted gf values.

The spectral region $4550\text{\AA}-4564\text{\AA}$ proved to be extremely important in our investigations. Ba II 4554.036 is an asset for the investigations because, for the spectral types of Cepheids, this line is relatively unblended. Shortward of this line, the first conspicuous line is Ti II 4552.29 which is not likely to affect the equivalent width and the central depth of the Ba II line. In the longer wavelength side, Cr II 4552.02 line (multiplet 44) is present. Intensity of this line is ^{not} more than 50% of the Ba II line. Fortunately, there are two more Cr II lines arising from the same multiplet

in the same wavelength region (Cr II 4558.050 and Cr II 4586.204). These lines can be used to predict the behaviour of Cr II 4555.02. Once a suitable value of chromium abundance is determined using other lines, the spectral region around 4554Å can be computed with different barium abundances till a satisfactory agreement is reached. Ba II 4550.036 line has the advantage that very accurate gf values are determined by Holweger and Müller (1974).

Some investigators do not recommend the use of 4554.036 line because of its strength. This line does not fall on the linear portion of curve of growth but on flat portion where the lines are supposed to be more sensitive to microturbulence. However, accurate value of microturbulence can be determined from the lines of elements like Fe, Cr and Ti, prior to the barium abundance determination, and hence the accuracy of the abundance estimates can be improved. Instead of being disadvantage, the strength of the line becomes an asset in low-dispersion spectra where weak lines are almost lost due to the crowding of lines.

In 4550.0Å to 4564.0Å spectral region ^{there} ~~three~~ are also important lines of Ce II at 4560.280Å, 4560.966Å and 4562.367Å (resonance line). The line at 4562.367Å is almost unblended. Its equivalent width is $\sim 80\text{mÅ}$, i.e. this line is on the linear portion of the curve of growth and hence is very sensitive to

abundance. The contaminating lines which might interfere with these three lines of Ce II are the following: (1) Fe I 4560.097 line which is rather weak for low-gravity atmospheres ($\log g = 1.0 - 2.0$) like Cepheids and hence not likely to affect Ce II 4560.280 line very seriously. At solar gravities ($\log g = 4.4$) the Fe I line becomes as strong as Ce II line. (2) Another contaminating line which comes in between these Ce II lines is Fe I 4561.417 which is even weaker than Fe I 4560.097. It continues to be weak for all gravity values. Solar equivalent width for this line is $1.3\text{m}\text{\AA}$ and even in the Photometric Atlas of Spectral Lines of Procyon (F5Ib) and α Boo it is not conspicuous. The atomic parameters of all these lines are included in the spectrum synthesis calculations reported here. Since there is a large number of unblended Fe I and Fe II lines in the spectra, the abundance of Fe is determined very accurately from them and the effect of these lines could be eliminated.

The resonance line Ce II 4562.367 is quite isolated and - at the dispersion of 11.3\AA mm^{-1} - is one of the most suitable lines for abundance determination of Ce.

At the dispersion of 22.6\AA mm^{-1} , which we have employed for the fainter stars, Ce II 4560.280 and 4560.966 have merged together, but this mixed feature can still be used for deriving the abundance of Ce. Cowley (1970) has suggested

the use of curve of growth for a blend itself. Blends are much easier to deal within the method of spectrum synthesis.

At the dispersion of 22.6\AA mm^{-1} , Ce II 4562.367 makes its presence felt as a hump in the wing of Ti II 4563.766 and if the abundance of Ti is fixed using other lines of Ti, the hump at 4562.367 still provides the information on the Ce abundance.

The utility of other lines of Ce II (e.g. 4486.917 and 4628.160) is limited to high dispersion spectra.

For Sm the important lines are due to Sm II 4329.038, 4334.166, 4362.038, 4420.526, 4577.694 and 4616.720. All these lines can be used at higher dispersions, but at lower dispersions Sm II 4334.166 and 4362.038 are the only ones that can be used. The former line is blended with La II 4333.764, but the contribution of these two lines to the blend can be separated out. The line 4362.038 is very useful even at 22.6\AA mm^{-1} dispersion. It has no strong neighbouring line to affect it. Ce II 4361.668 at its shorter wavelength side is extremely weak and Cr II 4362.93 at the longer wavelength side is also very insignificant.

CHAPTER 5

ABUNDANCE ANALYSIS OF INDIVIDUAL CEPHEIDS

5.1 Introduction

Detailed spectroscopic investigations of several bright Cepheids have been made during the last two decades by a number of workers covering the entire cycle of pulsations of individual Cepheids. Atmospheric parameters (temperature, gravity, electron pressure and elemental abundances) of RT Aur at different phases of its pulsation cycle were determined by Bappu and Raghavan (1969) using the differential curve-of-growth method. They have also derived the radial velocity curve of the star, and its radius using the Wesselink method. Van Paradijs (1971) determined metal abundances of δ Cep at nine phases using the curve-of-growth method. Curve-of-growth analysis of η Aql was made by Schwarzschild^{Schwarzschild} and Adams (1948). Coarse and fine analysis of κ Pav, β Dor and ι Car were made by Rodgers and Bell (1963, 1964a,b, 1968), and Bell and Rodgers (1967). Iron abundance of southern Cepheids S Nor, Y Oph, U Sgr and η Aql were determined by Schmidt (1971) using the curve-of-growth and model-atmosphere techniques. The atmospheres of RT Aur, T Mon and X Cyg were analysed by Schmidt, Rosendhal and Jewsbury (1974) using similar techniques with the intention of comparing the abundances of these Cepheids with the non-variable supergiants

that occupy the same region in the HR diagram as the Cepheids.

Three of our programme stars have been studied by Luck and Lambert (1981) using the spectrum-synthesis method. Luck has determined the abundances of C, N, O, and a few heavier elements using high-resolution reticon spectra in the red and near-infrared spectral region. The resolution of these spectra obtained using coude reticon spectrometer is 0.2\AA which is better than the resolution of 0.4\AA of the present investigations. Also, the red region of the spectrum is much less crowded compared to the spectral region covered here which made their analysis easier. However, the blue region has many more important lines of heavy elements as compared to the red region. In spite of the somewhat lower resolution of our spectrograms and entirely different spectral region of study, it is very satisfying to note the close agreement between the abundances derived by us and Luck and Lambert. This success of the method of spectrum synthesis in dealing with the problems related to blending of lines has lent support to our application of this method at still lower resolutions.

For a demonstration of our abundance analysis, we will describe the analysis of T Mon in greater detail. This star was observed not only at the dispersion of 11.3\AA mm^{-1} at which X Sgr and ζ Gem were observed, but also at the

dispersion of 22.6 \AA mm^{-1} at which distant and hence fainter Cepheids SV Mon and WZ Sgr were observed. Since the same spectral region was used for all the stars, we will show the calculated and observed line intensities of the test lines only for T Mon and for the rest of the stars we will demonstrate the agreement with the help of figures. The stars ζ Gem, T Mon and X Sgr were also studied by Luck and Lambert (1981) whose main interest was in the CNO abundances. However, they have also determined the abundances of heavier elements and we will compare the abundances of the common elements later in the chapter.

The solar abundances used in the present investigations are taken from the solar abundance table of Pagel (1977). Model atmospheres in the temperature range of 4000K to 5500K are from the grid of Gustafsson et al (1975) while those in the range of 5500K to 6500K are from Kurucz (1979).

5.2 T Monocerotis - A Detailed Example

T Monocerotis is a bright Cepheid ($m_v = 6.0$) with a pulsation period of 27.0205 d. Due to its brightness, it was included in a number of photometric investigations; important among them is the work of Wisniewski and Johnson (1968) who determined UBVRIJKL light curves for twenty classical Cepheids. The light curve of T Mon is highly asymmetric but the variations in light are smooth with no

suggestion of abrupt humps.

The light-curve parameters (mainly period and epoch of maximum light) used in our study are from Schaltenbrand and Tammann (1971). These authors combined numerous photometric observations of a large number of galactic Cepheids, after reduction to UBV system where the observations were made in different systems. The light-curve parameters were determined by Fourier analysis of these observations.

Radial velocity curves for T Mon have been derived by Sanford (1956) and Wallerstein (1972). Evans (1976a) determined simultaneous light and radial velocity curves for T Mon among other Cepheids, because the phase matching of light and radial velocity curves is crucial in Wesselink's method of radius determinations. Using these observations, Wesselink radii for several Cepheids were determined by Evans (1976b). The value of the radius of T Mon determined by Evans is $144 R_{\odot}$.

Photometric Estimates of Atmospheric Parameters: Photometric colours of stars should be first corrected for interstellar extinction before using them to derive atmospheric parameters. The colour excess $E(B-V)$ of T Mon has been calculated by a number of investigators (Kraft 1961; Sandage and Tammann 1968; Parsons 1971; Schmidt 1972b; Fernie 1970; van den Bergh 1977). As pointed out by Patterson and Neff (1979), the

values of colour excess determined by various observers ranges from $E(B-V) = 0.18$ to 0.58 ! The temperature of a star at any phase is often determined using the relation between $(B-V)$ and effective temperature, as proposed by Kraft (1961) and supported by Parsons (1971):

$$\text{Log } T_{\text{eff}} = 3.886 - 0.175(B-V)_0.$$

In such a case, the difference in the effective temperatures derived using the two extreme values of colour excess of T Mon could be as much as 750K.

Another factor which could affect the photometrically determined temperature is the presence of companions. As the companion of a Cepheid is normally bluer than the Cepheid itself, the accuracy of the intrinsic $B-V$ colour is affected and so is the temperatures derived from them. A companion has been predicted for T Mon photometrically by Pel (1978) from the peculiarities in the intrinsic Cepheid locus for the star; hence Pel regarded the calculated values of $E(B-V)$ with suspicion. The presence of a blue companion for T Mon has been confirmed by Mariska, Doschek and Feldman (1980) from the ultraviolet spectra of this star observed with the International Ultraviolet Explorer. It is clear that the temperatures of T Mon derived using blue colours or colour indices are likely to be inaccurate.

Parsons (1971) has derived the temperature, surface gravity and colour excess for a large number of Cepheids (including T Mon) and yellow supergiants by comparing UVBGR colours for these stars with the theoretical fluxes he had earlier computed from model atmospheres (Parsons 1969). Schmidt (1972b) has determined effective temperatures for a large number of Cepheids from continuum photometry. The slope of Paschen continuum was measured for these stars, and temperatures and line-blocking coefficients were determined through a comparison with the model-atmospheric energy distribution. The use of H-alpha profile to determine the temperature of the stars is also suggested by Schmidt (1972a). Pel (1978) determined atmospheric parameters of a large number of southern Cepheids using VBLUW photometric data and the model-atmospheric fluxes of Kurucz (1975).

In our investigations, we have assumed the atmospheric parameters derived by Pel (1978) as a starting value. For the phase 0.219 of our spectrogram (δ 1161), the parameters derived by Pel for T Mon are $T_e = 5100\text{K}$, $\log g = 0.8$. These estimates were improved spectroscopically by an analysis of a large number of Fe I and Fe II lines. Table 5.1 gives the list of test lines of Fe I and Fe II which were computed for a grid of models in the temperature range of 4500K to 6500K, $\log g$ ranging between 0.5 and 2.5, and the microturbulent velocities ranging between 3 and 7 km s^{-1} . Since the iron

Table 5.1

List of the iron lines computed over a grid of model
atmosphere to determine atmospheric parameters

λ	E_1	E_2
<u>Fe I lines</u>		
4427.312	0.05	2.84
4602.944	1.40	4.16
4602.008	1.60	4.28
4632.918	1.61	4.26
4352.748	2.21	5.05
4630.128	2.27	4.93
4401.451	2.83	5.59
4358.512	2.94	5.77
4517.530	3.06	5.79
4625.052	3.23	5.90
4587.137	3.57	6.25
4584.824	3.60	6.28
4484.240	3.60	6.35
4611.285	3.64	6.31
4485.683	3.69	6.40
<u>Fe II lines</u>		
4413.699	2.68	5.46
4416.817	2.77	5.56
4583.840	2.79	5.52
4515.327	2.82	5.52
4582.833	2.83	5.52
4576.327	2.83	5.52
4472.930	2.83	5.59
4508.283	2.84	5.59
4620.513	2.82	5.49

abundance of classical Cepheids are known to be not very different from the solar value, the solar iron abundance was assumed in computing these lines. At first, the micro-turbulence velocity was determined by examining Fe I lines of various strengths. The final value of the microturbulence was selected as the one at which there was no trend in $W_{\text{obs}} - W_{\text{comp}}$ depending on the strength of the line. The temperature was then determined by requiring no trend in $W_{\text{obs}} - W_{\text{comp}}$ with excitation potential of the line. At each of the appropriate model grid points the slope of the relation between the excitation potential and $W_{\text{obs}} - W_{\text{comp}}$ was derived and the proper effective temperature was then obtained by determining the temperature at which the slope would be zero. The gravity was determined by requiring Fe I and Fe II lines to lead to the same value of the abundance. The final atmospheric parameters derived for T Mon at a phase of 0.219 are: $T_e = 5500\text{K}$, $\log g = 1.25$ and $v_t = 5.0 \text{ km s}^{-1}$.

The atmospheric parameters of T Mon estimated by different workers at different phases of the star are compared in Figure (5.1). Our estimates of the atmospheric parameters are also plotted in the same figure. The temperatures derived by Schmidt (1972b) are seen to be systematically hotter by about 700K, while the temperatures derived by Pel (1978) are cooler by 250K. Our temperatures are in fair agreement with the spectroscopic temperatures derived by Luck and Lambert

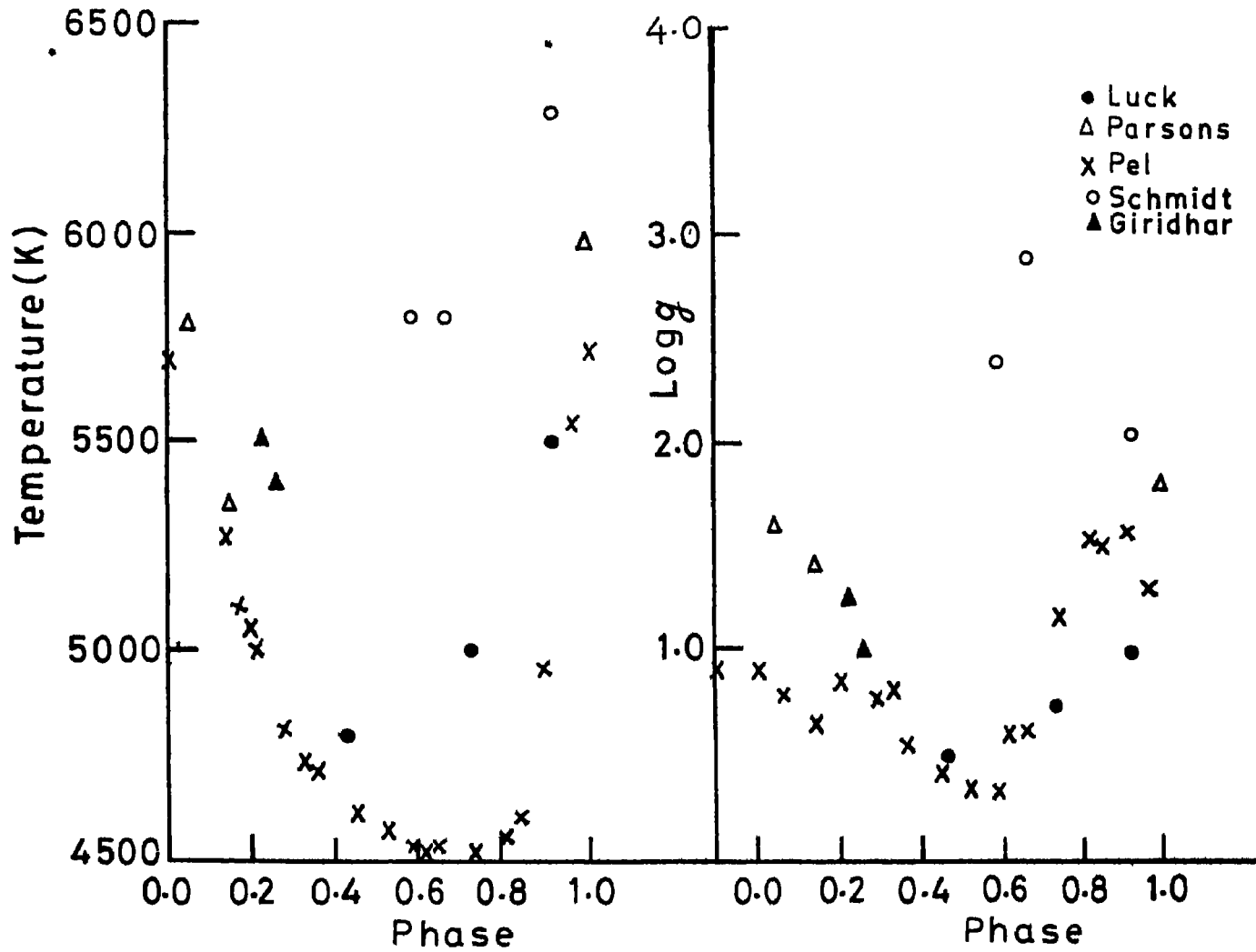


Figure 5.1 Atmospheric parameters of T Mon as a function of phase of the light curve, estimated by different investigators.

(1981) and temperatures derived by Parsons (1971) from the matching of observed UVBGR1 colours to the model atmosphere fluxes. Also the gravities derived by Pel and Parsons are in close agreement with the gravities derived in the present investigation ($\Delta \log g = \pm 0.5$) but the gravities determined by Schmidt, Rosendhal and Jewsbury (1974) are higher by $\Delta \log g = 1.6$. The probable reason for this is that the temperature determined by Schmidt (1972b) are too high and in order to maintain the ionisation balance Schmidt, Rosendhal and Jewsbury were forced to adopt higher gravities.

Derived Abundances: Having determined the atmospheric parameters, selected regions of the star's spectrum were computed for a range in chemical abundances which differed from the solar value by -0.3 to $+0.3$ dex in steps of 0.05 dex. Abundances of all the elements were varied by the same factor. The best-fit abundances were thus determined. In Table 5.2 we show the agreement between the observed and computed equivalent widths of Fe lines for the spectrogram $\delta 1161$. The observed equivalent widths are either measured directly or derived from the residual intensities at the line centre as described in Chapter 3. The test lines are computed for a model with the parameters $T_e = 5500\text{K}$, $\log g = 1.25$, $v_t = 5.0 \text{ km s}^{-1}$ and $\text{Fe} = 7.53$. Here and in what follows, the abundance A of an element A is the logarithmic abundance relative to $\text{H} = 12.0$.

Table 5.2

Comparison of observed and computed Fe lines for S1161 of T Mon

Wavelength	E1	E2	Observed W_λ mÅ	Observed central depth W_λ	Computed W_λ mÅ	Computed central depth	(O-C)% W_λ	(O-C) % central depth
<u>Fe I lines:</u>								
4602.944	1.40	4.16	308.7	0.382	300.0	0.377	+ 2.6	+ 1.3
4602.005	1.60	4.28	175.6	0.245	188.5	0.255	- 7.4	- 4.1
4632.918	1.61	4.26	240.0	0.340	245.0	0.310	- 2.0	+ 8.8
4630.125	2.27	5.59	263.5	0.350	235.0	0.321	+10.4	+ 8.2
4625.052	3.23	5.79	221.5	0.310	230.0	0.307	- 3.8	+ 0.9
4627.549	3.30	5.97	85.0	0.150	95.0	0.160	-11.7	- 6.6
4587.137	3.57	6.25	90.0	0.142	102.0	0.154	-10.5	- 8.4
4584.724	3.60	6.28	133.2	0.225	150.0	0.215	+12.0	+ 4.4
4611.285	3.64	6.31	301.3	0.320	275.0	0.325	+ 8.3	- 1.5
					Mean	Mean	- 0.2	0.3
					σ	σ	9.0	6.1
<u>Fe II lines:</u>								
4583.840	2.79	5.49	550.0	0.656	520.0	0.610	+ 5.4	+ 7.0
4555.890	2.82	5.52	370.0	0.520	350.0	0.513	+ 5.4	+ 1.3
4620.513	2.82	5.49	220.0	0.320	240.0	0.327	-13.5	- 2.2
4582.835	2.83	5.52	270.0	0.458	255.0	0.407	+ 5.5	+ 8.8
4576.331	2.83	5.52	255.7	0.320	270.0	0.347	- 5.5	- 8.4
4629.330	2.81	5.46	449.0	0.493	450.0	0.498	- 0.02	- 1.0
4635.330	5.93	8.59	135.0	0.345				
					Total	Mean	- 0.3	0.6
						σ	8.2	6.0

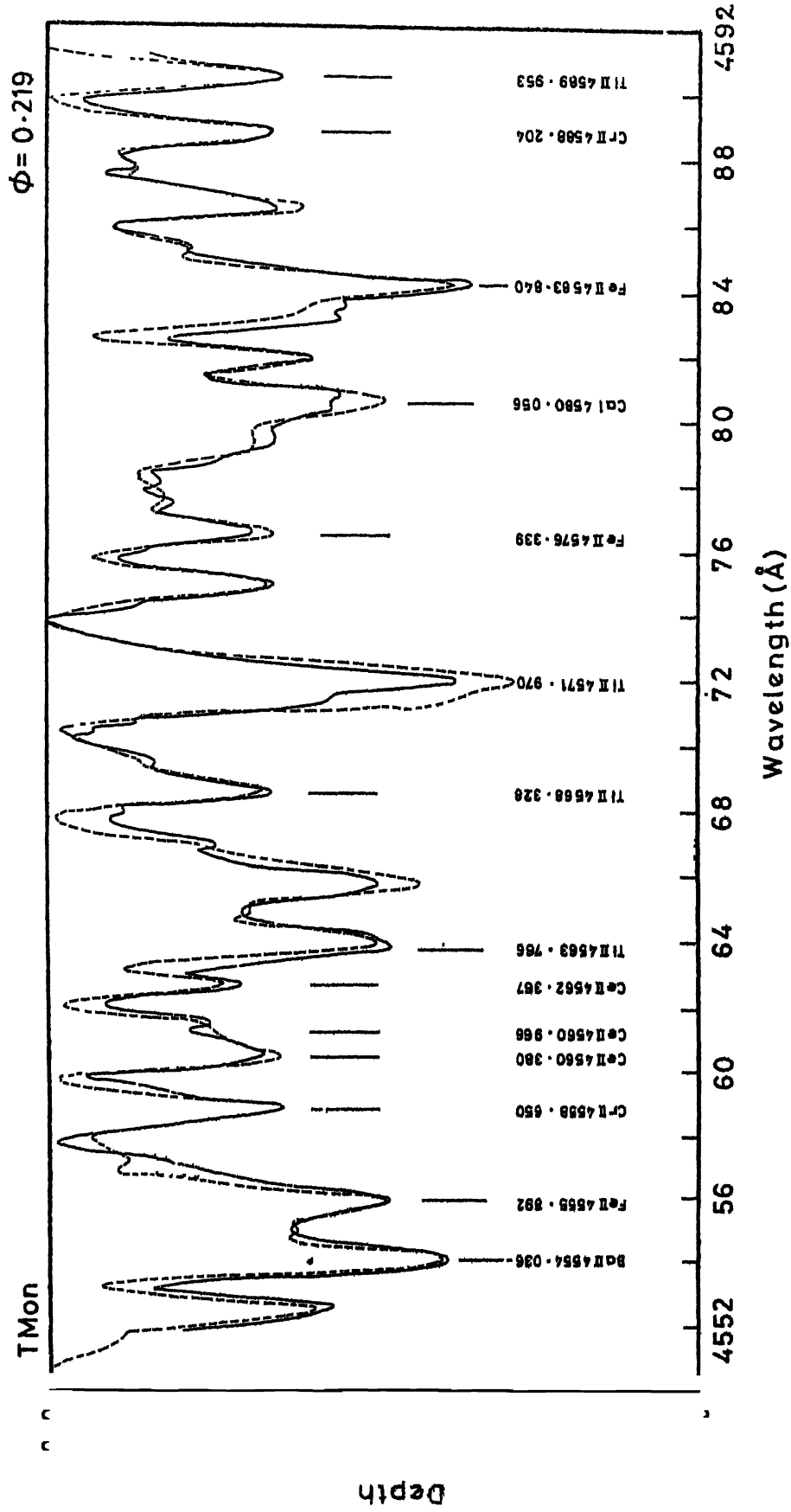


Figure 5.2 Observed (continuous line) and computed (broken line) spectra of T Mon; 4550-4590 Å. 29

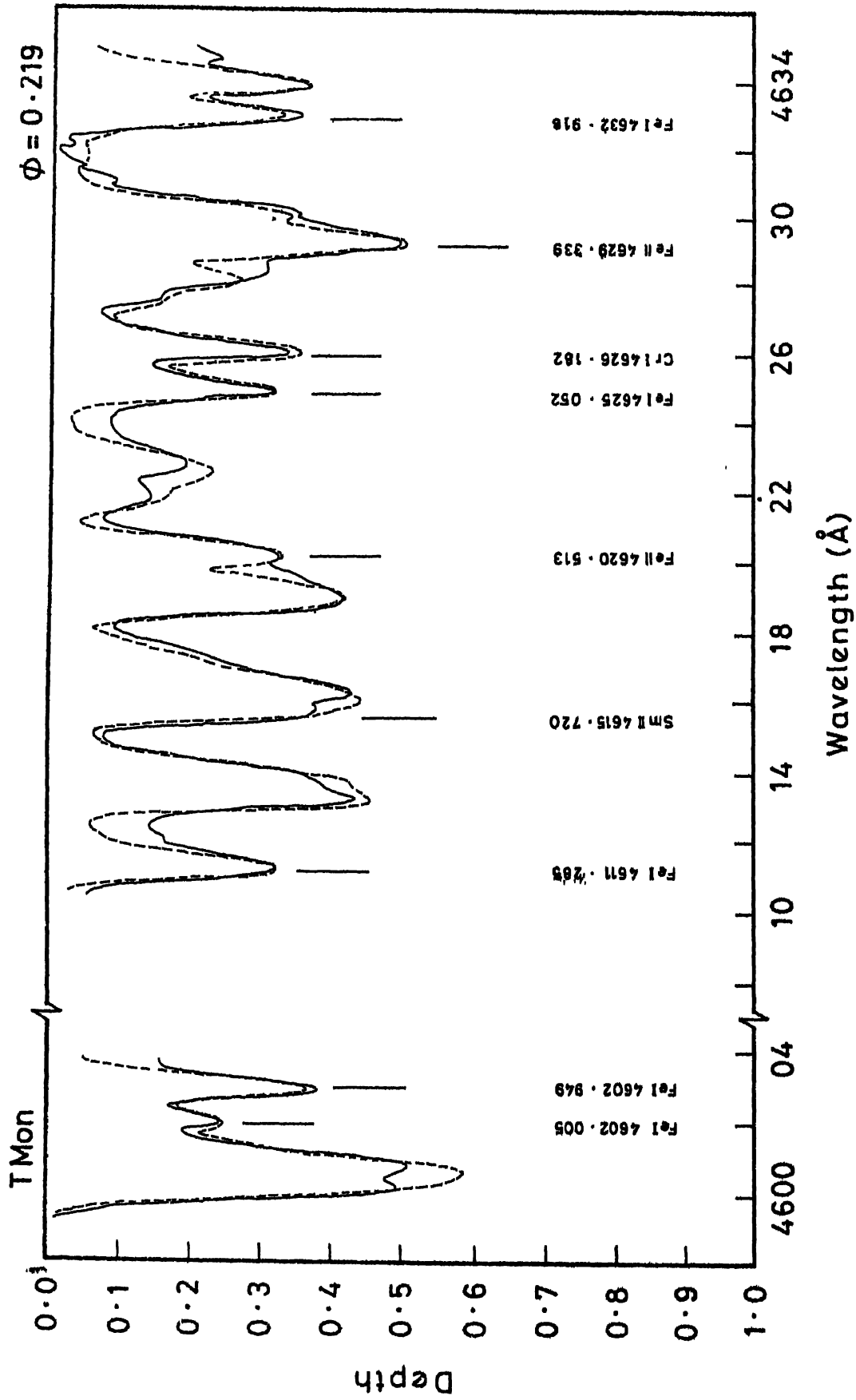


Figure 5.3 Observed (continuous line) and computed (broken line) spectra of T Mon; 4600-4635 Å.

In the last two columns of Table 5.2, we give percentage difference between the observed and computed equivalent widths

$$\Delta W = 100 (W_{\text{obs}} - W_{\text{comp}}) / W_{\text{obs}}$$

and the similar derivation in central depth

$$\Delta CD = 100 (CD_{\text{obs}} - CD_{\text{comp}}) / CD_{\text{obs}}$$

It is seen that the mean deviations are close to zero for both Fe I and Fe II lines independent of whether W or CD was compared. Also the overall standard error of the fit is 6.0% in CD and 8.2% in W. It should be noted that the central depths can be determined more accurately than the equivalent widths. Hence, the error in CD reflects the true error of the fit and the additional 5.6% error $\left[\sqrt{(8.2)^2 - (6.2)^2} \right]$ in the equivalent widths arises from the inaccuracies in the few equivalent widths that were directly measured.

Next, the abundances of different elements were altered by different amounts until the best fit of the observed spectrum and the computed spectrum was obtained. Figures (5.2) and (5.3) show two sections of the spectrograms δ 1161 of T Mon. The continuous line is the observed spectrum whereas the broken line is the computed one. The identifications and wavelengths of some important lines are also given

in the figure. The final abundances are listed in Table 5.5. $[Fe]$ abundance computed by Luck and Lambert (1981) for T Mon is higher than our estimate by 0.09 dex; $[Ce/Fe]$ computed by Luck is also higher by the same amount.

In Table 5.3 we present (at the phases of observations) atmospheric parameters and Fe abundances for our programme stars derived in our investigation. In Table 5.6, mean abundances of Fe, Cr, Te and s-process elements Y, Ba, La, Ce, Sm for T Mon, ζ Gem, and X Sgr derived in the present investigations are given. Mean abundance of these elements as derived by Luck and Lambert (1981) is also given to compare the results of the two investigations.

5.3 Other Stars Observed at Higher Resolution:

(1) Zeta Geminorum: The Cepheid ζ Gem is the prototype of Eggen's (1951) type C Cepheids with a nearly sinusoidal light curve and a period of 10.15 d. Photoelectric light curves were published by Harris (1953) and by Wisniewski and Johnson (1968). Radial velocity curves have been determined by Campbell (1901), Jacobsen (1926) and Evans (1976a). Using the light and radial-velocity curve obtained simultaneously, the radius has been determined by Evans (1976b). Scarfe (1976) has determined the radial velocity curve with better accuracy. The radius calculated by Evans (1976b) is $68 R_{\odot}$ which is in fair agreement with the radius determined by Fernie (1968)

Table 5.3

Derived model atmosphere parameters for the Cepheids

Star	Phase	T_{eff}	$\log g$	v_T	$12 + \log [Fe/H]$
X Sgr	0.258	6200	2.0	5.0	7.60
	0.394	6000	2.0	3.5	7.52
ζ Gem	0.238	5700	1.75	6.0	7.75
	0.427	5500	2.0	4.5	7.65
SV Mon	0.286	5800	1.5	5.0	7.40
	0.334	5600	1.5	5.0	7.40
WZ Sgr	0.219	5600	1.0	5.0	7.65
	0.941	6000	1.5	5.5	7.65
T Mon	0.219	5500	1.0	5.0	7.53
	0.255	5400	1.0	4.5	7.55

($R = 71 R_{\odot}$) and by Scarfe ($R = 67.6 R_{\odot}$). Scarfe (1976) has also reported a decrease in the period of ζ Gem at the rate of $3.12 \pm 0.08 \text{ s yr}^{-1}$.

Kautela and Joshi (1976) determined the temperature and gravity of ζ Gem at different phases by comparing the continuum energy distribution of the star with the model atmosphere fluxes of Parsons (1969). Schmidt (1972b) has determined the temperature at three phases by comparing the measured slopes of the Paschen continuum for the star and for model atmosphere fluxes. Equivalent widths of the heavy element lines in $5800\text{\AA} - 6800\text{\AA}$ region have been published by Schmidt, Rosendhal and Jewsbury (1974b). Luck and Lambert (1981) have determined the abundances of C, N, O and heavier elements using the method of spectrum synthesis.

Compared to our spectroscopic determinations, the temperatures derived by Kautela and Joshi are systematically higher by 400K, the ones derived by Parsons are cooler by 200K, while the estimates of Luck are in fair agreement with ours. The gravities derived by Kautela and Joshi, Parsons, and Luck are all in fair agreement with our estimates (± 0.5): Our observed and computed spectra are shown in Figures (5.4) and (5.5) and derived abundances are listed in Table 5.5. The iron abundance determined by Luck and Lambert (1981) is 0.13 dex higher than our estimates while their $[Ce/Fe]$ is higher by 0.07 dex.

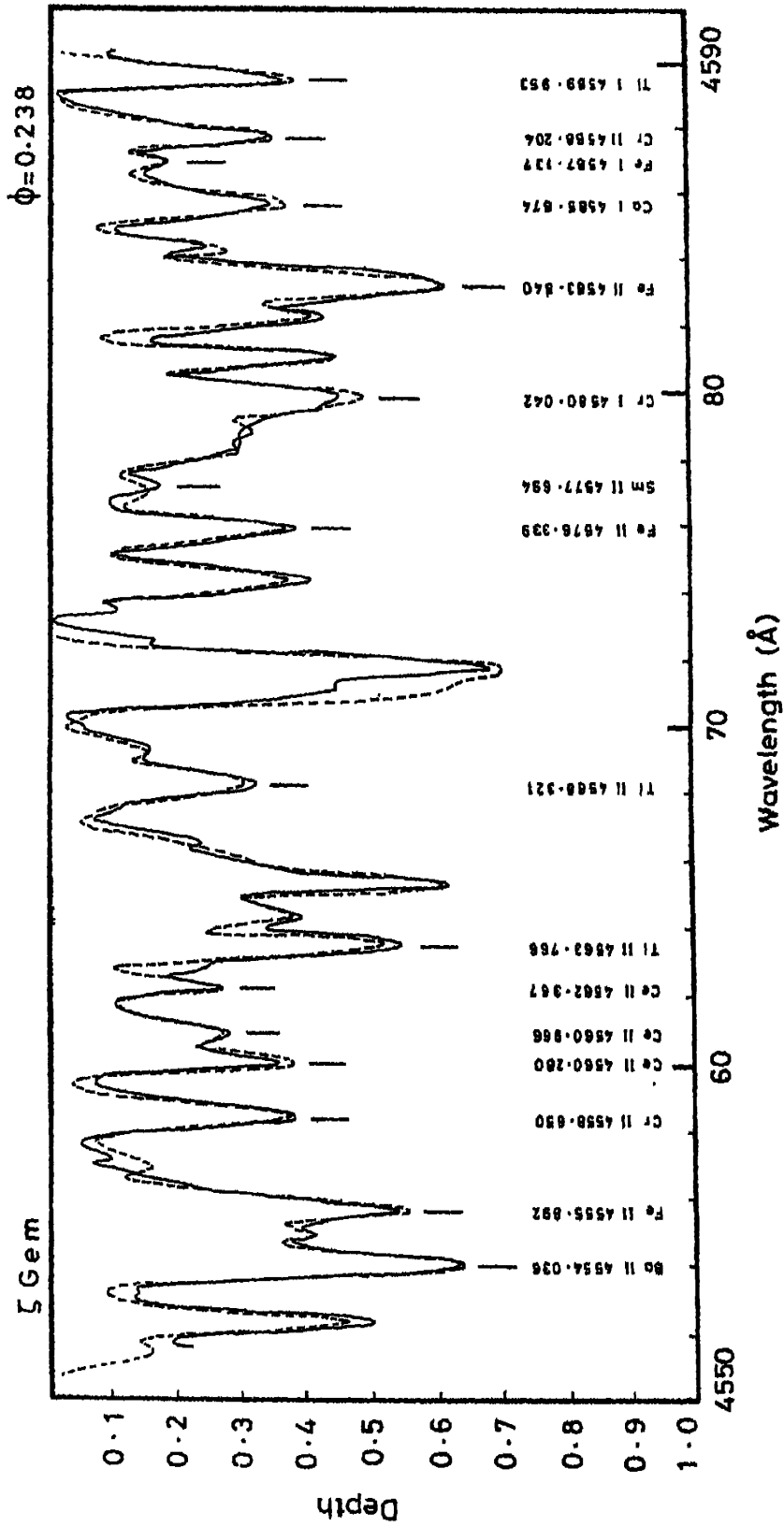


Figure 5.4 Observed (continuous line) and computed (broken line) spectra of ζ Gem;
 $\phi = 0.238$.

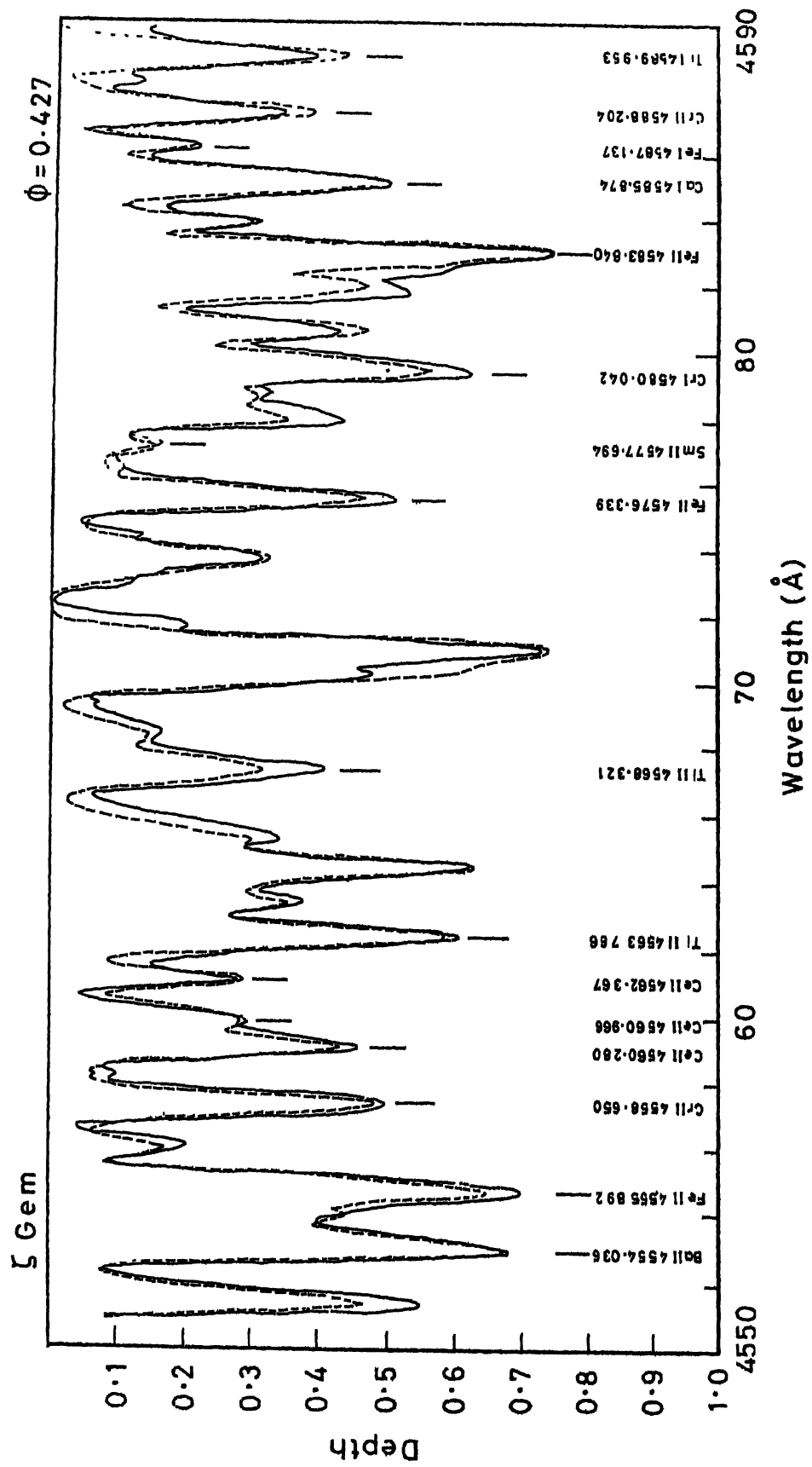


Figure 5.5 Observed (continuous line) and computed (broken line) spectra of ζ Gem; $\phi = 0.427$.

(2) X Sagittarii: X Sgr is a bright southern Cepheid. UBV photometry of this Cepheid was done by Mitchell et al (1964). Wisniewski and Johnson (1968) have determined the light curves in UBVRIJKL bands. Walraven, Tinbergen and Walraven (1964) and Pel (1976) have determined the light curves in UBLUW system. Light curves of X Sgr are asymmetric. Pel (1978) has reported some peculiarities in the two-colour loop in the (B-L) - (V-B) diagram which is generally used to determine the colour excess. Evans (1968) examined radial velocity curves derived by various investigators (e.g. Joy 1937; Stibbs 1955), but did not find any suggestion of a binary companion. High-resolution spectrophotometry in the ultraviolet (e.g. Mariska, Doschek and Feldman 1980) is more decisive in indicating the presence of faint photometric companions to Cepheids; an attempt needs to be made in this direction. Radius of X Sgr determined from period-radius relationship is $57.6 R_{\odot}$.

Despite being one of the brightest Cepheids in the southern sky, X Sgr has not been studied in a great detail. Schmidt (1971), Schmidt, Rosendhal and Jewsbury (1974) derived atmospheric parameters and abundances of iron peak elements for several bright southern Cepheids, but not of X Sgr. Abundances of CNO and other heavier elements derived by Luck and Lambert (1981) are the first estimates of abundances so far. Our determination of abundances are listed in Table 5.5. Iron abundance determined by Luck and Lambert is lower than ours

by 0.05 dex. The observed and computed spectra are shown in Figures(5.6), (5.7) and (5.8).

5.4. Stars observed at Lower Dispersion

(1) T Monocerotis: T Monocerotis was observed at the dispersions of 11.3\AA mm^{-1} as well as 22.6\AA mm^{-1} . Comparisons of the spectrograms obtained at the two dispersions helped us considerably in selecting the features which are useful even at the lower resolution. We would like to stress that lowering the dispersion does not necessarily imply the loss of accuracy since, in the method of spectrum synthesis, a spectral region is computed as a whole and we do not require the equivalent widths of individual lines. The most essential requirement in the method of spectrum synthesis is that all spectral lines which lie in the spectral region must be identified and must have known atomic constants. In Table 5.4, we present the observed and computed central depths of iron lines which were used in improving the estimates of the atmospheric parameters. The lines for lower dispersion were selected on the following criteria:

1) The lines which are main contributors to blends with no strong lines in the close neighbourhood to affect their central depths were preferred.

2) If a feature is made up of lines of the same element with no significant difference between the excitation

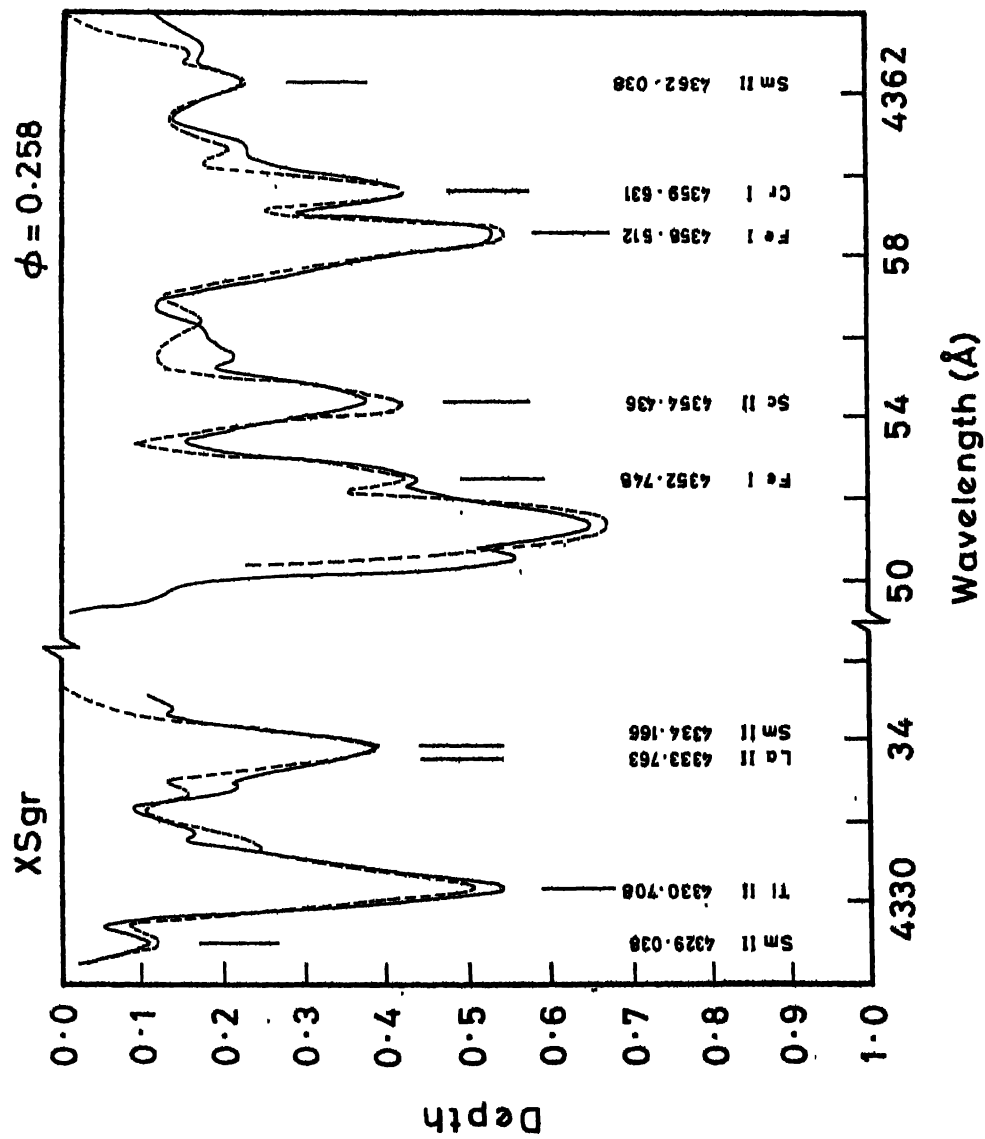


Figure 5.6 Observed (continuous line) and computed (broken line) spectra of X Sgr; $\phi = 0.258$, 4328-4364 Å.

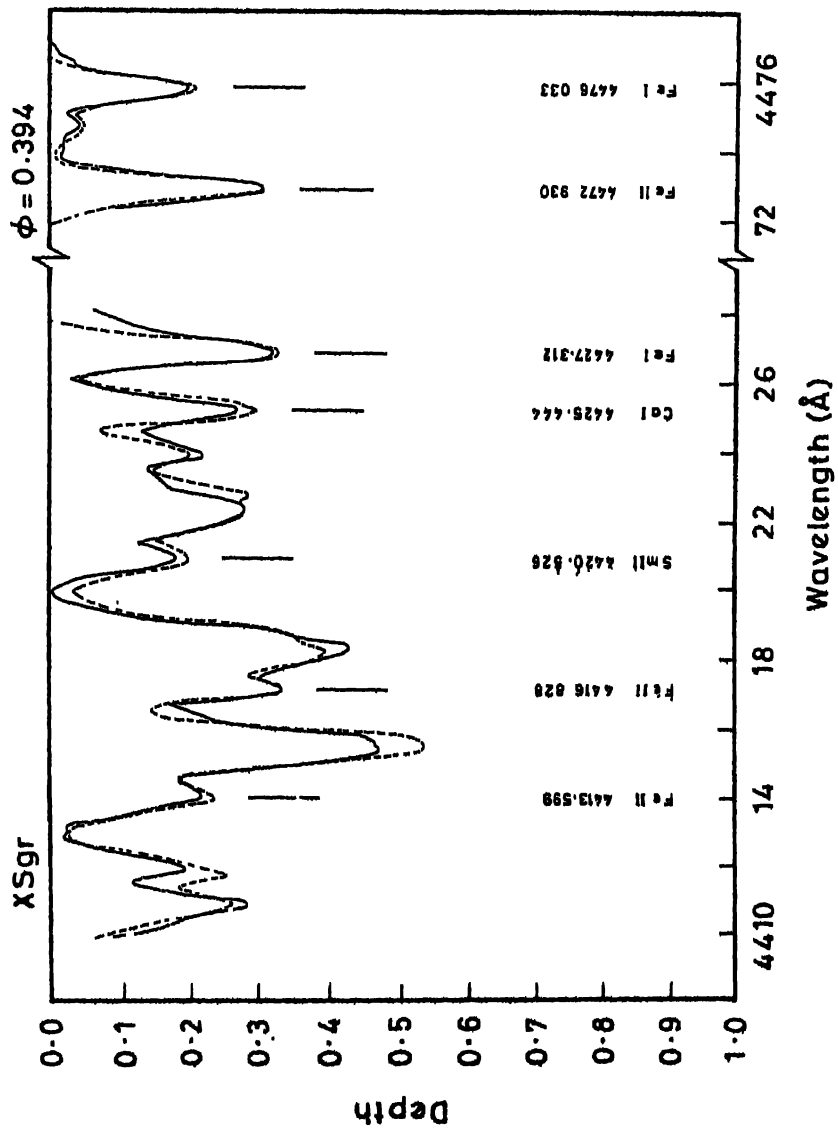


Figure 5.7 Observed (continuous line) and computed (broken line) spectra of X Sgr; $\phi = 0.394$, 4410-4476 Å.

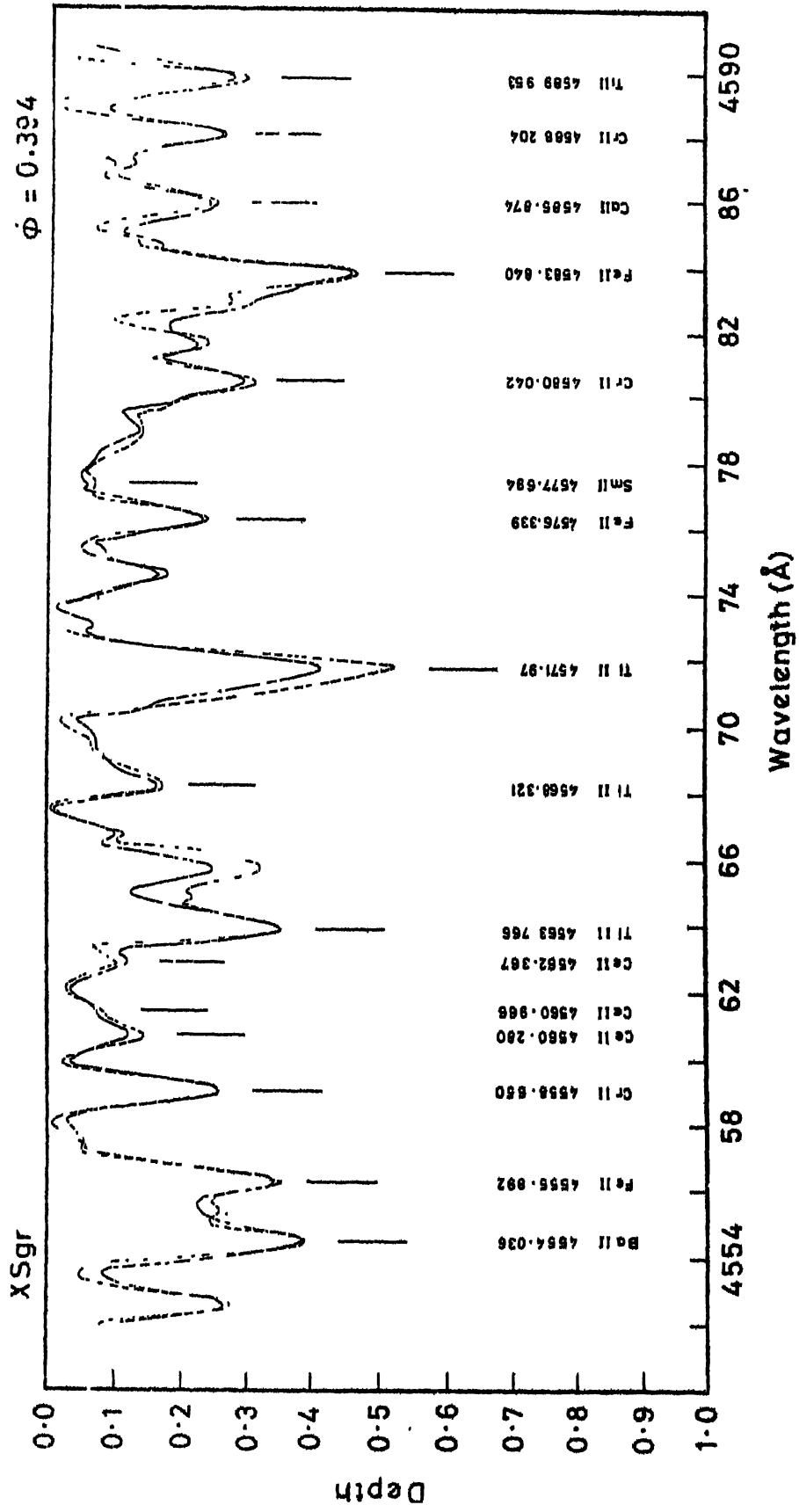


Figure 5.8 Observed (continuous line) and computed (broken line) spectra of X Sgr; $\phi = 0.394$, 4552-4590 Å.

Table 5.4

Fe lines used in improving the parameters of T Mon based
on low-dispersion spectra

λ	E1	E2	Central Depth		O-C %
			Observed	Computed	
4427.312	0.05	2.84	0.390	0.350	+ 10.2
4415.135	1.60	4.40	0.475	0.560	- 17.8
4352.748	2.21	5.05	0.300	0.310	- 3.3
4476.030	2.84	5.59	0.137	0.170	- 17.6
4358.517	2.94	5.77	0.427	0.440	- 3.0
4401.451	2.83	5.63	0.534	0.575	- 7.4
4360.797	3.63	6.46	0.230	0.210	+ 8.7
4413.699	2.68	5.46	0.275	0.270	+ 1.8
4583.840	2.79	5.52	0.445	0.425	+ 4.4
4515.327	2.82	5.52	0.310	0.280	+ 9.6
4576.339	2.83	5.59	0.187	0.200	- 6.9
4472.920	2.83	5.59	0.200	0.190	+ 5.0
4508.283	2.84	5.56	0.225	0.200	+ 11.1
4555.892	2.84	5.52	0.470	0.480	+ 02.1
			mean	=	-1.184
			σ	=	9.3237

potentials of contributing lines, then the blend can be treated as a single line. Cowley (1970) has suggested the use of blend equivalent widths even in the curve-of-growth technique. Our investigation support his idea. Ce II lines 4560.280 and 4560.966 which are seen well resolved in Figure (5.2) present themselves as a single feature at lower dispersion. The lower excitation potentials of these lines (0.43 and 0.20 eV) are not significantly different. This feature is useful for a determination of Ce abundance.

Abundances derived from the low-dispersion spectra of T Mon (Table 5.5) agree well with the ones derived at higher dispersion. The observed and computed low-dispersion spectra shown in Figures (5.9) and (5.10) demonstrate the utility of the method even at lower resolutions.

(2) SV Monocerotis: SV Mon is a relatively faint Cepheid ($m_v = 8.0$). Its UBV light curves are obtained by Mitchell et al (1964) and Eggen (1969). Light curves in VBLUW system are obtained by Walraven, Timbergen and Walraven (1964) and Pel (1976). Tsarevsky (1967) found some suggestion of slight variation in period. The light curves are highly asymmetric. However, Pel did not find any peculiarity in (B-L) - (V-B) diagram which could be attributed to the presence of a companion. Radial velocity curve for SV Mon was derived by Joy (1937) using prismatic spectra. No further spectroscopic

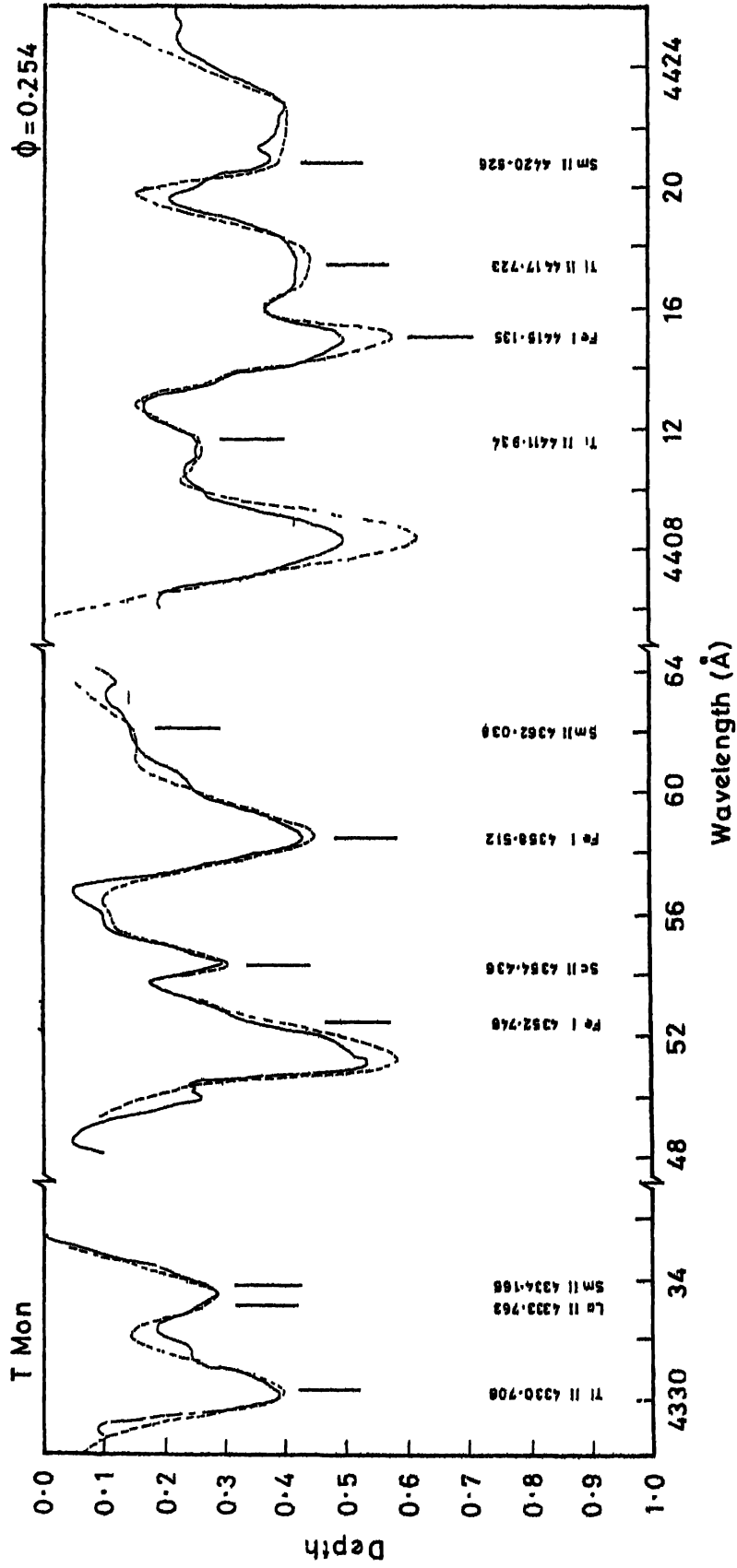


Figure 5.9 Observed (continuous line) and computed (broken line) spectra of T Mon at lower resolution; 4328-4426 Å.

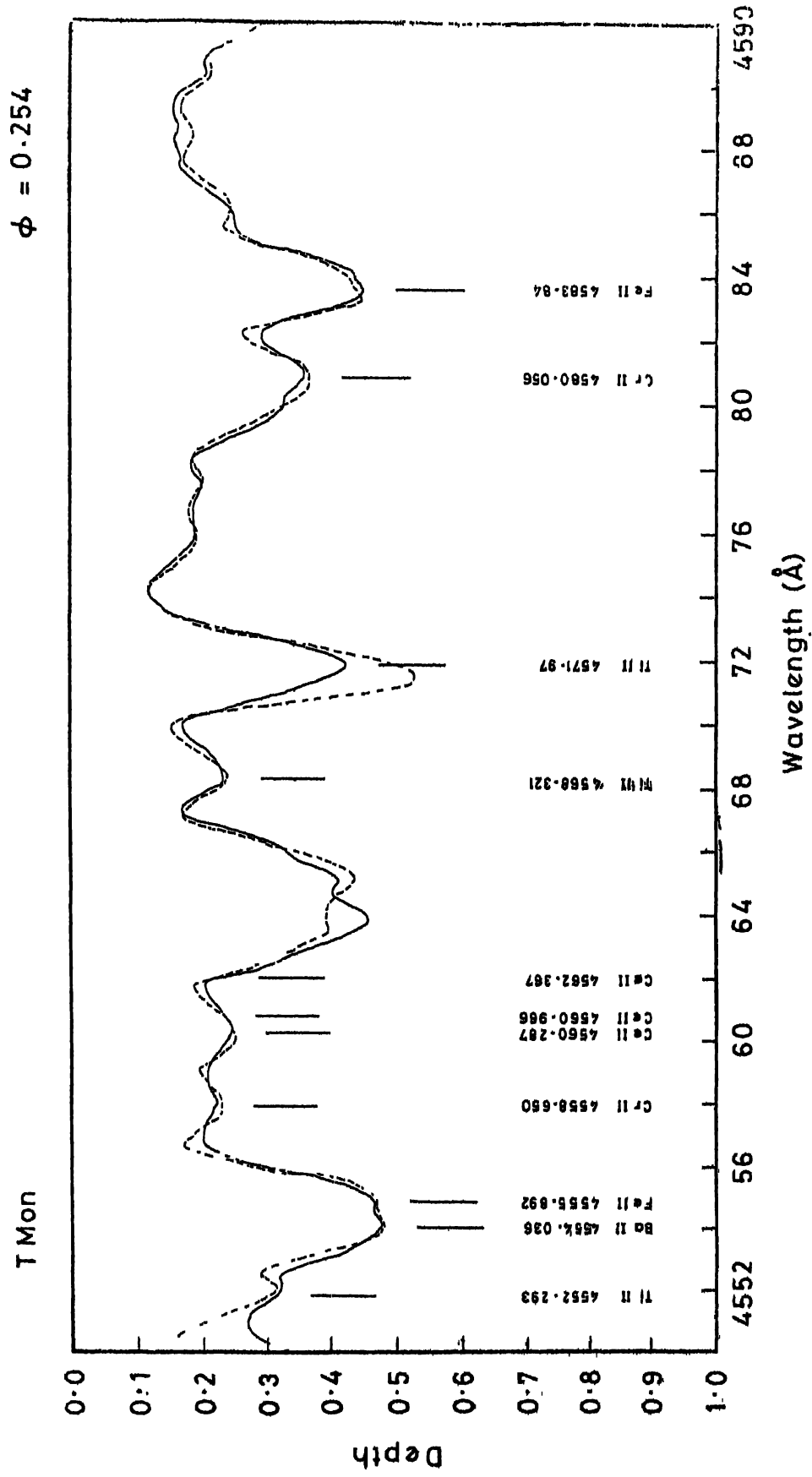


Figure 5.10 Observed (continuous line) and computed (broken line) spectra of T Mon at lower resolution; 4550-4590 Å.

investigation is done for this star. If we use radius relationship derived by Evans (1976b) the radius of the star turns out to be $R = 87 R_{\odot}$. Spectroscopic abundances of this star are determined for the first time in our investigation and are listed in Table 5.5. Observed and computed spectra are shown in Figures (5.11) and (5.12) and (5.13).

3) WZ Sagittarii: WZ Sgr is believed to be a member of Sgr-OB4 association (Tammann 1970). Light curves of this Cepheid in UBV photometric system are determined by Mitchell et al. (1964). Light curves in VBLUW colour system are obtained by Walraven, Tinbergen and Walraven (1964). Colour excesses are determined by Pei using $(B-L) - (V-B)$ diagram and he did not report any peculiarity in the intrinsic Cepheid locus which could be attributed to the presence of a companion. Radial-velocity curve was derived by Joy (1937). Spectroscopic abundances are determined for the first time in our investigations. Derived abundances are listed in Table 5.5. Observed and computed spectra are shown in Figures (5.14), (5.15) and (5.16).

5.5 Error Analysis

There are two main sources of error in the abundances derived here.

1) The errors in the input parameters like the observed equivalent width and the gf values manifest themselves as the

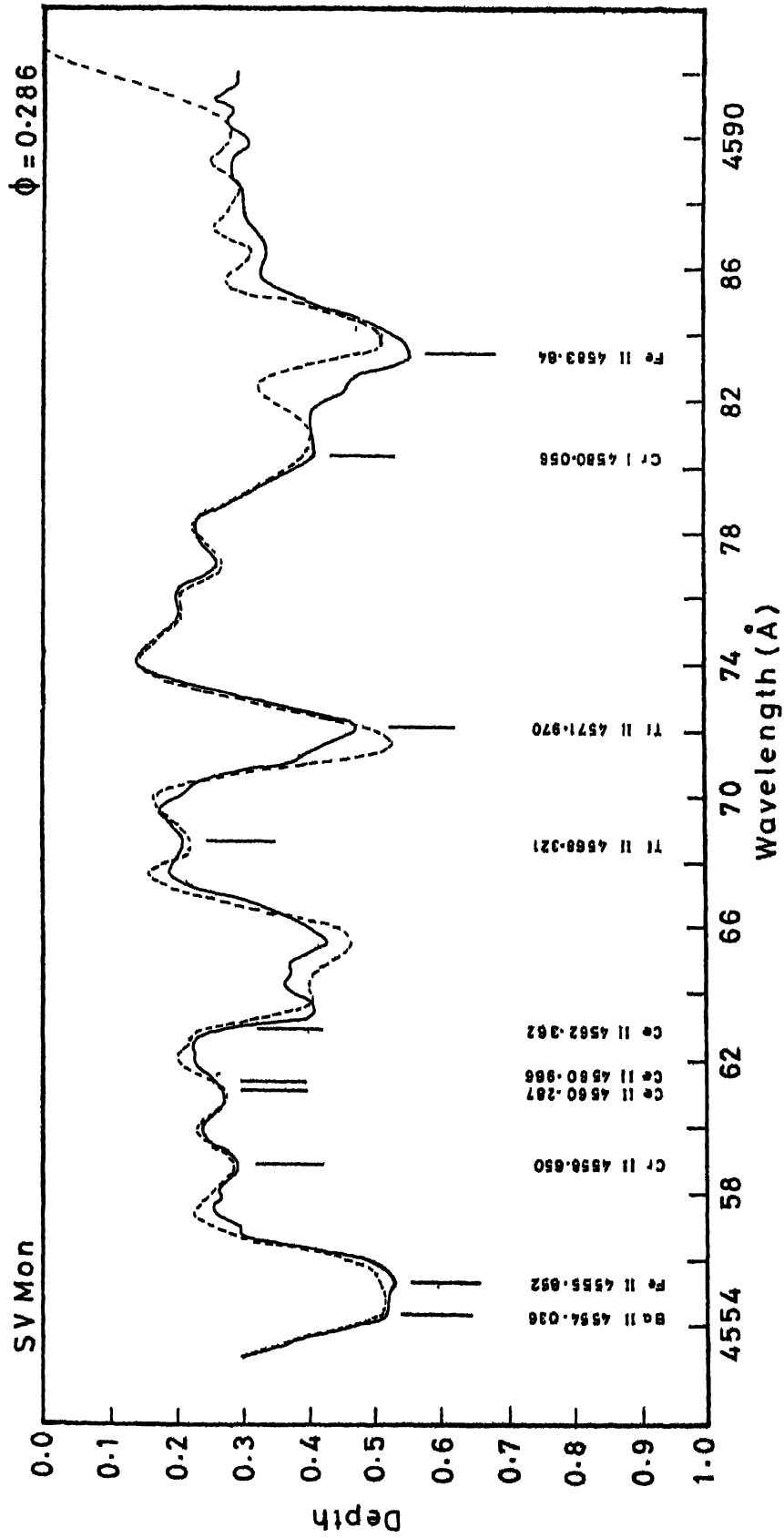


Figure 5.11 Observed (continuous line) and computed (broken line) spectra of SV Mon; $\phi = 0.286$, 4554--4592 Å.

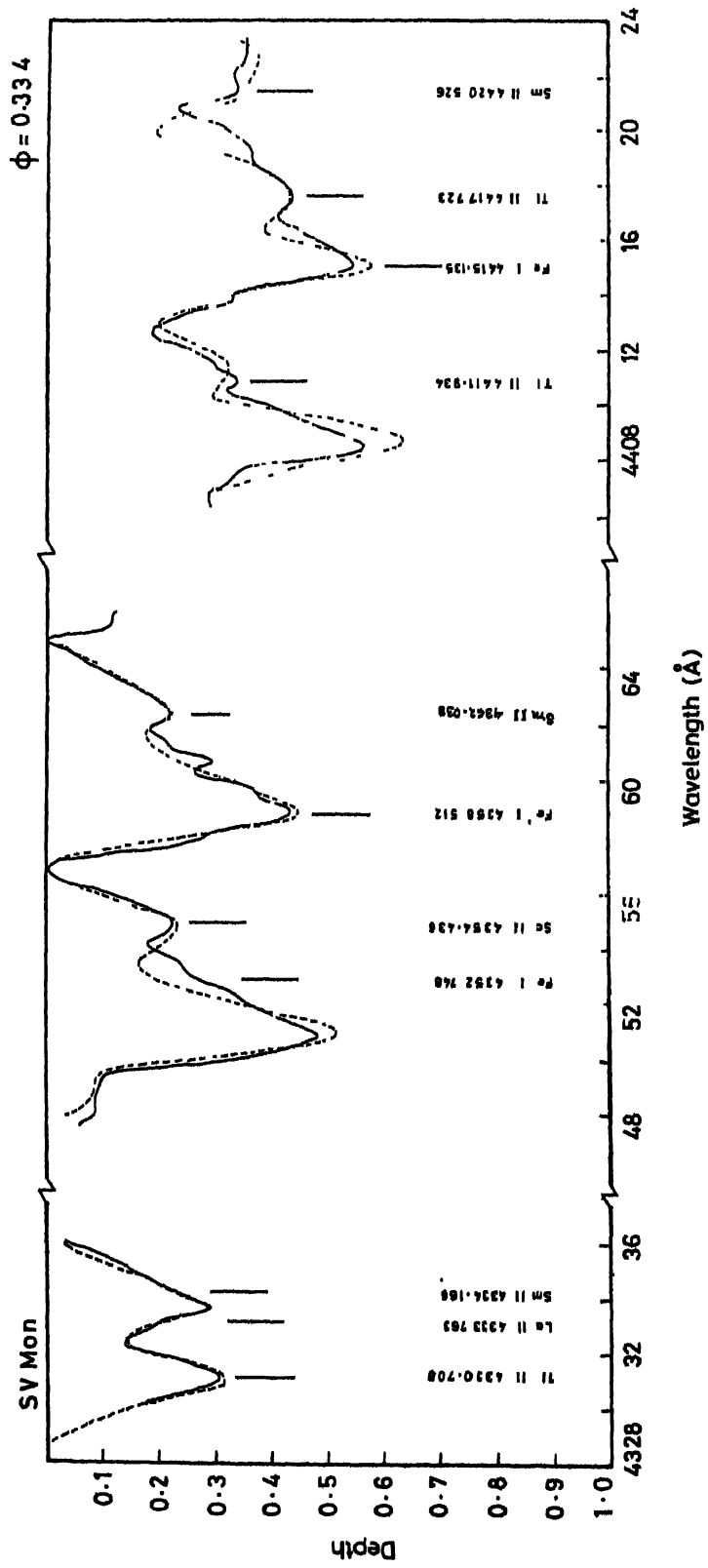


Figure 5.12 Observed (continuous line) and computed (broken line) spectra of SV Mon; $\phi = 0.334$, 4328-4424 Å.

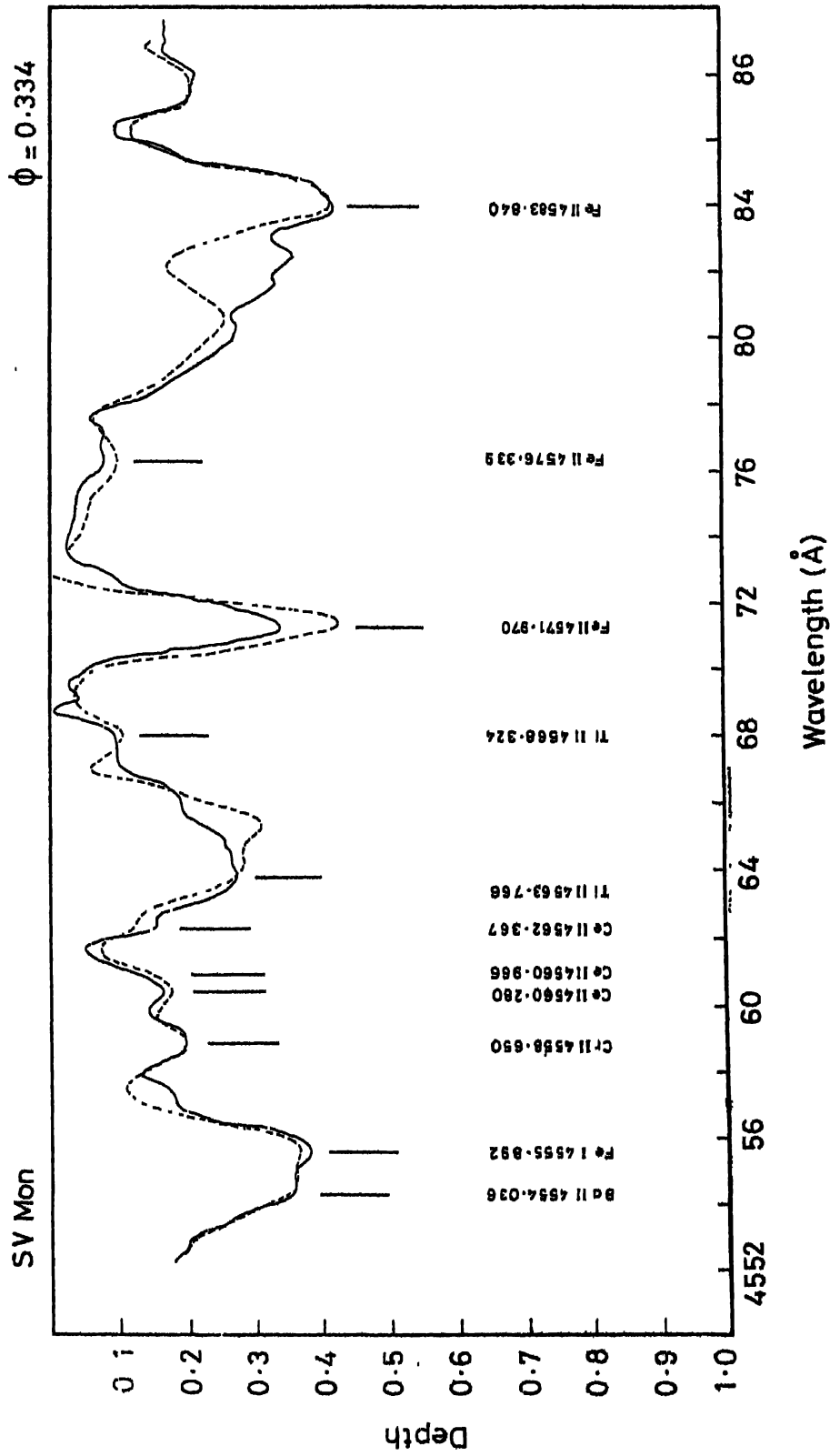


Figure 5.13 Observed (continuous line) and computed (broken line) spectra of SV Mon; $\phi = 0.334$, 4552-4586 Å.

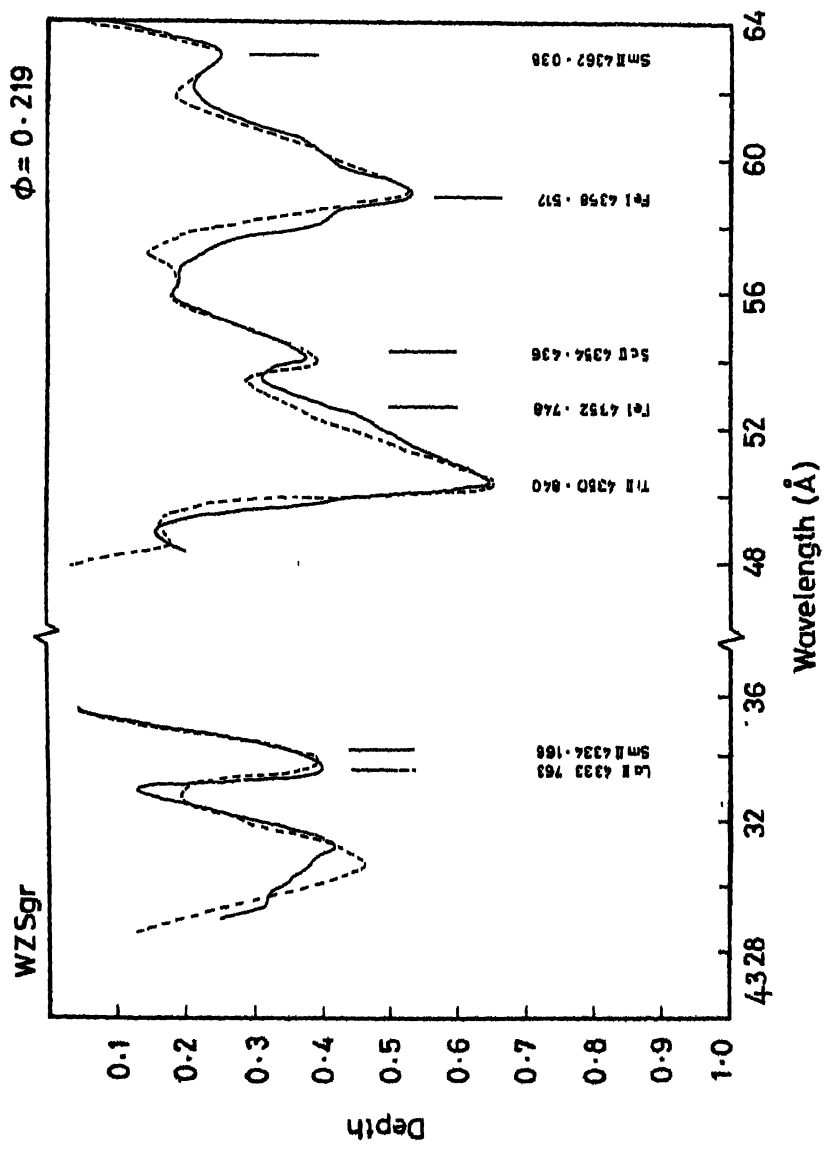


Figure 5.14 Observed (continuous line) and computed (broken line) spectra of WZ Sgr; $\phi = 0.219$, 4328–4364 Å.

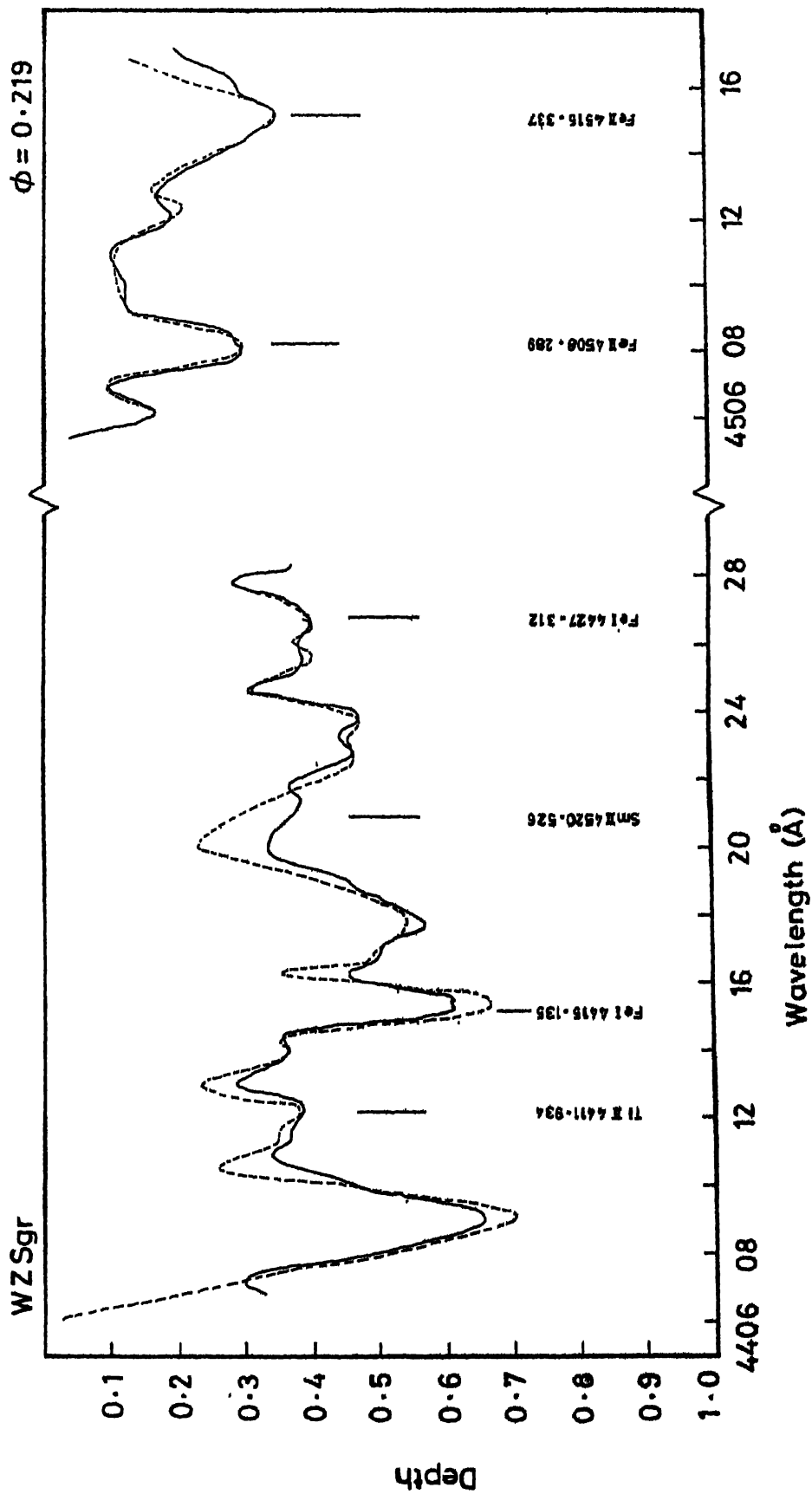


Figure 5.15 Observed (continuous line) and computed (broken line) spectra of WZ Sgr; $\phi = 0.219$, 4406-4516 Å.

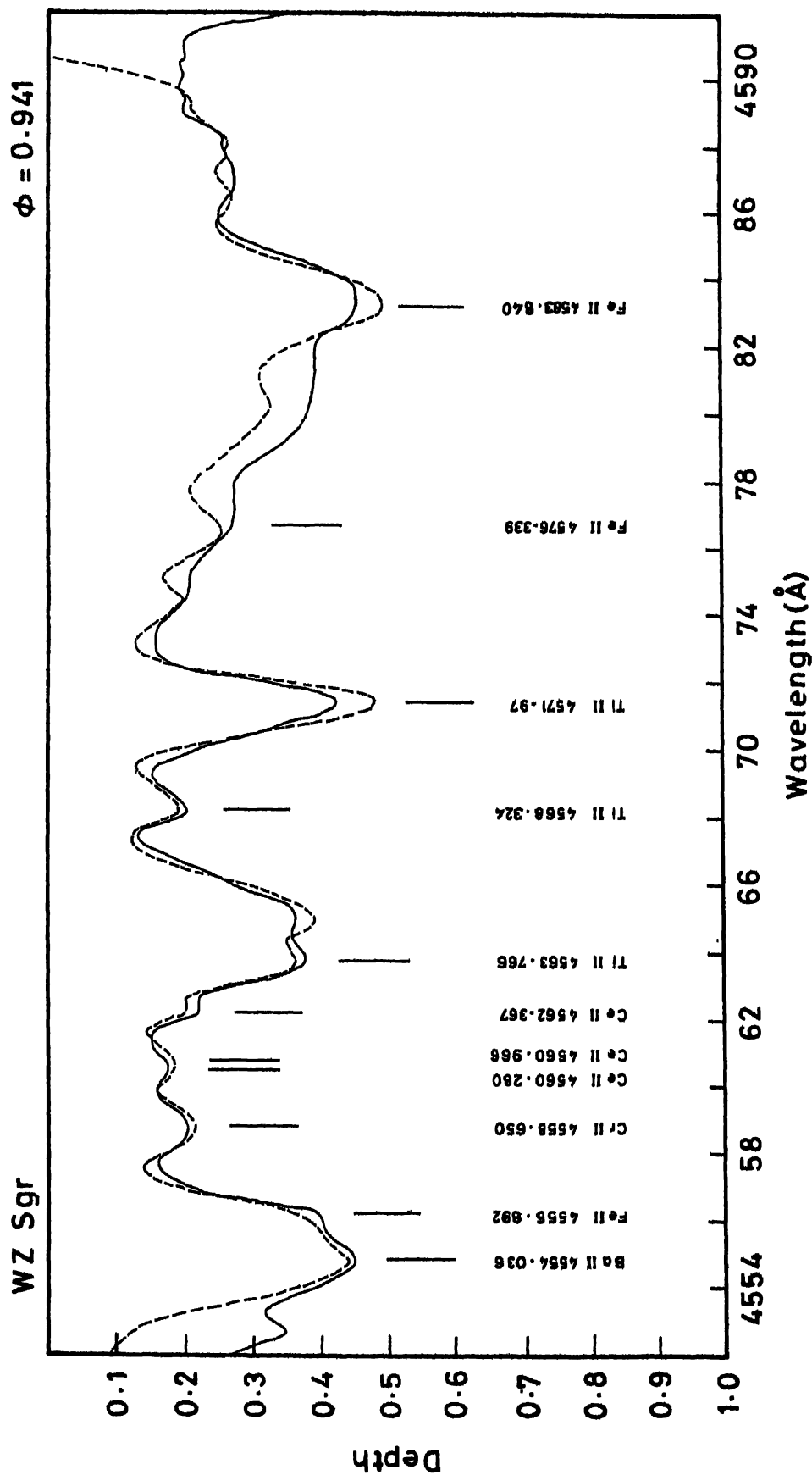


Figure 5.16 Observed (continuous line) and computed (broken line) spectra of WZ Sgr; $\phi = 0.941$, 4552-4592 Å.

Table 5.5

Cepheid abundances with respect to solar values

Element	Z	Lines	T Mon	T Mon	X Sgr	X Sgr	X Sgr	WZ Sgr	WZ Sgr	WZ Sgr	SV Mon	SV Mon	SV Mon	ζ_{Gem}	ζ_{Gem}
		Max	Min	$\phi =$	$\phi =$	$\phi =$	$\phi =$	$\phi =$	$\phi =$	$\phi =$	$\phi =$	$\phi =$	$\phi =$	$\phi =$	$\phi =$
				0.25	0.256	0.394	0.941	0.284	0.284	0.284	0.334	0.2	0.2	0.4	0.4
Ca	20	4	3	+0.10		-0.25								-0.1	-0.10
Sc	21	2	2												
Ti	22	6	4	0.0	+0.0	+0.12	-0.2	-0.3	-0.3	-0.3	-0.2	-0.2	-0.2	+0.1	+0.1
CR	24	12	6	+0.05	+0.1	+0.20	+0.25	+0.1	+0.1	+0.1	+0.1	+0.1	+0.1	+0.3	+0.25
Fe	26	20	6	+0.02	+0.05	+0.1	+0.15	+0.15	+0.1	+0.1	-0.1	-0.1	-0.1	+0.25	+0.15
Y	39	1	1												
Ba	56	1	1	+0.1	+0.1	-0.02	+0.15							+0.05	0.0
La	57	2	2											-0.2	-0.2
Ce	58	5	2	+0.07	+0.07	-0.2	-0.1	-0.3	-0.3	-0.3	-0.25	-0.25	-0.25	+0.15	+0.15
Sm	62	5	2	+0.02	-0.2	-0.2	+0.10	-0.2	-0.2	-0.2	-0.2	-0.2	-0.2	+0.25	+0.20

line-to-line scatter. This error can be evaluated statistically when the number of lines is large. For the element like iron for which a large number of lines ($n > 20$) could be measured, a typical standard deviation about the mean abundance is ± 0.08 dex. For Cr and Ti a less number of lines ($15 \lesssim n \lesssim 12$) are available and the standard deviation increases to ± 0.1 dex. For the elements with fewer than five lines, the errors are more difficult to assess since the standard deviation loses its statistical meaning. The errors in such cases probably lie in the range of $\pm 0.20 - 0.25$ dex.

2) The uncertainties in the model atmospheric parameters would also introduce errors, but such errors would be systematic rather than random. For an estimation of these errors, we computed selected Fe lines for the pairs of model atmospheres with

- i) the same gravity and microturbulent velocity, but different temperatures,
- ii) the same temperature and gravity, but different microturbulent velocities,
- iii) the same temperature and microturbulent velocity, but different gravities.

A comparison of the variations in the computed equivalent widths for the three cases mentioned above, with the

Table 5.6

Comparison of abundances derived in this study with those
of Luck and Lambert (1981)

Element	Sgr		ζ Gem		T Mon	
	L-L	Giridhar	L-L	Giridhar	L-L	Giridhar
Ti	+0.03	+0.13	+0.25	+0.10	+0.11	+0.0
Cr	+0.38	+0.20	+0.20	+0.27	+0.02	+0.07
Fe	+0.02	+0.07	+0.33	+0.20	+0.12	+0.03
Ba		-0.20		+0.25		-0.09
La	+0.32	-0.10	+0.48		+0.50	-0.10
Ce		-0.20	+0.21	+0.15	+0.06	+0.05
Sm		-0.20		+0.25		

Table 5.7

The sensitivity of computed line strength to different atmospheric parameters

λ	E1	E2	W_{λ} (mA)	(5500, 2.0; 5.0)	V Turb %	Temp	log g	Abundance
4602.944	1.40	4.16	292.0	10.0	5.0	2.8	4.4	
4602.005	1.60	4.28	187.4	9.0	8.05	2.88	6.7	
4630.125	2.27	4.93	229.0	7.9	6.00	7.3	4.6	
4476.021	2.83	5.59	291.2	8.0	5.6	3.7	5.1	
4517.530	3.06	5.79	182.0	6.0	8.0	4.5	6.4	
4625.052	3.23	5.90	213.9	9.7	9.0	7.5	6.2	
4587.134	3.57	6.25	106.0	10.1	16.0	2.4	15.0	
4611.285	3.64	6.31	267.0	6.6	15.0	11.0	7.3	
4584.824	3.60	6.28	166.0	6.7	16.0	7.2	10.3	
4583.840	2.79	5.49	455.0	8.0	6.5		4.0	
4515.327	2.82	5.52	312.7	8.2	7.00	6.6	4.4	
4620.513	2.82	5.49	224.6	10.8	8.50	6.8	10.8	
4582.835	2.83	5.52	250.3	8.0	7.00	6.6	4.8	
4576.331	2.83	5.53	230.2	13.5	7.04	12.0	6.5	
4472.920	2.83	5.59	315.2	8.7	3.55	4.5	4.9	
4508.283	2.84	5.58	285.8	8.5	6.00	6.6	3.56	

observational scatter (estimated to be 10%), leads us to believe that the accuracy of the adopted effective temperature is 250K, that of $\log g$ 0.25 and that of microturbulent velocity 0.5 km s^{-1} . The dependence of computed equivalent widths on the changes in the assumed atmospheric parameters are shown in Table 5.7. The equivalent widths for the lines given in Column 4 of Table 5.7 are computed for a model with $T_e = 5500\text{K}$, $\log g = 2.0$, $v_t = 5.0 \text{ km s}^{-1}$, assuming solar abundance. The percentage variations of equivalent widths due to an increase of v_t by 1 km s^{-1} , temperature by 200 K, $\log g$ by 0.5 and abundances by 0.1 dex are given in successive columns.

Error in abundances arising from the error in atmospheric parameters is not a gaussian sum of the errors due to the individual parameters. The parameters interact with each other; an error in the estimation of one parameter affects the estimates of other parameters. The net effect on the derived abundances would be considerably reduced when we employ a principle of consistency that the lines with a large range of excitation potentials, equivalent widths and different ionization states should lead us to the same abundances.

Thus we believe that the errors estimated from internal consistency represent the errors of this analysis well.

CHAPTER 6

RESULTS AND CONCLUSIONS

6.1 Compilation and Intercomparison of Spectroscopic
Abundances

We have summarized in Table 6.1, the basic data for the Cepheids for which spectroscopic abundances have been derived by different workers. The explanation of different columns is as follows: (1) name of the star, (2) galactic longitude, (3) galactic latitude, (4) pulsation period in days, (5) mean visual magnitude, (6) distance from the Sun, (7) galactocentric distance derived using a distance of 8.5 kpc to the galactic centre. The spectroscopic abundances computed from various sources and also the spectroscopic abundances derived in the present investigation are given in Table 6.2. The explanation of the various columns is as follows: (1) name of the star, (2) logarithmic abundance of Fe with respect to its solar value, (3) - (8) the ratios of logarithmic abundances of Y, Ba, La, Ce and Sm relative to Fe as compared to the solar value; i.e.

$$\left[\frac{X}{Fe} \right] = \text{Log} \left(\frac{X}{Fe} \right)^* - \text{Log} \left(\frac{X}{Fe} \right)^{\odot}$$

Column (9) gives the reference number for the various sources from which the abundances were compiled. These sources

Table 6.1

Basic data for Cepheids with known spectroscopic abundances

Star	l	b	Period days	m_v	r_θ	r_{gc}
WZ Sgr	12.10	-01.30	21.8497	9.00	1.82	6.73
SV Vul	63.94	00.30	45.0350	6.73	2.12	7.80
S Nor	327.75	-05.39	9.7549	6.11	0.91	7.74
Y Oph	20.60	+10.38	17.12326	7.15	0.708	7.84
U Sgr	13.70	-04.45	6.7449	6.35	0.66	7.86
W Sgr	1.00	-4.0	7.59471	4.70	0.43	8.07
X Sgr	1.60	00.22	7.01225	4.79	0.37	8.13
X Cyg	76.87	- 4.26	16.38660	6.65	0.37	8.32
η Aql	40.93	-13.07	7.17664	4.08	0.27	8.29
T Vul	72.13	-10.15	4.43558	5.43	0.59	8.33
DT Cyg	76.54	-10.78	2.49930	6.06	0.43	8.41
l Car	283.20	-07.00	35.54120	4.33	0.43	8.41
β Dor	271.74	-32.78	9.84200	4.03	0.32	8.49
δ Cep	105.20	+00.5	5.33634	4.94	0.26	8.57
SU Cas	133.47	08.51	1.94930	6.38	0.33	8.73
ζ Gem	195.74	11.89	10.15082	3.68	0.35	8.83
kT Aur	183.14	8.9	3.72826	5.48	0.46	8.95
TU Cas	118.92	-11.40	2.1393	7.38	1.00	9.02
RS Pup	252.40	-00.20	41.3876	7.59	1.71	9.16
T Mon	203.63	-02.56	27.0205	5.59	1.20	9.61
SV Mon	203.63	-03.70	15.2321	8.30	2.54	10.874

Table 6.2

Compilation of spectroscopic abundances of Cepheids

Star	r_{gc}	[Fe/H]	[Y/Fe]	[Ba/Fe]	[La/Fe]	[Ce/Fe]	[Sm/Fe]	Source
WZ Sgr	6.73	0.15		0.00	-0.10	-0.20	-0.05	7
SV Vul	7.80	0.27			+0.14	-0.03		6
S Nor	7.74	0.10						3
Y Oph	7.84	0.18						3
U Sgr	7.86	0.10						3
K Pav	6.07	-0.42			-1.16	-1.25	-0.87	2
X Sgr	8.13	0.02		-0.09	+0.30	-0.27	-0.27	6
W Sgr	8.03	0.07	+0.03		+0.30	-0.27	-0.27	7
X Cyg	8.32	0.15	0.06		+0.16	+0.01		6
η Aql	8.29	0.08		+0.28	+0.16	+0.13	+0.24	4
T Vul	8.33	0.06			+0.46	+0.01		6
DT Cyg	8.41	-0.05			-0.09			6
I Car	8.41	+0.12	-0.05		+0.12			6
		0.0						2
β Dor	8.49	0.01	+0.28	+0.01	-0.28	-0.43	-0.64	2
δ Cep	8.57	+0.05	-0.06		+0.30	+0.09		6
		-0.06	+0.06	-0.04	-0.10	-0.06	-0.49	5
SU Cas	8.73	-0.12	0.04		-0.03			6
ζ Gem	8.83	+0.34	-0.106		+0.14	-0.121		6
RT Aur	8.96	+0.20		-0.05	-0.98	-0.05	+0.03	7
		-0.20	+0.16	-0.98	-0.98	-1.14	-0.56	1
		0.06	-0.10	-0.21	-0.21			6
RX Aur	10.25	-0.37		-0.71	+0.44	+0.11	+0.54	4
TU Cas	9.02	-0.13	-0.085		+0.135			6

Table 6.2 - continued

Star	r_{gc}	[Fe/H]	[Y/Fe]	[Ba/Fe]	[La/Fe]	[Ce/Fe]	[Sm/Fe]	Source
RS Pup	9.16	-0.07	+0.25			-0.09		6
T Mon	9.61	+0.12	+0.10	+0.07	+0.43	-0.06		6
		+0.03			-0.13	+0.03	-0.12	7
SV Mon	10.874	+0.17	-0.65	-0.03	-0.65	0.05	+0.47	4
		-0.10		0.00	+0.03	-0.17	-0.16	7

- Source
- 1) Bappu and Rajarajan (1969)
 - 2) Rodgers and Bell (1963, 1968)
 - 3) Schmidt (1971),
 - 4) Schmitt, Koenndhal and Jewsbury (1974),
 - 5) Van Paradijs (1971)
 - 6) Luck and Lambert (1981)
 - 7) Present study

for each reference number are given at the bottom of the table.

Abundances of a few of these stars have been estimated by a number of investigators. The differences in the abundance estimates by different workers reflect the differences in the methods employed and the quality of the observational data.

In the investigations of Rodgers and Bell (1963, 1968), Bappu and Raghavan (1969), Schmidt (1971), and Schmidt, Rosendhal and Jewsbury (1974), the atmospheric abundances have been derived at different phases of the pulsation cycle. (The abundances listed in Table 6.2 are the mean values). It has been seen that the abundances derived at different phases do not agree between themselves. The amplitude of variations around the mean value is ~ 0.25 dex. Such variations in abundance estimates result from the inaccuracies in the estimates of atmospheric parameters. At the phases between minimum to maximum i.e. the rising branch of the light curve where atmospheric properties are changing rapidly, the spectrum of the star does not resemble that of a normal yellow supergiant for its temperature (Kraft 1967). In the falling branch of the light curve where there is no rapid variation in the atmosphere of the star, the spectrum closely resembles that of a yellow supergiant. The portion of the (V-B) - (B-L) loop (see Chapter 4, Section 3) corresponding

to the falling branch is very much similar for all the Cepheids. Thus, these phases are most suitable for the abundance determinations. With the zero phase assigned to the light maximum, the portion of the descending branch close to the mean brightness level falls in the range 0.2 - 0.4 in phase. In our investigation, we have observed almost all the stars in this phase range except for WZ Sgr for which one of the two spectrograms was taken at a phase of 0.941; other spectrogram was taken at the phase of 0.219. It is seen (Chapter 5) that Cr and Fe abundances agree in both the cases and only [Ti] differs considerably. We have assumed the value of [Ti] derived at $\phi = 0.219$ in preference to the value derived at $\phi = 0.941$.

Earlier investigations of bright Cepheids by Rodgers and Bell (1963, 1968) and Bappa and Kaghavan (1969) reported marked underabundance of s-process elements in the Cepheid atmospheres. However, recent abundance determination of a large number of Cepheids by Luck and Lambert (1981) using the spectrum synthesis technique does not confirm this trend. Although, relative to Fe, the s-process elements Ce and Nd are lower than the solar value, the difference is seldom exceeding -0.3 dex. La is overabundant in some of the stars. In our stars also we find that [s/Fe] is lower than the solar value and the differences are similar to those observed by Luck and Lambert (1981), never exceeding -0.3 dex.

The abundance ratio $[X/Fe]$ for various elements derived in this study are listed in Table 6.3. The individual elements fall in two groups: (i) the lighter elements with $20 < Z < 24$ and (ii) the heavier elements with $56 < Z < 62$, with yttrium falling in between.

We have plotted in Figure (6.1) the derived $[X/Fe]$ as a function of atomic number Z . The derived abundances for different programme stars are shown using different symbols. For the sample of stars considered, mean abundance for each element is also shown with $\pm 1\sigma$ error bars. These mean values are slightly shifted in the Z direction so as to maintain clarity. The mean abundance levels for both the groups of elements (light and heavy) are shown by dashed lines.

Within the errors of estimation, there are no systematic differences between $[X/Fe]$ for different stars, except for a possible underabundance of Ti and Ca in WZ Sgr and ζ Gem, $[X/Fe]$ has a tendency to increase with Z for the lighter elements and possibly a slight decreasing trend for heavier elements. Ca is overdeficient in all the stars, and more conspicuously in X Sgr and ζ Gem. Ti is deficient by a small amount and Cr is overabundant compared to the Sun. However, these differences are not significantly above the scatter in the individual abundances.

Table 6.3

Abundances derived in the present investigation

Z	[X/Fe]	X Sgr	χ Gem	SV Mon	WZ Sgr	T Mon	Mean	n	σ_{n-1}
20	Ca/Fe	-0.27	-0.3			0.08	-0.162	2	0.211
22	Ti/Fe	+0.06	-0.1	-0.07	-0.15	-0.03	-0.058	5	0.079
24	Cr/Fe	+0.13	+0.07	+0.2	+0.07	0.05	+0.104	5	0.061
20-24	mean	-0.026	-0.11	-0.065	-0.04	0.033	-0.038		
39	Y/Fe			0.0		-0.13	-0.065	2	
56	Ba/Fe	-0.09	-0.25	0.0	0.0	0.07	-0.054	5	0.1234
57	La/Fe			0.03	-0.1	-0.13	-0.082	3	0.076
58	Ce/Fe	-0.27	-0.05	-0.17	-0.2	0.04	-0.13	5	0.123
62	Sm/Fe	-0.27	+0.03	-0.10	-0.05	-0.12	-0.102	5	0.113
56-62	mean	-0.12	-0.10	-0.018	-0.071	-0.021	-0.092		

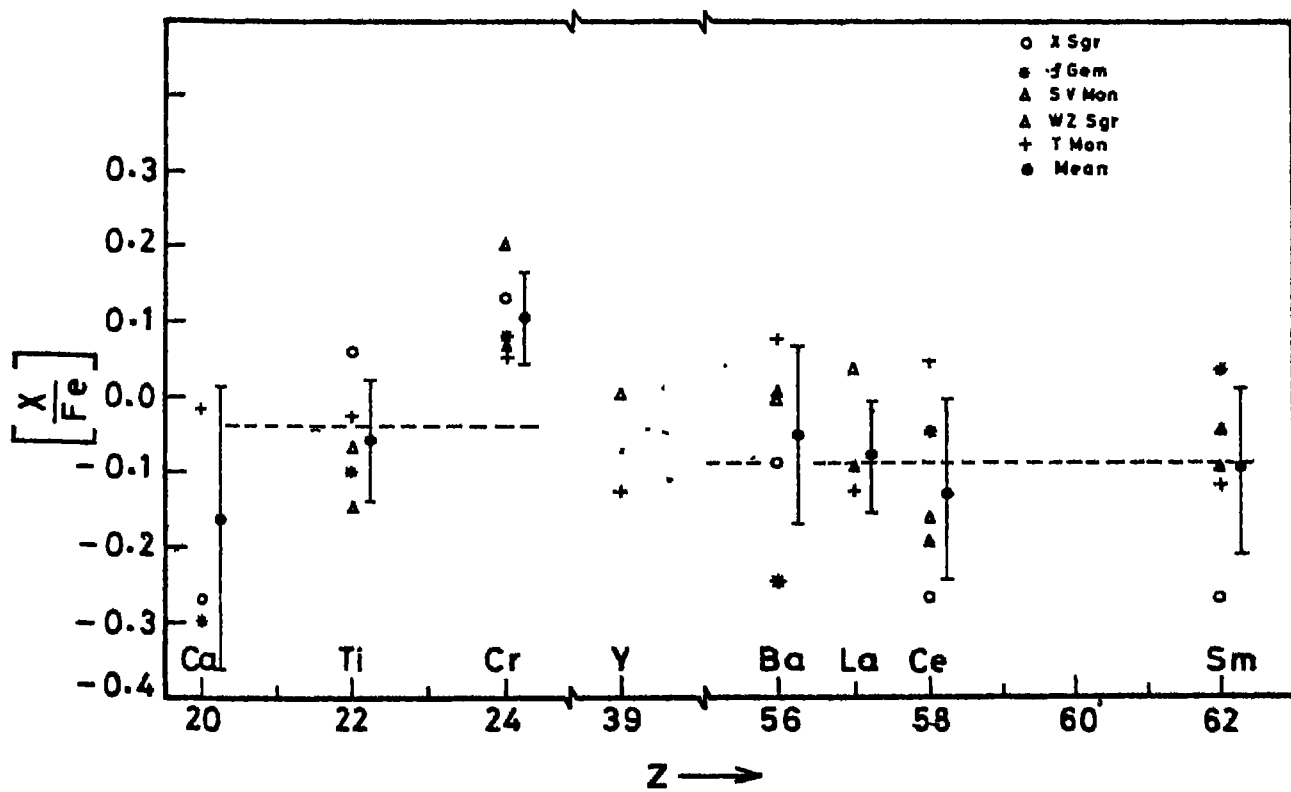


Figure 6.1 Observed abundance ratios $[X/Fe]$ as a function of atomic number.

Yttrium abundance was determined only for T Mon and SV Mon. The two values of $[Y/Fe]$ have a mean of -0.065 . The heavier s-process elements show a general underabundance, the average value of $[s/Fe]$ being -0.09 . Thus there is no evidence of s-processing or any other anomaly in the abundances of the sample stars.

6.2 The Radial Abundance Gradient in $[Fe/H]$

Figure(6.2) shows the location in the galactic plane of the stars for which the spectroscopic abundances are available. The outline of the spectral features are taken from Humphreys (1978) who used the associations of young stars, H II regions and young clusters to trace the optical features. In Figure(6.3) we have plotted $[Fe/H]$ for the stars of Table 6.1 as a function of their galactocentric distance (r_{gc}). A galactocentric distance of 8.5 kpc has been assumed for the sun in calculating these distances. Different symbols have been used for different investigators. This enables us to see the systematic differences between various investigations, as some of the stars have been included in two or three investigations. If we fit a straight line to this data we get the relation of the form

$$[Fe/H] = (-0.053 \pm 0.014) r_{gc} + 0.50 \pm 0.12 \quad (n = 30)$$

with a correlation coefficient of $r = -0.359$. The correlation

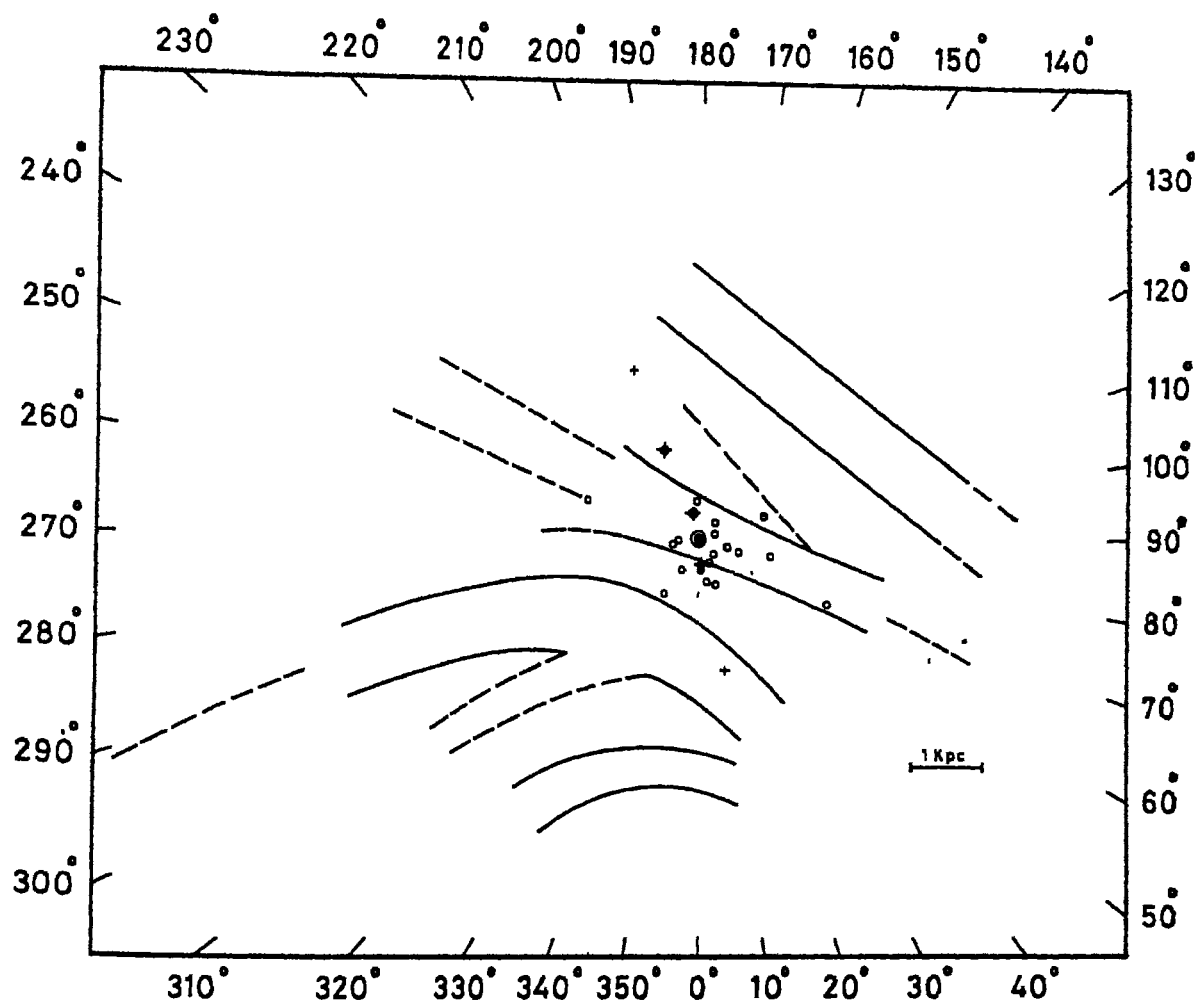


Figure 6.2 The galactic distribution of Cepheids. Spiral arms are traced from Humphreys (1978). Sun's position is shown by \odot symbol.

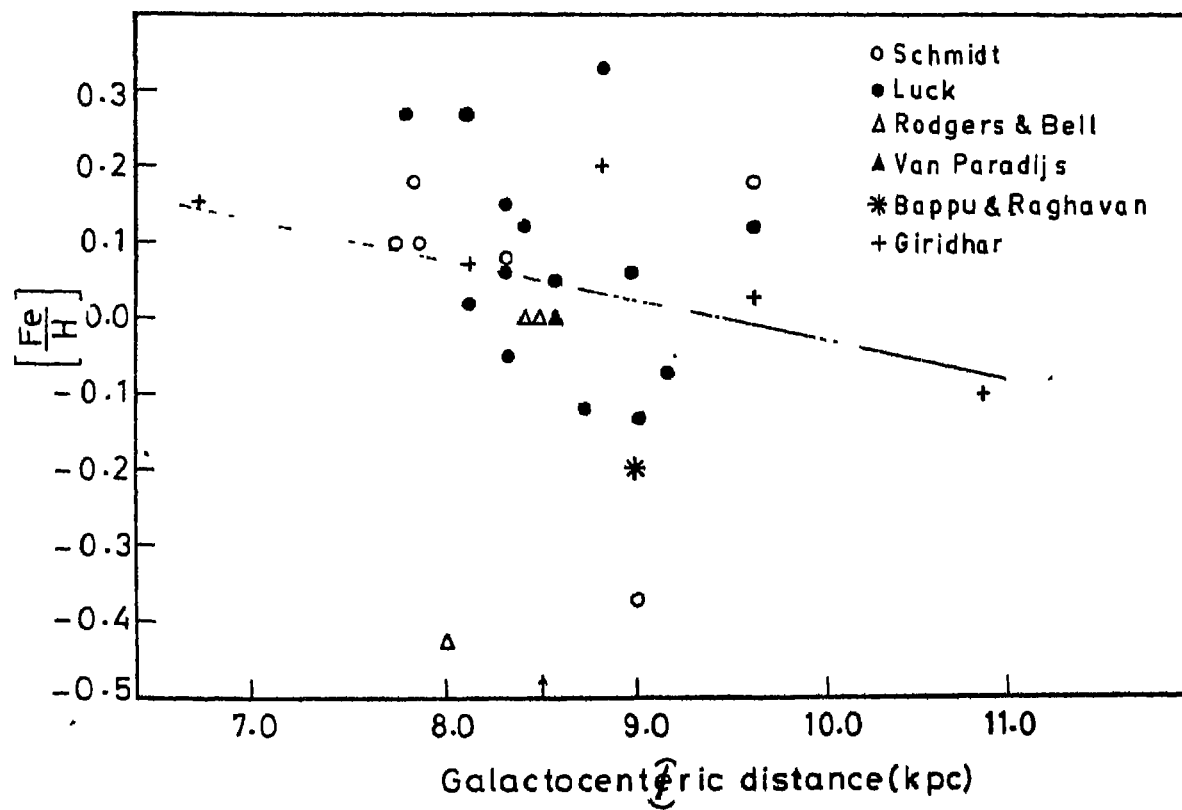


Figure 6.3 The radial abundance gradient in Fe. Sun's galactocentric position is shown by an arrow.

is thus rather weak. There is a 10% probability that this correlation is purely due to random effects. Harris (1981) determined photometric abundances of a large number of Cepheids using Washington colour system. These Cepheids cover a wide range of position in the galactic disc (5 to 15 kpc from the galactic centre). Harris derived an abundance gradient

$$\frac{d [A/H]}{dr_{gc}} = -0.07.$$

Using the iron abundances derived from supergiants and Cepheids in the earlier studies (Luck and Lambert 1981; Luck and Bond 1980) Luck (1982) derived a radial abundance gradient $\frac{d [Fe/H]}{dr_{gc}} = -0.13 \pm 0.03$ which is steeper than any abundance gradient determined so far. Pagel and Edmunds (1981) has questioned the use of supergiants in the determination of the radial abundance gradient, since the atmospheric abundances of these stars could be modified due to mixing with the interiors. We feel it is the small range in the galactocentric distance (7.7 - 10.6 kpc) covered by Luck which makes the derived abundance gradient rather uncertain. The present investigation covers a larger range of galactocentric distance (6.7 - 10.8 kpc) than that of Luck. Using the iron abundances and excluding Gem which is known to be metal rich for its position in the solar neighbourhood (Luck and Lambert 1981). We derive the relation (Figure 6.2),

$$[\text{Fe}/\text{H}] = -0.056 \pm 0.008 \quad r_{\text{gc}} + 0.53 \pm 0.07 \quad (n = 4)$$

with a correlation coefficient of -0.970 (3% chance that the correlation is spurious). This gradient is shallower than the gradient derived by Luck (1982) but in close agreement with the one derived by Janes (1979) using UDU photometry of a large number of K giants, and also with the estimates of Harris (1981). This value also agrees with the one derived from the total sample of 30 points, inclusive of Luck's sample, substantiating our claim that adding the two farthest Cepheids improves the derived gradient.

6.3 Local Chemical Inhomogeneities in Fe

Star formation in disks of galaxies is explained by Lin, Yuan and Shu (1969) as due to density-wave compression. In this picture, a spiral compression wave propagates at a constant angular velocity Ω_p through a disk of stars and gas rotating differentially with an angular velocity $\Omega(k)$ at a galactocentric distance k . Since $\Omega > \Omega_p$, the gas streams through the density wave at the inner edge, and consequently, the gas clouds are compressed and form stars. High mass stars explode and enrich the interstellar medium in a few million years after their formation. A star with a life time of $\sim 5 \times 10^6$ yr would move by an angle $\sim 4^\circ$ or by a distance of ~ 0.58 kpc across the spiral arm (at an assumed galactocentric distance of 8.5 kpc) before it

explodes. Such a supernova explosion may induce further stars formation. The shells of cold H II, dust and molecules around the supernova remnants have been observed by Sancisi (1974), and Knapp and Kerr (1974). Berkhuijsen (1974) and Herbst and Assousa (1977) found young stellar associations at the edge of supernova remnants.

Even if the star formation is not initiated by supernovae the material synthesized during explosive nucleosynthesis in the supernova will enrich the ISM and hence the next generation stars if the stars are formed after a time that is shorter than the time for this inhomogeneity to get mixed with surrounding medium. Thus it is important to know the birthsites of stars that belong to a single age group, in order to study the local chemical inhomogeneities.

A knowledge of the ages of stars is the most important prerequisite for an estimation of their birthsites. Fortunately, the age of a Cepheid can be determined from its pulsation period. Kippenhahn and Smith (1969) derived a period-age relationship for classical Cepheids from the stellar evolution theory. The calculations were based on stellar models with compositions $X = 0.602$ and $Z = 0.044$ without any mass loss. Analytical representation of their results as given by Tammann (1970) is $\log \tau_7 = 1.16 - 0.651 \log P$, where τ_7 is the age in 10^7 yr and P is the pulsation

period in days. Kippenhahn and Smith estimated a random error of $\pm 15\%$ for the derived age due to an intrinsic scatter in the period caused by the multiple crossing of the instability strip and due to the period changes within each crossing. Further, an eventual spread in the chemical composition and the effect of mass loss may lead to systematic errors with respect to observations. Inclusion of all these effects may increase the error estimates to $\pm 30\%$. Efremov (1978) derived a semi-empirical period-age relationship using the data on 64 Cepheids in clusters. The age of these Cepheids were determined from the ages of the clusters estimated using the theoretical colour-magnitude diagrams derived by Dixon, Ford and Robertson (1972). From the data on Cepheids in 29 clusters in Magellanic clouds, the Galaxy and M31, a composite period-age relationship was established as

$$\begin{aligned} \log \tau_7 &= 1.157 - 0.677 \log P \\ &\pm 0.37 \quad \pm 0.47 \end{aligned}$$

This relationship agrees closely with the theoretical one. We have listed in Table 6.4, the ages calculated using the semi-empirical period-age relationship of Efremov.

Detailed calculations of birth-sites of selected Cepheids have been made by Wielen (1973) by numerically

Table 6.4

Ages, birthsites and abundance residuals for Cepheids

S.No.	Star	r_{gc}	Age $\times 10^7 \text{yr}$	$\lambda = (\Omega - \Omega_p) \tau$	$\Delta \left[\frac{r_e}{H} \right]$
1	WZ Sgr	6.73	1.779	18.75	- 0.005
2	S Nor	7.74	3.071	24.98	0.0
3	Y Oph	7.84	2.098	16.59	0.08
4	U Sgr	7.86	3.943	31.18	0.0
5	κ Pav	8.08	3.227	24.08	- 0.42
6	X Sgr	8.13	3.800	27.99	- 0.05
7	W Sgr	8.07	3.638	26.53	+ 0.2
8	X Cyg	8.32	2.162	15.17	+ 0.083
9	η Aql	8.30	3.780	26.66	- 0.02
10	T Vul	8.34	5.236	36.55	- 0.12
11	DT Cyg	8.41	7.721	52.94	
12	l Car	8.41	1.279	8.77	- 0.05
13	β Dor	8.50	3.053	20.46	- 0.05
14	δ Cep	8.57	4.620	30.40	0.0
					- 0.05
15	SU Cas	8.73	9.136	57.69	
16	ζ Gem	8.83	2.989	18.40	+ 0.29
					+ 0.16
17	RT Aur	8.96	5.889	35.04	+ 0.03
					- 0.23
					- 0.40
18	TU Cas	9.03	8.578	50.12	- 0.20
19	RS Pup	9.16	1.151	6.52	- 0.09
20	T Mon	9.61	1.541	7.72	+ 0.13
					+ 0.04
					+ 0.18
21	SV Mon	10.874	2.271	17.96	- 0.02

integrating the galactic orbits of Cepheids backwards in time using the present positions and space velocities. The spiral field of the density wave was also included in the calculations. Wielen notes that the largest uncertainties in the birthsites arise due to the uncertainties in age. An error in age by 10^7 yr corresponds to an error of 1 kpc in birthsite, of which 0.1 kpc would be perpendicular to the spiral arm. In contrast, errors in space velocities of the Cepheids by $\pm 5 \text{ km s}^{-1}$ affect the birthsites by 0.3 kpc and inclusion of the gravitational field of the spiral density wave changes the birthsite by 0.2 kpc in 5×10^7 yr. Thus for the youngest of the Cepheids (age $\approx 3 \times 10^7$ yr), one may neglect these errors and obtain the birthsites with respect to the spiral arms by rotating their present radius vectors by an angle

$$\lambda = (\Omega - \frac{v}{p})\tau .$$

We have estimated in this fashion the birthsites of four Cepheids from Table 6.1 which are not in Wielen's list (Y Oph, X Cyg, SV Mon, KPav). We have used a value of $13.5 \text{ km s}^{-1} \text{ kpc}^{-1}$ for the pattern speed (Yuan 1969) and a constant rotation velocity of 212.5 km s^{-1} for the solar neighbourhood ($\Omega = 25 \text{ km s}^{-1} \text{ kpc}^{-1}$ from Oort's constants and $R_{\odot} = 8.5 \text{ kpc}$). TU Cas which is also not in Wielen's list is too old to derive an accurate birthsite in this

simplistic way.

We have plotted in Figure (6.4) the birthsites with respect to the spiral pattern deduced as above or obtained from Wielen's list. The outline of the spiral features are taken once again from Humphreys (1978). The birthsites of a large number of Cepheids are seen to be close to the Sagittarius - Carina arm. According to Lin, Yuan and Shu (1969) most of the nearby Cepheids probably originated in Sagittarius arm or in the Persius arm. Only the youngest Cepheids are probably born in the local feature. Figure (6.4) confirms this conclusion.

With the data on birthsites, we can study the chemical inhomogeneities across the spiral arm. Since Cepheids are relatively young objects, their atmospheric abundances reflect the abundances of the gas clouds out of which they are formed. It is of interest to study the departure of abundances in these stars with respect to the smoothed radial abundance distribution in the galaxy. Using the relationship determined by us (Figure 6.3) we have measured the departure $\Delta [Fe/H]$ of the Fe abundances of the Cepheids in Table 6.1. These values are listed in Table 6.4 for Cepheids with reliable abundance determinations. This requirement allowed us to include only the abundances derived by Luck and Lambert (1981), Bappu and Raghavan (1969), Van Paradijs (1971) and the present investigation.

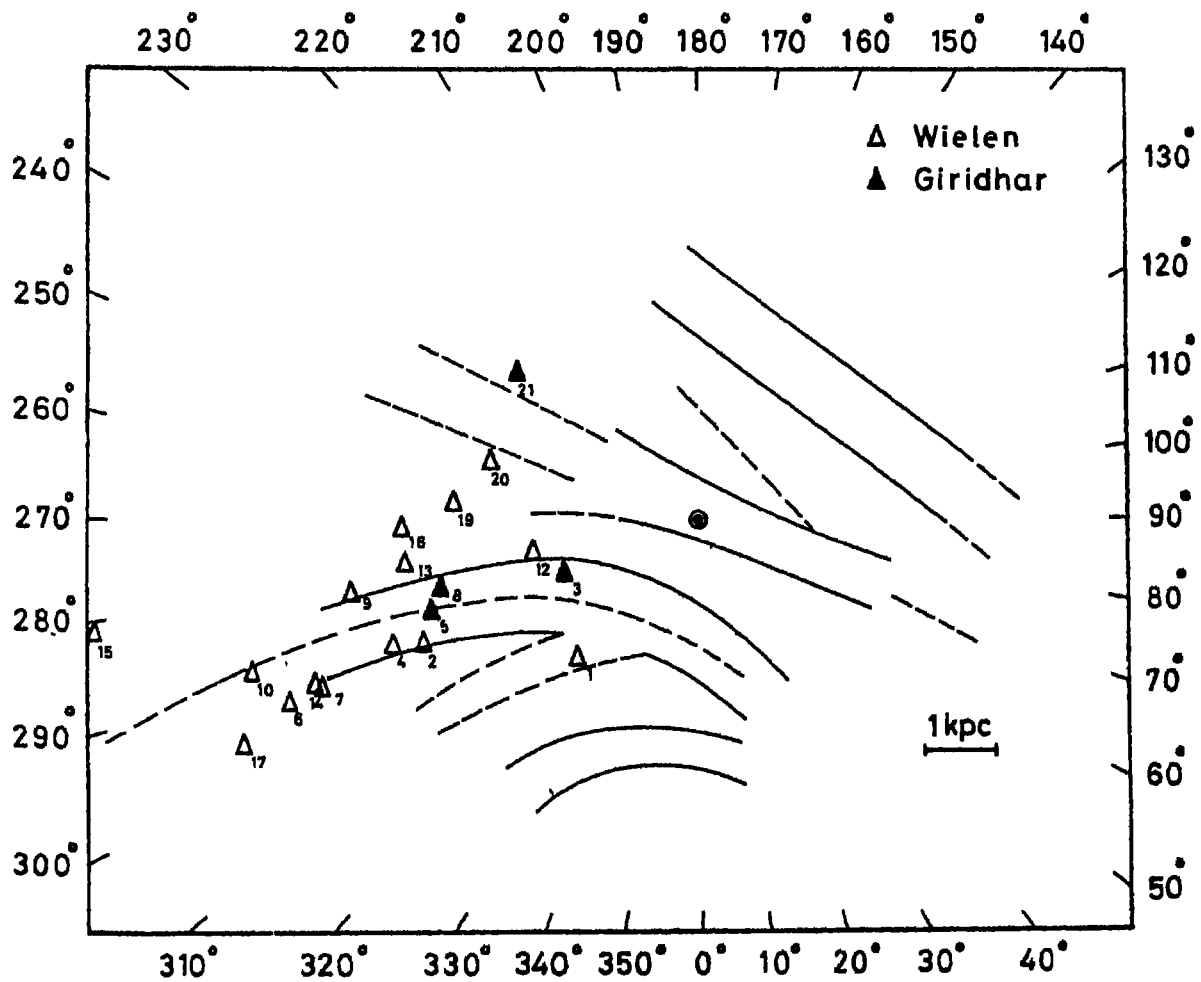


Figure 6.4 Birthsites of Cepheids with respect to the spiral arms sketched by Humphreys (1978). The numbers identify the stars through Table 6.4.

It is clear from Table 6.4 and Figure (6.4) that an overwhelming majority of stars that form at the inner edge of the spiral arms have normal abundances for their galactocentric position. The overabundance of η Sgr and ζ Gem is most probably due to their position at the outer edge of the spiral arm. These stars may have been born after the massive stars formed at the inner edge had exploded as supernovae in the vicinity of their birthsites. The lower-than-expected abundances of Γ Vul and κ Aur are puzzling. If confirmed, they may indicate the presence of local inhomogeneities that are not mixed away even over a few galactic rotations.

6.4 Variation of $[s/Fe]$ across the disc

Iron-peak nuclei are formed by explosive nucleosynthesis within supernovae whereas s-process elements are formed by slow neutron capture by heavy elements in the interiors of red giants. These two processes operate in stars of different mass range ($2-4 M_{\odot}$ for red giants and $8-15 M_{\odot}$ for supernovae with the present uncertainty about $4-8 M_{\odot}$ stars ending as planetary nebulae or supernovae). Thus, the abundance ratio $[s/Fe]$ at different times in the galactic history and the variation of $[s/Fe]$ across the galactic disc may provide important constraints on the theories of galactic evolution.

For metal-deficient stars of halo population, Spite and Spite (1978) found the s-process element barium and to

certain extent - yttrium to be overdeficient. This overdeficiency decreases when $\left[\frac{\text{Fe}}{\text{H}}\right]$ increases and becomes negligible for $\left[\frac{\text{Fe}}{\text{H}}\right] > -1.5$. From an analysis of a homogeneous group of old metal-poor F and G stars in the galactic disk, Huggins and Williams (1974) found a correlation between $\left[\text{s/Fe}\right]$ and $\left[\frac{\text{Fe}}{\text{H}}\right]$. They interpreted this correlation as an evidence that heavier (s-process) metals of the interstellar medium in the disk have increased more rapidly than the overall metal abundance, during the time interval covered by the formation of these stars.

In the present investigation, we have determined the abundance of s-process elements Ba, La, Ce and Sm. These elements present themselves in very few lines in the stellar spectra. This fact increases the uncertainty of the abundance estimates. The use of a composite s-process index S ($S = \frac{1}{N} \sum_i \left[\text{s}_i/\text{Fe}\right]$) has been suggested by Huggins and Williams (1974). These composite indices have the advantage of reduced scatter, though the information about individual elements is lost. In Table 6.5, we give $\left[\frac{\text{Fe}}{\text{H}}\right]$, $\left[\text{Ba/Fe}\right]$, $\left[\text{Ce/Fe}\right]$ and $\left[\text{Sm/Fe}\right]$ for our program stars and the composite indices

$$S_1 = \frac{1}{4} \left\{ \left[\frac{\text{Ba}}{\text{Fe}}\right] + \left[\frac{\text{Ce}}{\text{Fe}}\right] + \left[\frac{\text{La}}{\text{Fe}}\right] + \left[\frac{\text{Sm}}{\text{Fe}}\right] \right\}$$

and

$$S_2 = \frac{1}{3} \left\{ \left[\frac{\text{Ba}}{\text{Fe}}\right] + \left[\frac{\text{Ce}}{\text{Fe}}\right] + \left[\frac{\text{Sm}}{\text{Fe}}\right] \right\}.$$

Table 6.5

Abundances of s-process elements in Cepheids

star	$[\frac{Fe}{H}]$	$[Ba/Fe]$	$[La/Fe]$	$[Ce/Fe]$	$[Sm/Fe]$	s_1	s_2
WZ Sgr	+0.15	0.0	-0.1	-0.2	-0.05	-0.09	-0.08
X Sgr	+0.07	-0.09		-0.27	-0.27		-0.21
ζ Gem	+0.20	-0.25		-0.05	+0.03		-0.09
T Mon	+0.03	+0.07	-0.13	+0.03	-0.12	-0.037	-0.001
SV Mon	-0.10	0.0	+0.03	-0.17	-0.10	-0.06	-0.09

For two of our stars, Ba abundances were not derived so only S_2 could be determined.

We have shown in Figure (6.5) the variation of S_2 with galactocentric distance. It is obvious from the figure that there is no trend in S_2 with galactocentric distance which implies that the rate of enrichment of s-process elements is essentially the same as that of $[\frac{Fe}{H}]$ in the galactic plane. From Figure (6.6) we see that S_2 is not correlated with $[\frac{Fe}{H}]$.

In the simple models of galactic evolution which are based on the assumptions of evolution in isolated well-mixed zones with no initial enrichment, as the system evolves, the abundance of s-process element are predicted to vary as $[\frac{Fe}{H}]^2$. With the inclusion of prompt initial enrichment to account for the observed narrow range of metallicity distribution for G dwarf stars, the abundances of s-process element are no longer expected to vary so fast; but still the predicted abundances variation for s-process elements is faster than that for $[\frac{Fe}{H}]$. In other words, there should be a positive correlation between $[S/Fe]$ and $[\frac{Fe}{H}]$. The correlations obtained by Spite and Spite (1978) and Huggins and Williams (1974) may favour the enrichments predicted by a simple model, but the absence of any significant correlation for young disk stars cannot be explained by a simple model.

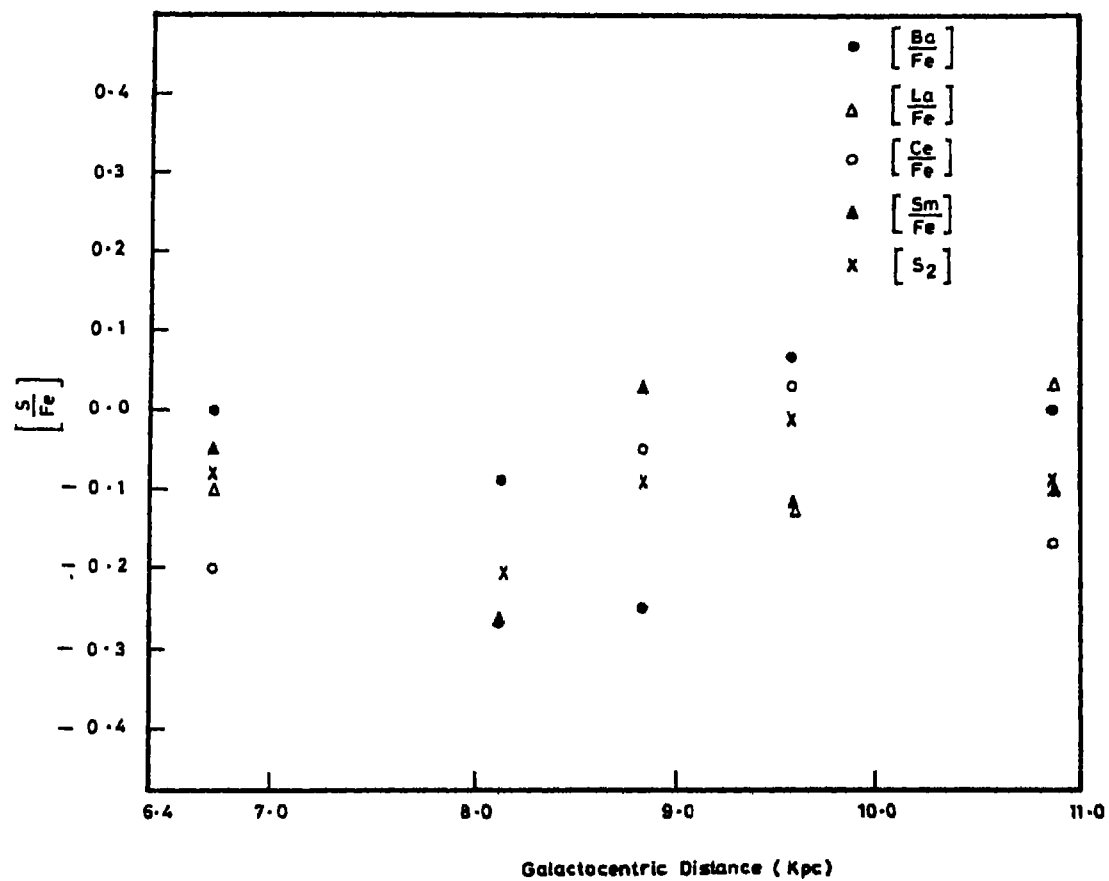


Figure 6.5 A plot of $[s/Fe]$ as a function of galactocentric distance.

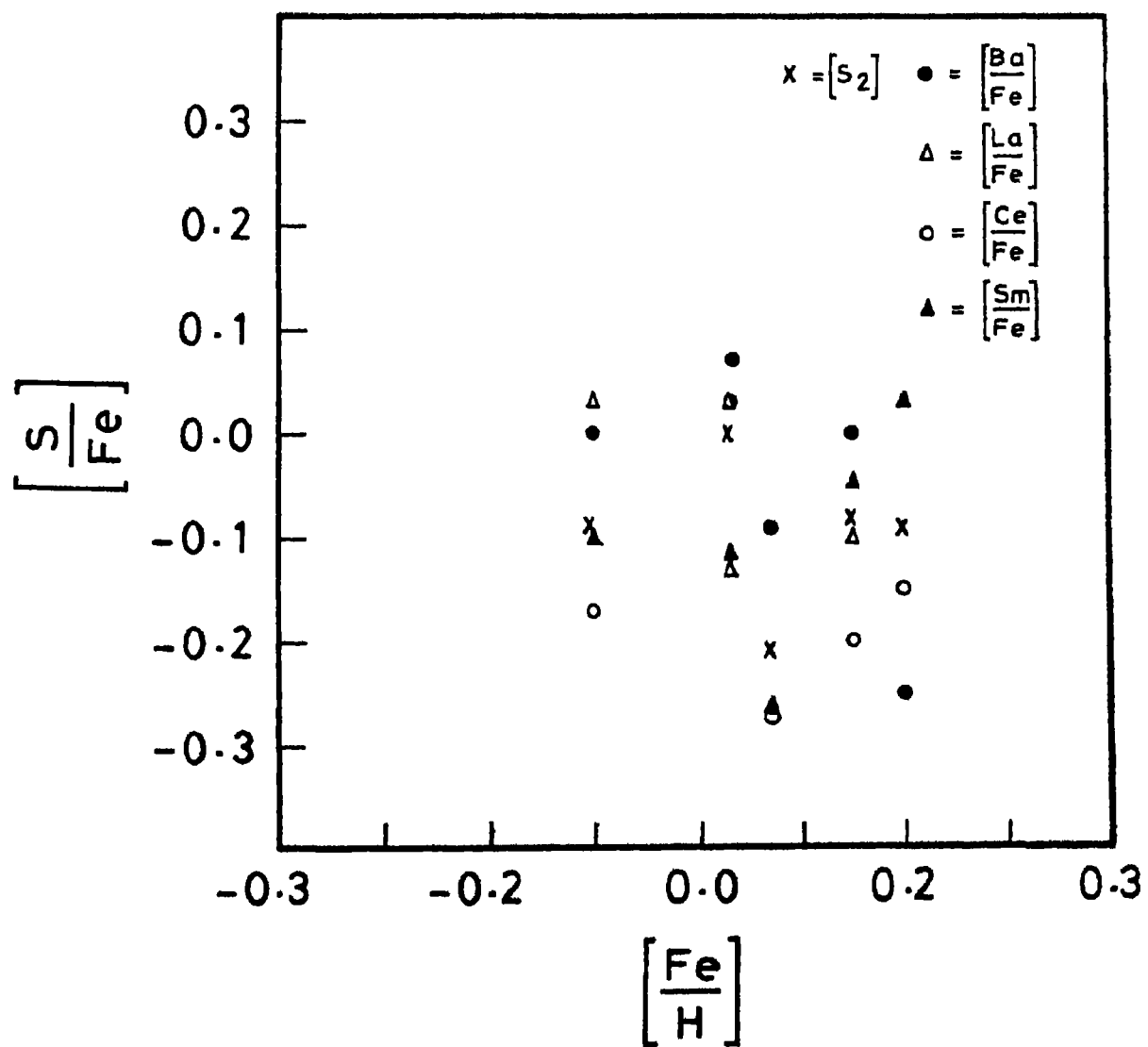


Figure 6.6 A plot of $[s/Fe]$ against $[Fe/H]$.

Instead of a closed system, the models with a steady infall of unprocessed material have been developed by Larson (1974, 1976). In these models, the observed metallicity distributions can be explained without requiring an initial burst of massive stars (Prompt initial enrichment). The infalling metal-poor gas produces a dilution effect which counteracts the enrichment of ISM and hence an asymptotic variation of $\left[\frac{\text{Fe}}{\text{H}}\right]$ and $\left[\frac{\text{s}}{\text{H}}\right]$ are predicted. Thus the ratio $\left[\text{s/Fe}\right]$ does not change after $\left[\frac{\text{s}}{\text{H}}\right]$ and $\left[\frac{\text{Fe}}{\text{H}}\right]$ have reached their asymptotic values. The lack of correlation between $\left[\text{s/Fe}\right]$ and $\left[\text{Fe/H}\right]$ for the young disk stars found in the present investigation favours ^{an} infall model of galactic evolution.

An alternative explanation can be based on the hypothesis of a variable initial mass function. Whereas $\left[\text{Fe}\right]$ is produced in explosive nucleosynthesis in supernova explosions of massive stars, s-process elements are synthesized in the intermediate mass stars. Thus $\left[\text{s/Fe}\right]$ ratio in ISM at a given time is related to the ratio of intermediate to high mass stars. A comparison of $\left[\text{s/Fe}\right]$ in old and young stars may provide useful information on the variations in IMF in the course of galactic evolution. In a simple intuitive way, we can say that the fast enrichment of s-process nuclei in the old halo population stars is due to an increase in the intermediate stars as compared

to the high-mass stars at the time of the formation of the spheroidal population. After the formation of the disk, the number of high mass stars produced might have become larger than the intermediate mass stars. Hence, the abundance of s-process elements for the disk objects does not show the steady enrichment as exhibited by halo stars. It should be borne in mind that the assumption of a constant initial mass function has been made in the models of chemical evolution of galaxies only out of ignorance on star formation processes. The density wave can compress the cold disk gas clouds in the young disk and form massive stars. Such conditions may not exist in the absence of a density wave. Thus the initial mass function at the time of the formation of halo may really have lacked massive stars. Similar effect may have been present in the old disk also. If the old disk could produce massive stars, its chemical evolution may have been diluted by infall.

6.5 Summary of Conclusions

Three major conclusions have been drawn from the present study of the abundances in Cepheid atmospheres:

- 1) There is a gradient in $[Fe/H]$ in the disk between the galactocentric distances 6.74 - 10.87 kpc. The value of the gradient -0.053 ± 0.008 derived by us agrees with the general sample of Cepheids for which spectroscopic abundances

are available, and also with the photometric gradient (-0.07) derived by Harris (1981). The steeper gradient obtained by Luck (1982) is due to a sample limited over a small range of galactocentric distances.

2) There is an indication that a secondary star formation takes place near the outer edge of the spiral pattern, from the interstellar matter locally enriched by supernova explosions.

3) The s-process enrichment of the young galactic disk takes place at the same rate as the Fe enrichment, indicating that the high mass stars are probably formed at a higher rate in the young disk than in the halo, and probably in the old disk too.

CHAPTER 7

DISCUSSION AND FUTURE PROSPECTS

In the present investigation we have demonstrated a successful application of the method of spectrum synthesis in dealing with problems of blending of spectral lines which had so far been a major handicap in the conventional abundance determinations. For the stars with spectral type later than G0, the crowding of lines becomes increasingly severe. This problem cannot be solved by only increasing the dispersion. In a given spectral region, if the frequency of lines is larger than the reciprocal of the line width, all the lines of the regions will be intrinsically blended, and hence increasing the dispersion will not separate these lines. Such a situation is very common in intermediate and late-type stars especially in the blue region of the spectrum which contains a large number of important metallic lines. Further, for the elements like s-process elements which present themselves in very few, and often blended features, the abundance determination at a dispersion of 22.6\AA mm^{-1} employed in the present investigation would have been an impossible task without the spectrum synthesis technique.

Alternately one may advocate the use of red spectral region where the blending of the spectral lines is considerably less. If we abandon blue spectral region in favour of the red one, we would miss important lines of a large number of elements. Thus the method of spectrum synthesis which allows for the effects of blending and hence does not demand a high resolution is an indispensable tool in the study of stellar chemical composition.

Our compilation of the existing spectroscopic abundances for the Cepheids (Section 6.1) shows that spectroscopic abundances are known for only 21 Cepheids. Mostly the Cepheids brighter than visual magnitude 7.0 are spectroscopically studied. The reason for this is obvious. For a given combination of telescope and spectral resolution, there is a limiting brightness fainter than which we cannot observe with a reasonable exposure time. Further, longer exposures should be avoided for the variable stars where the atmospheric parameters change with time. If the fainter Cepheids are to be observed at the same dispersion, one requires telescopes with larger apertures. Using the method of spectrum synthesis, the need of extremely high dispersion is removed. Thus, fainter and hence further Cepheids could be observed spectroscopically with a moderate-size telescope using a slightly lower resolution. With the 102-cm telescope at Kavalur, we have determined spectroscopic abundances of

Cepheids as faint as $m_V = 8.2$. The total number of classical Cepheids with $m_V < 8.5$ is around 90. All these Cepheids can be studied with a 1-m telescope with an observing time of 30-40 nights.

We have used classical Cepheids as probes to study the chemical evolution of our Galaxy. Cepheids as a group have the advantages of high intrinsic luminosity and small age, as also the existence of period-luminosity relation which enables us to determine their distances more accurately. A good coverage of galactocentric distance has enabled us to determine a reliable abundance gradient. Earlier gradient determinations which have covered a large range in galactocentric distances are based on photometric techniques. The accuracy of photometric abundances is much lower than in the case of spectroscopic determinations. The gradient obtained from a smaller sample by Luck (1982) is very steep. This is most likely due to insufficient coverage of galactocentric distances while the abundances of individual stars are quite accurate. This fact emphasizes the need for a good coverage of galactocentric distances.

In order to study the chemical evolution of the halo, metal-deficient high-velocity stars are currently used. An abundance gradient perpendicular to the plane of the Galaxy is discovered by Trefzger (1981). W Virginis stars which belong to halo population also follow their own period-

luminosity relations. One can obtain more accurate distribution of chemical composition perpendicular to the galactic plane by utilizing these stars whose accurate distances can be determined.

The chemical inhomogeneities across the spiral arms (Section 6.3), if confirmed, could provide valuable information on the theories of star formation. According to Lin's density wave theory, compression of gas clouds at the inner edge of the spiral arm due to the propagation of a density wave induces star formation. These newly born stars, due to the difference in angular velocity of the pattern and material angular velocity, drift away from the spiral pattern by a velocity $(\Omega - \Omega_p)$.

The massive stars would explode as supernovae at 0.6 - 1.0 kpc from the spiral arm. It is possible that these supernova explosions may induce further star formation (Sancisi 1974, Knapp and Kerr 1974), or stars may form by some other process from the interstellar matter enriched by this material (Edmunds 1977). These possibilities may be confirmed by studying the abundances in the Cepheid and supergiant atmospheres relative to their birthsites with respect to the spiral pattern. We have shown that the overabundance exhibited by ζ Gem and W Sgr can indeed be explained in this fashion. The sample of stars should be enlarged to study this phenomenon better. In this direction,

the birthsites with respect to the spiral pattern are as important as the abundances themselves. Accurate birthsites can be derived (Wielen 1973) only with a good knowledge of the distances, space velocities and the ages of the stars. The theoretical parameters like the pattern and material velocities, and also the spiral gravitational potential need to be improved. These model parameters are dependent upon the assumed distance to the galactic centre. This distance is generally assumed to be 10 kpc while modern estimates are close to 8.5 kpc. The s-process abundances need to be determined better, using a larger number of lines and extending to a larger sample. The galactic distribution of $[s/Fe]$, especially its dependence on $[Fe/H]$, would provide important constraints on the models of galactic evolution.

Accurate abundance determinations require good models for line-forming regions i.e. model atmospheres. A number of semi-empirical relations based on the limb darkening data have been constructed for the Sun. For other stars, only theoretical models are available. The straightforward way of checking the adequacy of a model atmosphere is by comparing the fluxes predicted by them at different wavelengths with observed fluxes. Detailed comparison for G-K stars shows a good agreement in general, but there is a discrepancy in the ultraviolet region. The fluxes predicted by theoretical models are higher than the observed ones. This difference

becomes larger in red giants. The recent study of Arcturus (Frisk et al 1980) suggests that it is also significant in blue-ultraviolet spectral region. In the case of giants, the discrepancy is proportional to the logarithmic metal abundance. This discrepancy is negligible for population II stars. Most probably, this discrepancy arises due to an unconsidered opacity source which is sensitive to metallicity. A haze of weak spectral lines not included in extensive line list used in the model atmosphere calculation, as suggested by Holweger (1970), could be the source of this extra opacity. The effect on the temperature structures of this extra opacity as estimated by Gustafsson et al (1975) may be $\sim 100\text{K}$. An attempt to study these weak lines in laboratory spectra of iron should be undertaken.

In the spectral line calculations, a correct treatment of line broadening processes is essential. Van der Waals broadening is most dominant for all photospheric lines. ^{In low gravity} For stars like Cepheids natural damping predominates over Van der Waals damping. hydrogen lines, stark broadening is also important. For the calculation of damping half-widths for Van der Waals broadening the formula given by Unsöld (1955) is used in the present investigation. Holweger (1971) suggested a higher value for the interaction constant C_6 . In the determination of solar Na abundances, Holweger found that this larger value eliminated the scatter in the derived abundances for a number of Na I lines for which other atomic parameters were accurately known. We feel that detailed calculations of attraction as well

repulsive interaction potentials between the perturber and lower and upper term of the perturbed element are required to solve the problem.

We have used solar g_f values for the lines used in the present investigation. These values are derived using solar equivalent widths and a good model of solar atmosphere. However, in the list of wavelengths of the lines in the solar spectrum (Moore, Minnaert and Houtgast 1966), some weak lines remain unidentified. In our calculations, we have omitted the spectral regions with such unknown features. Thus we had to leave out some important lines of s-process elements due to the presence of unidentified lines in their close neighbourhood. Detailed laboratory investigations of a number of elements are required for the identification of these lines.

We have indicated a few steps which would lead to the determination of accurate abundances. The importance of accurate abundance estimation need hardly be exaggerated. A radical change in the understanding of nucleosynthesis in stars and of chemical evolution of the Galaxy may appear when more accurate abundance estimates for stars of different age groups are available as a function of their galactocentric position.

APPENDIX

Line Data Used in Synthesizing the Spectrum

We present in the following tables the line data used for synthesizing various spectral regions. The columns of the tables contain the following information:

- 1) WAVELENGTH in \AA units;
- 2) IDENT, identification of the parent atom of the line written in the style of ATLAS i.e., the number earlier to the decimal point is the atomic number of the atom and the digit after the decimal point represents the ionisation state; for example,
Fe I = 26.0, Fe II = 26.1 etc;
- 3) MASS, the atomic mass in amu;
- 4) IP(1), the first ionisation potential of the atom in eV;
- 5) IP(2), the second ionisation potential of the atom in eV;
- 6) EP(1), the excitation potential of the lower state in eV;
- 7) EP(2), the excitation potential of the upper state in eV;
- 8) GF, the statistical weight multiplied by the oscillator strength of the transition.

Table A.1 - Line data : 4329-4335Å

WAVELENGTH	IDENT	MASS	IP(1)	IP(2)	EP(1)	EP(2)	GF
4329.038	62.1	150.400	5.63	11.07	.18	3.03	.01029
4329.537	26.0	55.847	7.87	16.16	2.21	5.06	.00006
4330.024	23.0	50.941	6.74	14.65	.00	2.85	.11445
4330.245	22.1	47.900	6.83	13.85	2.05	4.89	.01069
4330.708	22.1	47.900	6.83	13.85	1.18	4.02	.00832
4330.728	28.0	58.710	7.63	18.17	3.78	6.63	.01622
4330.820	26.0	55.847	7.87	16.16	3.02	5.85	.00047
4330.956	26.0	55.847	7.87	16.16	3.25	6.10	.00769
4331.243	27.0	58.933	7.86	17.06	3.41	6.25	.17386
4331.651	28.0	58.710	7.63	18.17	1.67	4.52	.00912
4332.583	24.0	51.996	6.77	16.50	3.11	5.98	.31940
4332.831	23.0	50.941	6.74	14.65	.02	2.87	.05081
4333.206	40.0	91.220	6.84	13.13	2.40	5.25	.77625
4333.763	57.1	138.906	5.77	11.06	.17	3.05	1.05730
4334.166	62.1	150.400	5.63	11.07	.28	3.12	.00985
4334.246	62.1	150.400	5.63	11.07	.28	3.12	.00985
4334.840	22.0	47.900	6.83	13.85	.81	3.66	.01784

Table A-2 - Line data: 4348-4365Å

WAVELENGTH	IDENT	MASS	IP(1)	IP(2)	EP(1)	EP(2)	GF
4348.947	26.0	55.847	7.87	16.16	2.98	5.82	.01517
4349.799	58.1	140.120	5.47	10.87	.70	3.53	1.32580
4350.840	22.1	47.900	6.83	13.85	2.05	4.89	.04170
4351.056	24.0	51.996	6.76	16.50	.96	3.80	.09120
4351.303	60.1	144.240	5.49	10.72	.18	3.02	.79459
4351.392	26.0	55.847	7.87	16.16	3.40	6.24	.00203
4351.554	26.0	55.847	7.87	16.16	2.98	5.81	.02642
4351.764	26.1	55.847	7.87	16.16	2.69	5.53	.00006
4351.770	24.0	51.996	6.76	16.50	1.03	3.86	.11891
4351.921	12.0	24.305	7.64	15.03	4.33	7.16	.62940
4352.748	26.0	55.847	7.87	16.16	2.21	5.05	.04786
4352.880	23.0	50.941	6.74	14.65	.07	2.92	.12701
4353.948	24.0	51.996	6.76	16.50	3.36	6.20	.35738
4354.067	22.0	47.900	6.83	13.85	2.16	4.99	.13849
4354.266	26.0	55.847	7.87	16.16	3.93	6.73	.01530
4354.436	57.1	138.906	5.77	11.06	.91	3.75	1.19410
4354.514	12.0	24.305	5.49	10.72	4.33	7.16	.26288
4354.615	21.1	44.956	6.54	12.80	.59	3.44	.23990
4354.951	23.0	50.941	6.74	14.65	1.88	4.72	3.19140
4355.093	20.0	40.080	6.11	11.87	2.70	5.53	.03918
4355.902	28.0	58.710	7.63	18.17	3.62	6.45	.05380
4355.943	23.0	50.941	6.74	14.65	.02	2.85	.01549
4356.743	24.0	51.996	6.71	16.50	3.00	5.83	1.30680
4357.514	24.0	51.996	6.76	16.50	3.35	6.19	.43380
4357.530	26.0	55.847	7.87	16.16	3.94	6.77	.00371
4358.170	60.1	144.240	5.49	10.72	.32	3.15	6.20930
4358.512	26.0	55.847	7.87	16.16	2.94	5.77	.06661
4358.718	39.1	88.905	6.38	12.24	.10	2.94	.01155
4358.916	26.0	55.847	7.87	16.16	3.87	6.70	.01023
4359.585	28.0	58.710	7.63	18.17	3.38	6.22	.03381
4359.631	24.0	51.996	6.76	16.50	.98	3.81	.15450
4359.744	40.1	91.220	6.84	13.13	1.23	4.06	.20158
4360.480	22.0	47.900	6.82	13.58	2.17	5.00	.83678
4360.797	26.0	55.847	7.87	16.16	3.63	6.46	.02295
4361.668	58.1	140.120	5.47	10.87	.53	3.36	.18754
4362.038	62.1	140.400	5.63	11.07	.48	3.31	.00764
4362.099	28.1	58.710	7.63	18.17	4.01	6.92	.00752
4362.930	24.1	51.996	6.76	16.50	5.64	8.47	.07500
4362.950	24.0	51.996	6.76	16.50	2.86	5.69	.02032
4363.108	24.0	51.996	6.76	16.50	2.95	5.78	.00525
4363.663	58.1	140.120	5.47	10.87	.65	3.48	.01660
4364.871	24.0	51.996	6.76	16.50	3.09	5.92	.00141

Table A.3 - Line data: 4398-4402Å

WAVELENGTH	IDENT	MASS	IP(1)	IP(2)	EP(1)	EP(2)	GF
4398.020	39.1	88.905	6.38	12.24	.13	2.93	.05623
4398.299	22.1	47.900	6.82	13.58	1.22	4.03	.00108
4398.491	23.1	50.940	6.74	14.65	3.33	6.13	.02238
4398.621	28.0	58.710	7.63	18.17	3.54	6.35	.03501
4399.224	58.1	140.120	5.47	10.87	.33	3.13	.35588
4399.602	28.0	58.710	7.63	18.17	3.85	6.65	.10153
4399.778	22.1	47.900	6.82	12.80	1.24	4.04	.09399
4400.185	28.0	58.710	7.63	18.17	3.63	6.43	.03577
4400.398	21.1	44.956	6.54	12.80	.61	3.41	.37253
4400.580	23.0	50.940	6.74	14.65	.26	3.07	
4400.850	60.1	144.240	5.49	10.72	.05	2.87	
4400.850	28.0	58.710	7.63	18.17	3.65	6.45	
4401.298	26.0	55.847	7.87	16.16	3.60	6.40	
4401.451	26.0	55.847	7.87	16.16	2.83	5.63	
4401.552	28.0	58.710	7.63	18.17	3.19	5.99	

Table A.4 - Line data: 4406-4428Å

WAVELENGTH	IDENT	MASS	IP(1)	IP(2)	FP(1)	FP(2)	GF
4406.153	23.0	50.941	6.74	14.65	1.06	3.12	.63160
4406.652	23.0	50.941	6.74	14.65	.30	3.12	2.16720
4407.272	58.1	140.120	5.74	10.87	.70	3.51	6.28430
4407.652	23.0	50.941	6.74	14.65	.29	3.11	.91200
4407.706	26.0	55.847	7.87	16.16	2.18	5.13	.02746
4407.708	24.0	51.996	6.77	16.50	3.01	5.84	.05302
4408.208	23.0	50.941	6.74	14.65	.28	3.09	3.52000
4408.425	26.0	55.847	7.87	16.16	2.20	5.02	.36630
4408.523	23.0	50.941	6.74	14.65	.26	3.08	.13537
4408.523	23.0	50.941	6.74	14.65	.27	3.09	.20428
4408.798	59.1	140.910	5.42	10.55	.00	2.80	.70318
4408.941	23.1	50.941	6.74	14.65	3.97	6.80	2.36640
4409.128	26.0	55.847	7.87	16.16	3.30	6.13	.01100
4409.248	22.1	47.900	6.83	13.85	1.24	4.06	.00813
4409.526	22.1	47.900	6.83	13.85	1.23	4.05	.00141
4410.306	24.0	51.996	6.77	16.50	3.01	5.81	.04843
4410.525	28.0	58.710	7.63	18.17	3.31	6.13	.07430
4410.953	24.0	51.996	6.77	16.50	2.98	5.78	.00631
4411.083	22.1	47.900	6.83	13.85	3.09	5.92	.59617
4411.092	24.0	51.996	6.77	16.50	3.01	5.84	.10960
4411.884	25.0	54.938	7.43	15.64	4.71	7.50	1.17500
4411.934	22.1	47.900	6.83	13.85	1.22	4.02	.01175
4412.257	24.0	51.996	6.77	16.50	1.03	3.82	.00277
4413.399	26.0	55.847	7.87	16.16	4.07	6.87	.00324
4413.599	26.1	55.847	7.87	16.16	2.68	5.46	.00018
4413.859	24.0	51.996	6.77	16.50	3.55	6.33	.66200
4414.048	26.0	55.847	7.87	16.16	3.60	6.28	.00166
4414.234	26.0	55.847	7.87	16.16	3.07	5.86	.00100
4414.458	26.0	55.847	7.87	16.16	3.37	6.16	.00069
4414.554	40.1	91.220	6.84	13.13	1.24	4.03	.17567
4414.890	25.0	54.938	7.43	15.64	2.88	5.67	1.19230
4415.135	26.0	55.847	7.87	16.16	1.60	4.40	.36937
4415.563	21.1	44.956	6.54	12.80	.59	3.40	.42917
4416.475	23.0	50.940	6.74	14.65	.27	3.06	.24688
4416.828	26.1	55.847	7.87	16.16	2.77	5.56	.00240
4417.287	22.0	47.900	6.82	13.58	1.89	4.68	.75858
4417.389	27.0	58.930	7.86	17.06	3.06	5.85	.17003
4417.723	22.1	47.900	6.82	13.58	1.16	3.95	.06390
4418.342	22.1	47.900	6.82	13.58	1.24	4.02	.01199
4418.430	26.0	55.847	7.87	16.16	2.98	5.77	.00116
4418.574	26.0	55.847	7.87	16.16	3.63	6.41	.00107
4418.785	58.1	140.120	5.47	10.87	.86	3.66	5.10900
4419.104	24.0	51.996	6.76	16.50	3.00	5.78	.06700
4419.273	26.0	55.847	7.87	16.16	3.63	6.41	.00270
4419.778	26.0	55.847	7.87	16.16	3.30	6.09	.00152
4419.942	23.0	50.940	6.74	14.65	.28	3.07	.02344
4420.526	62.1	150.400	5.63	11.07	.33	3.13	.01850
4420.671	21.1	44.956	6.54	12.80	.62	3.41	.00646
4421.125	62.1	150.400	5.63	11.07	.38	3.17	.01348
4421.334	27.0	58.933	7.86	17.06	2.91	5.71	.23070

Table A.4 - continued

WAVLENGTH	IDENT	MASS	IP(1)	IP(2)	EP(1)	EP(2)	GF
4421.573	23.0	50.940	6.74	14.65	.27	3.07	.18380
4421.763	22.0	47.900	6.82	13.58	2.23	5.02	1.20960
4421.944	22.1	47.900	6.82	13.58	2.05	4.84	.01886
4422.505	23.0	50.940	6.74	14.65	1.70	4.50	.88360
4422.572	39.1	88.905	6.38	12.24	.10	2.91	.00011
4422.576	26.0	55.847	7.87	16.16	2.83	5.62	.05373
4422.829	22.0	47.900	6.82	13.58	1.07	3.86	.05880
4422.973	28.0	58.710	7.63	18.68	3.66	6.45	.07454
4423.140	26.0	55.847	7.87	16.16	2.92	5.77	.00606
4423.263	24.0	51.996	6.76	16.50	3.01	5.80	.03236
4423.847	26.0	55.847	7.87	16.16	3.64	6.43	.01827
4424.072	24.0	51.996	6.76	16.50	2.10	4.89	.01958
4424.204	26.0	55.847	7.87	16.16	3.54	6.32	.00229
4424.294	24.0	51.996	6.76	16.50	3.00	5.79	.34530
4425.148	24.0	51.996	6.76	16.50	3.10	5.89	.05000
4425.444	20.0	40.080	6.13	11.87	1.88	4.66	.66069
4425.664	26.0	55.847	7.87	16.16	3.57	6.37	.01341
4425.769	26.0	55.847	7.87	16.16	3.26	6.41	.00085
4425.769	26.0	55.847	7.87	16.16	3.64	6.41	.00129
4425.850	22.0	47.900	6.82	13.58	1.06	3.85	.00650
4426.040	23.0	50.940	6.74	14.65	.29	3.07	.12023
4426.054	22.0	47.900	6.82	13.58	1.88	4.66	.17378
4427.105	22.0	47.900	6.82	13.58	1.50	4.28	1.17240
4427.300	26.0	55.847	7.87	16.16	3.65	6.43	.00077
4427.312	26.0	55.847	7.87	16.16	.05	2.84	.00041

Table A.5 - Line data: 4472-4476Å

WAVELENGTH	IDENT	MASS	IP(1)	IP(2)	EP(1)	EP(2)	GF
4472.704	26.0	55.847	7.87	16.16	3.64	6.39	.00851
4472.723	26.0	55.847	7.87	16.16	3.27	6.02	.00406
4472.802	25.0	55.847	7.43	15.64	2.95	5.74	.28697
4472.930	26.1	55.847	7.87	16.16	2.84	5.59	.00031
4474.049	23.0	50.941	6.74	14.65	1.95	4.71	.62180
4474.755	23.0	50.941	6.74	14.65	1.89	4.65	2.20000
4474.859	22.0	47.900	6.83	13.85	1.44	4.20	.12900
4474.859	22.0	47.900	6.83	13.83	2.10	4.86	.01047
4475.306	24.0	51.996	6.77	16.50	2.89	5.64	.03362
4475.722	39.0	88.904	6.08	12.24	1.40	4.15	.33150
4476.033	26.0	55.847	7.87	16.16	2.84	5.59	.03790
4476.089	26.0	55.847	7.87	16.16	3.69	6.43	.08814

Table A.6 - Line Data: 4483-4489Å

WAVELENGTH	IDENT	MASS	IP(1)	IP(2)	EP(1)	EP(2)	GF
4483.782	26.0	55.847	7.87	16.16	3.64	6.39	.00212
4483.911	27.0	58.933	7.86	17.06	3.13	5.88	.20280
4484.240	26.0	55.847	7.87	16.16	3.60	6.35	.11196
4484.503	27.0	58.933	7.87	17.06	.92	3.68	.00057
4484.659	24.0	51.996	6.76	16.50	3.08	5.84	.00775
4485.422	40.1	91.220	6.84	13.13	1.24	3.97	.02211
4485.683	26.0	55.847	7.87	16.16	3.69	6.43	.08317
4485.976	26.0	55.847	7.87	16.16	3.65	6.40	.00389
4486.914	58.1	140.120	5.47	10.87	.30	3.40	.75070
4487.004	26.0	55.847	7.87	16.16	3.93	6.67	.00159
4487.258	39.0	88.905	6.38	12.24	1.37	4.11	.36727
4487.513	39.0	88.905	6.38	12.24	1.36	4.10	.52480
4487.747	26.0	55.847	7.87	16.16	3.24	5.98	.00121
4488.061	24.0	51.996	6.76	16.50	2.99	5.73	.05223
4488.138	26.0	55.847	7.87	16.16	3.60	6.35	.02500
4488.329	22.1	47.900	6.82	13.58	3.12	5.87	.23990

Table A.7 - Line data: 4506-4518Å

WAVELENGTH	IDENT	MASS	IP(1)	IP(2)	FP(1)	EP(2)	GF
4506.608	20.0	40.080	6.11	11.87	2.52	5.26	.00350
4506.747	22.1	47.900	6.83	13.85	1.13	3.86	.00017
4506.842	24.0	51.996	6.77	16.50	4.18	6.91	.63640
4507.100	40.0	91.220	6.84	13.13	.54	3.28	.23591
4507.227	26.0	55.847	7.87	16.16	3.11	5.84	.00034
4507.395	20.0	40.080	6.11	11.87	2.52	5.26	.00351
4507.858	20.0	40.080	6.11	11.87	2.52	5.26	.00171
4508.011	22.0	47.900	6.83	13.82	2.78	5.51	.44092
4508.289	26.1	55.847	7.87	16.16	2.84	5.59	.00277
4509.128	26.0	55.847	7.87	16.16	2.61	5.78	.00003
4509.270	26.0	55.847	7.87	16.16	3.05	5.78	.00024
4509.298	26.0	55.847	7.87	16.16	3.69	6.42	.00147
4509.449	20.0	40.080	6.11	11.87	2.52	5.26	.00610
4509.995	24.0	51.996	6.76	16.50	4.53	7.26	.39857
4509.995	24.0	51.996	6.76	16.50	4.53	7.26	.02049
4510.160	59.1	140.908	5.42	10.55	.42	3.16	.02049
4510.830	26.0	55.847	7.87	16.16	3.60	6.42	.00133
4511.072	26.0	55.847	7.87	16.16	3.60	6.42	.00166
4511.900	24.0	51.996	6.76	16.50	3.07	5.81	.26190
4512.273	20.0	40.080	6.11	11.87	2.51	5.25	.00855
4512.741	22.0	47.900	6.83	13.85	.83	3.57	.17249
4512.997	28.0	58.710	7.63	18.17	3.69	6.42	.02651
4513.582	39.0	88.905	6.38	12.24	1.90	4.62	.47860
4513.720	22.0	47.900	6.83	13.85	1.43	4.16	.03332
4513.872	28.0	58.710	7.63	18.17	3.54	6.27	.00364
4514.189	26.0	55.847	7.63	16.16	3.03	5.77	.00530
4514.193	23.0	50.941	6.74	14.65	1.94	4.67	1.10770
4514.432	24.0	51.996	6.76	16.50	2.91	5.82	.39899
4514.496	24.0	51.996	6.76	16.50	4.17	6.90	2.19880
4515.178	26.0	55.847	7.87	16.16	2.87	5.61	.00014
4515.337	26.1	55.847	7.87	16.16	2.82	5.52	.00219
4515.440	24.0	51.996	6.76	16.50	3.01	5.74	.05754
4515.597	23.0	50.941	6.74	14.65	1.89	4.63	.85300
4516.272	26.0	55.847	7.87	16.16	3.60	6.38	.01349
4517.089	27.0	58.933	7.86	17.07	3.13	5.85	.15304
4517.154	26.0	55.847	7.87	16.16	3.32	6.06	.00083
4517.530	26.0	55.847	7.87	16.16	3.06	5.79	.01084

Table A.8 - Line data: 4551-4573Å

WAVELENGTH	IDENT	MASS	IP(1)	IP(2)	EP(1)	EP(2)	GF
4551.228	28.0	58.710	7.63	18.17	4.17	6.87	.11220
4551.654	26.0	55.847	7.87	16.16	3.94	6.65	.00876
4552.293	22.1	47.900	6.82	13.58	1.12	3.83	.00085
4552.463	22.0	47.900	6.82	13.58	.84	3.55	.57514
4553.010	40.0	91.220	6.84	13.13	.52	3.23	.06026
4553.056	23.0	50.941	6.74	14.65	2.36	5.06	.00437
4553.174	28.0	58.710	7.63	18.17	3.66	6.35	.01746
4554.036	56.1	137.340	5.21	10.00	.00	2.71	1.47941
4554.460	26.0	55.847	7.87	16.16	2.86	5.56	.00172
4554.536	44.0	101.070	7.37	16.76	.81	3.52	1.41000
4554.834	24.0	51.996	6.77	16.50	3.10	5.81	.04700
4554.992	24.1	51.996	6.77	16.50	4.05	6.76	.03400
4555.069	22.0	47.900	6.82	13.58	2.40	5.11	.79433
4555.090	24.0	51.996	6.77	16.50	3.10	5.80	.12303
4555.295	24.0	51.996	6.77	16.50	3.42	6.13	.03090
4555.492	22.0	47.900	6.82	13.58	.84	3.55	.12426
4555.750	26.0	55.847	7.87	16.16	3.27	5.96	.00018
4555.892	26.1	55.847	7.87	16.16	2.82	5.52	.00074
4556.129	26.0	55.847	7.87	16.16	2.94	5.64	.00260
4556.129	26.0	55.847	7.87	16.16	3.93	6.64	.00010
4556.129	26.0	55.847	7.87	16.16	3.59	6.30	.00257
4556.169	24.0	51.996	6.77	16.50	3.10	5.81	.18197
4556.939	26.0	55.847	7.87	16.16	3.24	5.95	.00179
4557.284	26.0	55.847	7.87	16.16	4.06	6.67	.01359
4557.857	22.0	47.900	6.82	13.58	2.46	5.17	.03890
4558.092	22.0	47.900	6.82	13.58	2.33	5.04	1.22070
4558.092	22.0	47.900	6.82	13.58	2.33	5.04	.00871
4558.103	26.0	55.847	7.87	16.16	3.64	6.33	.00158
4558.103	26.0	55.847	7.87	16.16	3.97	6.67	.00004
4558.460	23.1	50.941	6.74	14.65	3.79	6.49	.00002
4558.460	57.1	138.906	5.58	11.06	.32	3.03	.02455
4558.650	24.1	51.996	6.77	16.50	4.06	6.76	.06606
4559.930	22.0	47.900	6.82	13.58	1.45	4.16	.03845
4559.945	28.0	58.100	7.63	18.17	3.52	6.23	.00402
4560.097	26.0	55.847	7.87	16.16	3.59	6.29	.01510
4560.280	58.1	140.120	5.47	10.87	.43	3.14	1.10800
4560.720	23.0	50.941	6.74	14.65	1.94	4.65	1.13770
4560.966	58.1	140.120	5.47	10.87	.20	2.91	.58288
4561.417	26.0	55.847	7.87	16.16	2.76	5.53	.00099
4562.367	58.1	140.120	5.47	10.87	.00	2.71	.60950
4562.637	22.0	47.900	6.82	13.85	.02	2.73	.00130
4563.237	24.0	51.996	6.77	16.50	3.85	6.54	.16481
4563.438	22.0	47.900	6.82	13.58	2.43	5.12	.37756
4563.766	22.1	47.900	6.82	13.85	1.22	3.92	.13804
4564.173	24.0	51.996	6.77	16.50	4.78	7.46	.25142
4564.578	23.1	50.941	6.74	14.65	2.27	4.96	.04351
4564.702	26.0	55.847	7.87	16.16	3.65	6.11	.00702
4564.828	26.0	55.847	7.87	16.16	3.07	5.76	.00135

Table A.8 - continued

WAVLENGTH	IDENT	MASS	IP(1)	IP(2)	EP(1)	EP(2)	GF
4565.173	24.0	51.996	6.77	16.50	4.78	7.46	1.25900
4565.316	26.0	55.847	7.87	16.16	3.27	5.96	.00268
4565.430	40.1	91.220	6.84	13.13	1.77	4.47	.66992
4565.512	24.0	51.996	6.77	16.50	.98	3.68	.01096
4565.578	27.0	58.933	7.86	17.06	3.00	5.71	.10356
4565.668	26.0	55.847	7.87	16.16	2.55	5.25	.00404
4565.729	24.1	51.996	6.77	16.50	4.02	6.73	.00399
4565.856	58.1	140.120	5.47	10.87	.61	3.52	.60580
4566.233	62.1	150.400	5.63	11.07	.33	3.03	.00842
4566.524	26.0	58.847	7.63	16.16	3.33	5.99	.00615
4566.678	26.0	55.847	7.87	16.16	2.55	5.26	.00007
4566.993	26.0	55.847	7.87	16.16	3.40	6.11	.00196
4568.328	22.1	47.900	6.83	13.85	1.22	3.92	.00095
4568.771	26.0	55.847	7.87	16.16	3.26	5.96	.00345
4568.855	26.0	55.847	7.87	16.16	3.63	6.33	.00704
4569.250	27.1	58.933	7.86	17.06	3.40	6.10	.00323
4569.525	24.0	51.996	6.77	16.50	3.12	7.29	.06383
4569.618	24.0	51.996	6.77	16.50	3.12	5.82	.16696
4570.025	27.0	58.933	7.86	17.06	3.63	6.32	.19638
4570.918	22.0	47.900	6.82	13.85	2.40	5.09	.19383
4571.102	12.0	24.305	7.65	15.03	.00	2.70	.00001
4571.444	26.0	55.847	7.87	16.16	2.87	5.56	.00580
4571.675	24.0	51.996	6.77	16.50	2.54	5.23	.11123
4571.783	23.0	50.941	6.74	14.65	1.94	4.64	1.31825
4571.830	24.0	51.996	6.77	16.50	3.83	6.53	.13804
4571.982	22.1	47.900	6.82	13.85	1.57	4.27	.28284
4572.160	24.0	51.996	6.77	16.50	3.31	6.01	.04600
4572.284	58.1	140.120	5.47	10.87	.28	2.90	2.83480

Table A.9 - Line data: 4574-4584Å

WAVELENGTH	IDENT	MASS	IP(1)	IP(2)	EP(1)	EP(2)	GF
4574.245	26.0	55.847	7.87	16.16	3.20	5.90	.00366
4574.450	24.0	51.996	6.77	16.50	3.07	5.76	.00277
4574.490	40.1	91.220	6.84	13.13	2.42	5.12	.10465
4574.728	26.0	55.847	7.87	16.16	2.27	4.97	.00114
4574.902	57.1	138.906	5.47	10.87	.17	2.87	.01025
4575.121	24.0	51.996	6.77	16.50	3.35	6.05	.08912
4575.800	26.0	55.847	7.87	16.16	3.29	5.98	.00139
4575.800	26.0	55.847	7.87	16.16	3.86	6.56	.00030
4576.339	26.1	55.847	7.87	16.16	2.83	5.56	.00060
4576.551	22.0	47.900	6.83	13.85	2.32	5.02	.03005
4576.785	24.0	51.996	6.77	16.50	3.08	5.76	.02571
4577.184	23.0	50.941	6.74	14.65	.00	2.70	.06452
4577.694	62.1	150.400	5.63	11.07	.25	2.94	.00333
4578.326	24.0	51.996	6.77	16.50	3.83	6.53	.10965
4578.559	20.0	40.080	6.11	11.87	2.51	5.21	.13851
4578.730	23.0	50.941	6.74	14.65	1.93	4.63	.52230
4579.054	26.0	55.847	7.87	16.16	3.87	6.56	.00005
4579.070	26.0	55.847	7.87	16.16	3.26	5.97	.00333
4579.187	23.0	50.941	6.74	14.65	1.94	4.64	.26915
4579.344	26.0	55.847	7.87	16.16	3.68	6.37	.00237
4579.344	26.0	55.847	7.87	16.16	2.82	5.52	.00030
4579.688	26.0	55.847	7.87	16.16	3.63	6.32	.00058
4579.825	26.0	55.847	7.87	16.16	3.06	5.75	.00109
4580.056	24.0	51.996	6.77	16.50	.94	3.63	.03341
4580.139	27.0	58.933	7.86	17.06	.92	3.61	.00069
4580.394	23.0	50.941	6.74	14.65	.02	2.71	.15803
4580.600	26.0	55.847	7.87	16.16	3.64	6.33	.00661
4580.619	28.0	58.710	7.63	18.17	3.64	6.33	.15850
4581.063	24.0	51.996	6.77	16.50	3.07	5.77	.00095
4581.320	39.0	88.905	6.38	12.24	1.90	4.59	.19953
4581.406	20.0	40.080	6.11	11.87	2.52	5.21	.17727
4581.519	26.0	55.847	7.87	16.16	3.24	5.92	.03925
4581.630	27.0	58.933	7.86	17.06	2.94	5.64	.22555
4582.833	26.1	55.847	7.87	16.16	2.84	5.52	.00053
4582.952	26.0	55.847	7.87	16.16	2.84	5.53	.00018
4583.415	22.1	47.900	6.82	13.58	1.16	3.85	.00080
4583.724	26.0	55.847	7.87	16.16	3.10	5.79	.00076
4583.839	26.1	55.847	7.87	16.16	2.80	5.49	.01202
4583.992	26.1	55.847	7.87	16.16	2.70	5.39	.00004

Table A.10 - Line data: 4584-4632Å

WAVELENGTH	IDENT	MASS	IP(1)	IP(2)	FP(1)	FP(2)	GF
4584.706	26.0	55.847	7.87	16.16	3.60	6.28	.00437
4584.752	24.0	51.996	6.77	16.50	3.00	5.70	.00376
4584.824	26.0	55.847	7.87	16.16	3.60	6.28	.01901
4585.874	20.0	40.080	6.11	11.87	2.52	5.21	.65163
4585.923	20.0	40.080	6.11	11.87	2.52	5.21	.01166
4585.973	23.0	50.941	6.74	14.65	1.35	4.05	.44337
4586.144	24.0	51.996	6.77	16.50	3.11	5.79	.07841
4586.378	23.0	50.941	6.74	14.65	.04	2.73	.13804
4587.134	26.0	55.847	7.87	16.16	3.57	6.25	.01197
4587.723	26.0	55.847	7.87	16.16	3.98	6.66	.00554
4588.204	24.1	51.996	6.77	16.50	4.05	6.74	.13182
4589.953	22.1	47.900	6.82	13.58	1.24	3.92	.01905
4591.400	24.0	51.996	6.77	16.50	.96	3.65	.01185
4592.057	24.1	51.996	6.77	16.50	4.04	6.74	.03911
4592.531	28.0	58.710	7.63	18.16	3.54	6.23	.43247
4592.659	26.0	55.847	7.87	16.16	1.55	4.24	.00458
4593.530	26.0	55.847	7.87	16.16	3.94	6.62	.00938
4593.832	24.0	51.996	6.77	16.50	3.32	6.00	.00891
4593.935	58.1	140.120	5.47	10.87	.69	3.37	1.80400
4594.126	23.0	50.940	6.74	14.65	.07	2.76	.18621
4594.639	27.0	58.933	7.86	17.06	3.63	6.31	.39051
4594.894	28.0	58.100	7.63	18.17	3.39	6.08	.02025
4595.216	26.0	55.847	7.87	16.16	3.63	6.31	.00161
4595.365	26.0	55.847	7.87	16.16	3.29	5.97	.02215
4595.593	24.0	51.996	6.77	16.50	4.18	6.86	1.23026
4595.690	26.1	55.847	7.87	16.16	2.86	5.53	.00003
4596.069	26.0	55.847	7.87	16.16	3.62	6.27	.05669
4596.392	26.0	55.847	7.87	16.16	3.65	6.11	.00702
4596.905	27.0	58.933	7.86	17.06	3.63	6.31	.61019
4598.125	26.0	55.847	7.87	16.16	3.27	5.95	.05604
4598.364	26.0	55.847	7.87	16.16	3.94	6.62	.00550
4600.107	24.0	51.996	6.76	16.50	2.53	5.22	.05927
4600.190	23.1	50.941	6.74	14.65	2.26	4.94	.03467
4600.364	28.0	58.710	7.63	18.17	3.58	6.26	.16326

Table A.10 - continued

WAVELENGTH	IDENT	MASS	IP(1)	IP(2)	FP(1)	EP(2)	GF
4600.757	24.0	51.996	6.77	16.50	1.00	3.68	.06607
4600.938	26.0	55.847	7.87	16.16	3.24	5.93	.00252
4601.025	24.0	51.996	6.77	16.50	2.54	5.22	.68994
4601.380	26.1	55.847	7.87	16.16	2.88	5.57	.00002
4602.008	26.0	55.847	7.87	16.16	1.61	4.28	.00040
4602.949	26.0	55.847	7.87	16.16	1.48	4.16	.00255
4603.953	26.0	55.847	7.87	16.16	2.99	5.66	.00069
4604.560	24.0	51.996	6.76	16.50	3.37	5.99	.57770
4604.852	26.0	55.847	7.87	16.16	3.63	6.31	.00152
4604.996	28.0	58.710	7.63	18.17	3.48	6.15	.20280
4605.104	26.0	55.847	7.87	16.16	2.86	5.53	.00025
4605.357	25.0	54.938	7.43	15.64	4.72	7.33	4.67740
4606.226	28.0	58.710	7.63	16.17	3.60	6.26	.10320
4606.396	24.0	51.996	6.76	16.50	4.45	7.13	.93940
4607.087	26.0	55.847	7.87	16.16	3.41	6.08	.00032
4607.338	38.0	87.620	5.70	11.03	.00	2.68	.59290
4607.654	26.0	55.847	7.87	16.16	3.25	5.93	.02089
4607.654	26.0	55.847	7.87	16.16	3.97	6.65	.00115
4609.266	22.1	47.900	6.82	13.85	1.18	3.86	.00029
4609.912	28.0	58.710	7.63	18.17	4.09	6.77	.08251
4611.070	26.0	55.847	7.87	16.16	3.30	5.96	.00250
4611.194	26.0	55.847	7.87	16.16	2.85	5.52	.00132
4611.285	26.0	55.847	7.87	16.16	3.65	6.31	.06853
4613.213	26.0	55.847	7.87	16.16	3.29	5.95	.02377
4613.367	24.0	51.997	6.77	16.50	.96	3.63	.02691
4613.921	40.1	91.220	6.84	13.13	.97	3.64	.14030
4614.150	24.0	51.996	6.77	16.50	3.09	5.77	.03037
4614.216	26.0	55.847	7.87	16.16	3.29	5.96	.00186
4614.534	24.0	51.996	6.77	16.50	3.85	6.51	.10101
4614.583	28.0	58.710	7.63	18.17	3.60	6.24	.00476
4614.726	24.0	51.996	6.76	16.50	3.37	6.04	.04983
4615.456	62.1	150.400	5.63	11.07	.54	3.21	.00379
4615.720	62.1	150.400	5.63	11.07	.18	2.85	.00646
4616.132	24.0	51.996	6.76	16.50	.98	3.66	.01710
4616.628	24.1	51.996	6.76	16.50	4.06	6.74	.02580

Table A.10 - continued

WAVELENGTH	IDENT	MASS	IP(1)	IP(2)	EP(1)	FP(2)	GF
4617.276	22.0	47.900	6.82	13.58	1.75	4.42	.67680
4617.968	28.0	58.710	7.63	18.17	3.77	6.43	.01259
4618.792	26.0	55.847	7.87	16.16	2.94	5.61	.00631
4618.794	24.1	51.996	6.77	16.50	4.07	6.73	.01525
4619.297	26.0	55.847	7.87	16.16	3.60	6.26	.05417
4619.525	22.0	47.900	6.82	13.85	2.33	5.01	.15850
4619.551	24.0	51.996	6.77	16.50	2.99	5.67	.27040
4619.780	23.0	50.941	6.74	14.65	.04	2.71	.01259
4620.132	26.0	55.847	7.87	16.16	3.07	5.73	.00023
4620.347	28.0	58.710	7.63	18.17	3.68	6.34	.00637
4620.513	26.1	55.847	7.87	16.16	2.83	5.50	.00036
4620.811	27.0	58.933	7.86	17.06	2.72	5.38	.00813
4621.033	24.0	51.996	6.77	16.50	2.54	5.21	.00345
4621.618	26.0	55.847	7.87	16.16	3.96	6.62	.00083
4621.888	24.0	51.996	6.77	16.50	2.54	5.20	.04244
4621.963	24.0	51.996	6.77	16.50	2.54	5.20	.04203
4621.963	24.0	51.996	6.77	16.50	3.83	6.50	.29830
4622.491	24.0	51.996	6.77	16.50	3.55	6.21	.81280
4622.751	24.0	51.996	6.77	16.50	2.99	5.64	.10661
4623.101	22.0	47.900	6.82	13.85	1.74	4.40	.85110
4624.419	23.0	50.941	6.74	14.65	1.05	3.72	.12178
4624.901	58.1	140.120	5.47	10.87	1.11	3.78	.70790
4625.052	26.0	55.847	7.87	16.16	3.23	5.90	.02569
4625.441	26.0	55.847	7.87	16.16	3.98	6.65	.00120
4625.771	27.0	58.933	7.86	17.06	3.71	6.38	.46773
4625.920	24.0	51.996	6.77	16.50	3.85	6.51	.37153
4626.182	24.0	51.996	6.77	16.50	.96	3.63	.03754
4626.538	25.0	54.938	7.43	15.64	4.71	7.37	6.74050
4627.368	14.0	28.086	8.15	16.34	5.08	7.74	.01229
4627.549	26.0	55.847	7.87	16.16	3.30	5.97	.00108
4628.160	58.1	140.120	5.47	10.87	.52	2.71	1.49980
4628.457	24.0	51.996	6.77	16.50	3.14	5.80	.03624
4629.336	22.0	47.900	6.82	13.85	1.73	4.39	.60256
4629.336	26.1	55.847	7.87	16.16	2.81	5.46	.00316
4629.359	27.0	58.933	7.86	17.06	3.05	5.71	.05255
4630.128	26.0	55.847	7.87	16.16	2.28	4.93	.00398
4631.036	26.0	55.847	7.87	16.16	4.10	6.76	.00253
4631.484	26.0	55.847	7.87	16.16	4.55	7.20	.01092

REFERENCES

- Abramowitz, M.,
Stegun, I.A. 1965 Handbook of Mathematical
Functions, N.B.S. Applied
Mathematical Ser., No.55
- Adams, W.S.,
Russell, H.N. 1928 Astrophys. J., 68, 9
- Aller, L.H. 1976 Publ. astr. Soc. Pacific,
88, 574
- Arp, H.C.,
Kraft, R.P. 1961 Astrophys. J., 133, 420
- Auer, L.H.,
Nihalas, D. 1973 Astrophys. J., 184, 151
- Baade, W.,
Swope, H.H. 1965 Astr. J., 70, 212
- Baker, A.E. 1925 Proc. R. Soc. Edinburgh, 45, 116
- Bappu, M.K.V.,
Raghavan, N. 1969 Mon. Not. R. astr. Soc., 142,
295
- Barker, T. 1974 Ph.D Thesis, University of
California, Santa Cruz.
- Bates, D.R. 1951 Mon. Not. R. astr. Soc., 111,
303
- Becker, W.,
Fenkart, K. 1970 in IAU Symp. 38 : The Spiral
Structure of our Galaxy, Eds.
W. Becker and G. Contopoulos,
D. Reidel, Dordrecht, p.205
- Bell, R.A.,
Parsons, S.B. 1972 Astrophys. Lett., 12, 5
- Bell, R.A.,
Rodgers, A.W. 1967 Mon. Not. R. astr. Soc., 135,
121
- Benvenuti, P.,
D'Odorico, S.,
Pembert, M. 1973 Astr. Astrophys., 28, 447

- Berkhuijsen, E.M. 1974 Astr. Astrophys., 35, 429
- Dolton, C.T. 1970 Astrophys. J., 161, 1187
- Hurbidge, E.M.,
Hurbidge, G.R.,
Fowler, W.A.,
Hoyle, F. 1957 Rev. Mod. Phys., 29, 547
- Cameron, A.G.W. 1955 Astrophys. J., 121, 144
- Cameron, A.G.W. 1968 in Origin and Distribution of
Elements, Ed. L.H. Ahrens,
Pergamon Press, New York,
p. 125
- Campbell, W.W. 1901 Astrophys. J. 13, 90
- Canterna, R. 1976 Astr. J., 81, 228
- Carbon, D.,
Gingerich, O.,
Latham, D. 1969 in Low-Luminosity Stars,
Ed. S.S. Kumar, Gordon and
Breach, New York, p. 435
- Cayrel, R.,
Jugaku, J. 1963 Ann. Astrophys., 26, 495
- Chevalier, R.A. 1975 Astrophys. J., 200, 698
- Chevalier, R.A. 1976a Nature, 260, 689
- Chevalier, R.A. 1976b Astrophys. J., 208, 826
- Chevalier, R.A.,
Kirshner, R.P. 1978 Astrophys. J., 219, 931
- Comte, G. 1975 Astr. Astrophys., 39, 197
- Cowley, C.R. 1970 The Theory of Stellar Spectra,
Gordon and Breach, New York
- Dalgarno, A. 1962 Geophys. Corp. of Am., GCA
Tech. Rep., No.62-28-A
- de Jager, C. 1972 Solar Phys., 25, 71
- de Jager, C. 1980 in The Brightest Stars, D. Reidel,
Dordrecht, p. 195

- de Jager, C.,
Neven, L. 1975 *Astrophys. Space Sci.*, 33, 295
- de Vacouleurs, G. 1968 *Appl. Opt.*, 7, 1513
- Dixon, M.E.,
Ford, V.L.,
Robertson, J.W. 1972 *Astrophys. J.*, 174, 17
- D'Odorico, S.,
Peubert, M.,
Sabbadin, F. 1976 *Astr. Astrophys.*, 47, 341
- Drawin, H.W.,
Helenbok, P. 1965 *Data for Plasma in Local
Thermodynamic Equilibrium*,
Gauthier-Villiers, Paris
- Edmonds, F.N.,
Richard, R.,
Servajean, R. 1965 *Ann. Astrophys.*, 28, 534
- Eremov, Yu, N. 1978 *Soviet Astr.*, 22, 161
- Eggen, O.J. 1951 *Astrophys. J.*, 113, 367
- Eggen, O.J. 1969 *Astrophys. J.*, 156, 617
- Eggen, O.J. 1976 *Q.J.R. astr. Soc.*, 17, 472
- Eggen, O.J.,
Lynden-Bell, D.,
Sandage, A.R. 1962 *Astrophys. J.*, 136, 748
- Elmegreen, B.G.,
Lada, C.J. 1977 *Astrophys. J.*, 214, 725
- Evans, N.R. 1976a *Astrophys. J. Suppl. Ser.*,
32, 399
- Evans, N.R. 1976b *Astrophys. J.*, 209, 135
- Evans, T.L. 1968 *Mon. Not. R. astr. Soc.*,
141, 109
- Faber, S.M. 1973 *Astrophys. J.*, 179, 731
- Faber, S.M. 1977 *in the Evolution of the Galaxies
and Stellar Populations*, Eds.
B.M. Tinsley and R.M. Larson,
Yale University Observatory

- Fernie, J.D. 1968 *Astrophys. J.*, 151, 197
- Fernie, J.D. 1970 *Astrophys. J.*, 161, 674
- Frisk, U.,
Bell, R.A.,
Gustafsson, B.,
Nordh, L.,
Olofsson, G. 1980 Preprint
- Gascoigne, S.C.B. 1969 *Mon. Not. R. astr. Soc.*,
146, 7
- Gingerich, O. 1964 in Proc. First Harvard-
Smithsonian Conf. on Stellar
Atmospheres, Smithsonian
Astrophys. Obs. Spec. Rep.
No.167, p.17
- Gingerich, O. (Ed.) 1969 *Theory and Observation of*
Normal Stellar Atmospheres,
MIT Press, Cambridge
- Gingerich, O.,
Noyes, R.W.,
Kalkofen, W.,
Cuny, Y. , 1971 *Solar Phys.*, 18, 347
- Goldberg, L.,
Pierce, A.K. 1948 Office of Naval Research
Project M720-5, Contract Mb-232,
Tech. Rept. No.1, Engineering
research centre, University of
Michigan, Ann Arbor, Michigan
- Goldberg, L.,
Pierce, A.K. 1959 *Encyclopedia of Physics*,
Springer-Verlag, Berlin, 52, 59
- Gray, D.F. 1967 *Astrophys. J.* 149, 317
- Gray, D.F. 1976 *The Observation and Analysis of*
Stellar Photospheres, John Wiley
and Sons, New York
- Grenon, M. 1972 in IAU Col.17: *L'age des etoiles*,
Eds. G. Cayrel de Strobel and
A.M. Delplace, Meudon Observa-
tory, Paris, Chapter 55.
- Gull, S.F. 1974 *Mon. Not. R. astr. Soc.*, 171,
263

- Gustafsson, B.,
Bell, R.A.,
Eriksson, K.,
Nordlund, A. 1975 Astr. Astrophys., 42, 407
- Hansen, L.,
Kjaergaard, P. 1971 Astr. Astrophys., 15, 123
- Harris, D.L. 1953 Astrophys. J., 118, 346
- Harris, H.C. 1981 Astrophys. J., 86, 707
- Harris, H.C.,
Canterna, R. 1979 Astrophys. J., 84, 1750
- Hawley, S.A. 1977 Bull. am. astr. Soc., 9, 374
- Hawley, S.A. 1978 Astrophys. J., 224, 417
- Herbst, W.,
Assouba, G.E. 1977 Astrophys. J., 217, 473
- Herbst, W.,
Assouba, G.E. 1978 in Proto-stars and Planets,
Ed. T. Gehrels, The University
of Arizona Press, Tucson,
p. 368
- Hofmeister, E. 1967 Z. Astrophys., 65, 164
- Hollars, D.R.,
Reitsema, H.J. 1974 Publ. astr. Soc. Pacific, 86,
330
- Holweger, H. 1970 Astr. Astrophys., 4, 11
- Holweger, H. 1971 Astr. Astrophys. 12, 310
- Holweger, H.,
Muller, E.A. 1974 Solar Phys., 39, 19
- Huggins, P.J.,
Williams, P.M. 1974 Mon. Not. R. astr. Soc.,
169, 1p.
- Humphreys, R.M. 1978 in IAU Symp. 84: The large-
Scale Characteristics of the
Galaxy, Ed. W.B. Burton,
D. Reidel, Dordrecht, p. 93
- Iben, I. Jr. 1967 A Rev. Astr. Astrophys., 5, 571
- Jacobson, T.S. 1926 Lick Obs. Bull., 12, 138

- James, K.A. 1977 in IAU Col.45: Chemical and Dynamical Evolution of our Galaxy, Eds. E. Basinska-Grzesik and M. Mayor, Geneva Observatory, p.173
- James, K.A. 1979 *Astrophys. J. Suppl. Ser.*, 39, 135
- James, K.A.,
McClure, R.D. 1972 in IAU Coll. 17: L'age des etoiles, Eds. G. Cayrel de Strobel and A.M. Delplace, Meudon Observatory, Paris, Chapter 28.
- John, T.L. 1968 *Mon. Not. R. astr. Soc.*, 138, 137
- Joy, A.A. 1937 *Astrophys. J.*, 86, 363
- Keller, C.F.,
Mutschlecner, J.P. 1970 *Astrophys. J.*, 161, 217
- Kinman, T.D. 1959 *Mon. Not. R. astr. Soc.*, 119, 538
- Kippenhahn, R.,
Smith, L. 1969 *Astr. Astrophys.*, 1, 142
- Krapp, G.R.,
Kerr, F.J. 1974 *Astr. Astrophys.*, 33, 463
- Krafft, R.P. 1961 *Astrophys. J.*, 134, 616
- Kraft, R.P. 1967 in IAU Symp. 28: Aerodynamic Phenomena in Stellar Atmospheres, Ed. R.N. Thomas, Academic Press, New York, London, p. 207
- Kukarkin, B.V.,
Kholopov, P.N.,
Litremov, Yu. N.,
Kukarkina, N.,
Kurochkin, N.D.,
Medvedeva, G.I.,
Perova, N.B.,
Pedorovich, V.P.,
Frolov, M.S. 1969 *General Catalogue of Variable Stars*, Astronomical Council of the Academy of Sciences, Moscow

- Kurucz, R.L. 1970 Smithsonian Astrophysical Obs. Spec. Rep. No.319
- Kurucz, R.L. 1975 In Multicolour Photometry and IR Diagram, Eds. A.G. Davis Phillip and D.S. Hayes, Dudley Obs. Rep. No.9, 271
- Kurucz, R.L. 1979 Astrophys. J. Suppl. Ser., 40, 1
- Kurucz, R.L.,
Peytremann, E. 1975 Smithsonian Astrophys. Obs. Spec. Rep., No.362
- Larson, R.B. 1974 Mon. Not. R. astr. Soc., 166, 585
- Larson, R.B. 1976 Mon. Not. R. astr. Soc., 176, 31
- Lin, C.C.,
Yuan, C.,
Shu, F.H. 1969 Astrophys. J., 155, 721
- Lub, J.,
Pel, J.W. 1977 Astr. Astrophys., 54, 137
- Luck, R.E. 1977a Astrophys. J., 212, 743
- Luck, R.E. 1977b Astrophys. J., 218, 752
- Luck, R.E. 1978 Astrophys. J., 219, 148
- Luck, R.E. 1979 Astrophys. J., 232, 797
- Luck, R.E. 1982 Astrophys. J., 256, 177
- Luck, R.E.,
Bond, H.E. 1980 Astrophys. J., 241, 214
- Luck, R.E.,
Lambert, D.L. 1981 Astrophys. J., 245, 1018
- Lynden-Bell, D. 1967 Mon. Not. R. astr. Soc., 136, 101
- Lynden-Bell, D. 1975 Vistas in Astr., 19, 299
- Madore, B.F. 1974 Ph.D Thesis, University of Toronto, Canada

- Mariska, J.T.,
Dosechok, G.A.,
Feldman, U. 1980 *Astrophys. J.* 242, 1083
- Matsushima, S. 1964 in Proc. First Harvard-Smithsonian
Conf. on Stellar Atmospheres,
Smithsonian Astrophys. Obs.
Spec. Rep., No. 167, p. 42
- Mayor, M. 1976 *Astr. Astrophys.*, 48, 301
- Menzel, D.H. 1936 *Astrophys. J.*, 84, 462
- Mezger, P.G.,
Pankonin, V.,
Schmid-Burkg, J.,
Thum, C.,
Wink, J. 1980 *Astr. Astrophys.*, 80, L3
- Minnaert, M.,
Mulders, G.F.W. 1931 *Z. Astrophys.*, 2, 165
- Minnaert, M.,
Mulders, G.F.W.,
Houtgast, J. 1940 *Photometric Atlas of the Solar
Spectrum*, Ed. D. Schrabel,
Amsterdam.
- Minnaert, M.,
Slob, C. 1931 *Proc. K. Acad. Amst.*, 34, 542
- Mitchell, R.,
Iriarte, B.,
Steinmetz, D.,
Johnson, H.L. 1964 *Bol. Obs. Tonantzintla Tacubaya*,
3, 153
- Moore, C.E. 1945 *Contributions from the Princeton
University*, No. 20, 1
- Moore, C.E.,
Minnaert, M.G.J.,
Houtgast, J. 1966 *The Solar Spectrum 2935 Å to
8770 Å*, N.B.S. Monograph 61
- Nikolov, N.C.,
Ivanov, G.R. 1974 *Variable Stars*, 20, 63
- Ögelman, H.H.,
Maran, S.P. 1976 *Astrophys. J.*, 209, 124
- Pagel, B.E.J. 1977 in Proc. Second IAGC Symp. on
Origin and Distribution of the
Elements, UNESCO, Paris, p.79

- Pagel, B.E.J.,
Edmunds, M.G. 1981 A Rev. Astr. Astrophys.,
19, 77
- Panagia, N.,
Tosi, M. 1980 Astr. Astrophys., 81, 375
- Panagia, N.,
Tosi, M. 1981 Astr. Astrophys., 96, 306
- Parsons, S.B. 1969 Astrophys. Suppl. Ser. 18, 127
- Parsons, S.B. 1971 Mon. Not. R. astr. Soc.,
152, 121
- Patterson, R.S.,
Neff, J.S. 1979 Astr. Astrophys. Suppl. Ser.,
41, 215
- Peimbert, M. 1968 Astrophys. J., 154, 33
- Peimbert, M. 1973 Mem. Soc. R. Sci. Liege,
Ser., 6, 5, 307
- Peimbert, M. 1979 in IAU Symp. 84 : The Large
Scale Characteristics of the
Galaxy, Ed. W.B. Burton,
D. Reidel, Dordrecht, p. 79
- Peimbert, M.,
Serrano, A. 1980 Rev. Mex. Astr. Astrofis., 5, 9
- Peimbert, M.,
Torres-Peimbert, S 1976 Astr. J., 203, 581
- Peimbert, M.,
Torres-Peimbert, S 1979 Paper presented at the 17th
General Assembly of IAU,
Montreal
- Peimbert, M.,
Torres-Peimbert, S.,
Kayo, J.F. 1978 Astrophys. J., 220, 516
- Pel, J.W. 1976 Astr. Astrophys. Suppl. Ser.,
24, 413
- Pel, J.W. 1978 Astr. Astrophys. 62, 75
- Rautela, B.S.,
Joshi, S.C. 1976 Astrophys. Space Sci.,
40, 455
- Rodgers, A.W.,
Bell, R.A. 1963 Mon. Not. R. astr. Soc.,
125, 487

- Rodgers, A.W.,
Bell, R.A. 1964a Mon. Not. R. astr. Soc.,
127, 471
- Rodgers, A.W.,
Bell, R.A. 1964b Mon. Not. R. astr. Soc.,
129, 9
- Rodgers, A.W.,
Bell, R.A. 1967 Mon. Not. R. astr. Soc.,
136, 91
- Rodgers, A.W.,
Bell, R.A. 1968 Mon. Not. R. astr. Soc.,
138, 23
- Ross, J.,
Aller, L. 1968 Astrophys. J., 153, 235
- Russell, H.N. 1929 Astrophys. J., 70, 11
- Russell, H.N.,
Adams, W.S.,
Moore, C.E. 1928 Astrophys. J., 68, 1
- Sancisi, R. 1974 in IAU Symp. 60 : Galactic
Radio Astronomy, Eds. F.J. Kerr
and S.C. Simonson, III,
D. Reidel, Dordrecht, p. 115
- Sandage, A.,
Tammann, G.A. 1968 Astrophys. J., 151, 531
- Sandage, A.,
Tammann, G.A. 1969, Astrophys. J., 157, 683
- Sanford, R.F. 1956 Astrophys. J., 123, 201
- Scarfe, C.D. 1976 Astrophys. J., 209, 141
- Schaltenbrand, L.,
Tammann, G.A. 1971 Astr. Astrophys. Suppl. Ser. 4, 265
- Schmidt, E.G. 1971 Astrophys. J., 170, 109
- Schmidt, E.G. 1972a Astrophys. J., 174, 595
- Schmidt, E.G. 1972b Astrophys. J., 174, 605
- Schmidt, E.G.,
Kosendhal, J.D.,
Jewsbury, C.P. 1974 Astrophys. J., 189, 293
- Schmidt, M. 1963 Astrophys. J., 137, 758

- Schwarzschild, M.,
Schwarzschild, B.,
Adams, W.S. 1948 Mon. Not. R. astr. Soc.,
108, 207
- Searle, L. 1971 Astrophys. J., 168, 327
- Shapley, H.,
McKibben, V. 1940 Proc. Natl. Acad. Sci.,
26, 105
- Shields, G.A. 1974 Astrophys. J., 193, 335
- Snedden, C.A. 1974 Ph.D Thesis, The University
of Texas at Austin
- Spite, M.,
Spite, F. 1978 Astr. Astrophys., 67, 23
- Stibbs, D.W.N. 1955 Mon. Not. R. astr. Soc.,
115, 363
- Stille, J.L.,
Callaway, J. 1970 Astrophys. J., 160, 245
- Strömberg, B. 1940 Festschrift für Elis Strömberg,
Munksgaard, Copenhagen
- Suess, H.,
Urey, H.C. 1956 Rev. mod. Phys., 28, 53
- Sweigart, A.V.,
Mengel, J.G. 1979 Astrophys. J., 229, 624
- Talent, D.L.,
Dufour, R.J. 1977 Astrophys. J., 233, 888
- Tammann, G.A. 1970 in IAU Symp. 38 : The Spiral
Structure of our Galaxy, eds.
W. Becker and G. Contopoulos,
D. Reidel, Dordrecht, p.236
- Ten Bruggencate, P.,
Lust-Kulka, R.,
Vogt, H.H. 1953 Nachr. Akad. Wiss. Göttingen,
43
- Torres-Peimbert, S.,
Peimbert, M. 1977 Rev.Mex. Astr. Astrofis., 2, 181
- Trefzger, C.F. 1981 Astr. Astrophys., 95, 184

- Psarevsky, G.S. 1967 Inf. Bull. Var. Stars, No.176
- Psuji, T. 1964 Ann. Tokyo astr. Obs., 2nd Ser., 2, 1
- Ulrich, R.K. 1973 in Explosive Nucleosynthesis, Eds. D.N. Schramm and W.D. Arnett, University Texas Press, Austin, p. 139
- Ulrich, R.K. 1974 Astrophys. J., 192, 507
- Unsöld, A. 1955 Physik der Sternatmosphären, 2 edn, Springer-Verlag, Berlin
- Van den Bergh, B. 1958 Astr. J., 63, 492
- Van den Bergh, B. 1977 in IAU Coll. 37 : Decalages vers Le Rouge et Expansion De L'univers, Eds. C. Balkowski and B.E. Westerlund, Centre National de La Recherche Scientifique, Paris, p. 13
- Van Paradys, J.L. 1971 Astr. Astrophys., 11, 299
- Vardya, M.S. 1982 Astrophys. Space Sci., 84, 155
- Vernazza, J.E.,
Arnett, E.H.,
Loeber, K. 1976 Astrophys. J. Suppl. Ser., 30, 1
- Viswanath, C. 1981 Kodaikanal Obs. Bull. Ser. A, 3, 57
- Voigt, W. 1912 Munch Ber., No.603
- Voigt, H.W. (Ed.) 1965 Landolt-Bornstein Vol. of Astr. and Astrophys., Springer-Verlag, Berlin
- Wallerstein, G. 1972 Publ. astr. Soc. Pacific, 84, 656
- Walraven, J.H.,
Tinbergen, J.,
Walraven, T.H. 1964 Bull. astr. Inst. Netherl., 17, 520
- Wiele, R. 1973 Astr. Astrophys., 25, 285

Williams, J.A.	1966	Astrophys. J., <u>71</u> , 615
Wisniewski, W.Z., Johnson, H.L.	1968	Commu. Lunar Planet. Lab., <u>7</u> , 57
Wrubel, M.H.	1949	Astrophys. J., <u>109</u> , 66
Yuan, C.	1969	Astrophys. J., <u>158</u> , 889